



HAL
open science

Separated representations for th multiscale simulation of the mechanical behavior and damages of composite materials.

Sondes Metoui

► **To cite this version:**

Sondes Metoui. Separated representations for th multiscale simulation of the mechanical behavior and damages of composite materials.. Mechanics of materials [physics.class-ph]. Ecole nationale supérieure d'arts et métiers - ENSAM, 2015. English. NNT : 2015ENAM0049 . tel-01311101

HAL Id: tel-01311101

<https://pastel.hal.science/tel-01311101>

Submitted on 3 May 2016

HAL is a multi-disciplinary open access archive for the deposit and dissemination of scientific research documents, whether they are published or not. The documents may come from teaching and research institutions in France or abroad, or from public or private research centers.

L'archive ouverte pluridisciplinaire **HAL**, est destinée au dépôt et à la diffusion de documents scientifiques de niveau recherche, publiés ou non, émanant des établissements d'enseignement et de recherche français ou étrangers, des laboratoires publics ou privés.

2015-ENAM-0049

École Doctorale n° 432: Science des Métiers de l'ingénieur

Doctorat ParisTech

THÈSE

pour obtenir le grade de docteur délivré par

l'École Nationale Supérieure d'Arts et Métiers

Spécialité "Mécanique-Matériaux"

Présentée et soutenue publiquement par

Sondes METOUI

le 01/12/2015

**Separated representations for the multiscale simulation of the
mechanical behavior and damages of composite materials.**

Directeurs de thèse: **Ivan IORDANOFF & Amine AMMAR**
Co-encadrement de la thèse: **Etienne PRULIÈRE & Frédéric DAU**

Jury

M. Francisco CHINESTA, Professeur, GEM, École Centrale de Nantes
M. Elias CUETO, Professeur, GEMM, Université de Saragosse
M. Laurent GALLIMARD, Professeur, LEME, Université Paris Ouest Nanterre La Défense
M. David RYCKELYNCK, Professeur, Centre des Matériaux, Mines ParisTech
M. Olivier POLIT, Professeur, LEME, Université Paris Ouest Nanterre La Défense
M. Amine AMMAR, Professeur, LAMPA, Arts et Métiers ParisTech
M. Etienne PRULIÈRE, Maître de Conférence, I2M, Arts et Métiers ParisTech
M. Frédéric DAU, Maître de Conférence, I2M, Arts et Métiers ParisTech

Président
Rapporteur
Rapporteur
Examineur
Examineur
Examineur
Examineur
Examineur

T
H
È
S
E

Remerciements

Me voilà arrivée au bout de cette aventure mais déjà une autre se dessine. Le moment est arrivé d'écrire les tous derniers mots de ce manuscrit. Je n'aurais jamais pu réaliser ce travail sans le soutien de plusieurs personnes à qui j'exprime mes sincères remerciements.

Je tiens à exprimer tout d'abord mes remerciements aux membres du jury qui ont accepté d'évaluer mon travail de thèse.

J'adresse un grand merci à Ivan Iordanoff, directeur de cette thèse, pour avoir retenu ma candidature, m'avoir accueillie au sein du laboratoire et qui malgré un emploi du temps très chargé à toujours pris le temps de suivre avec attention le bon déroulement de mon travail.

Je tiens particulièrement à témoigner ma profonde gratitude envers Amine Ammar, co-directeur de cette thèse, pour son suivi et ses conseils avisés lors des étapes cruciales de cette thèse. Les mots me manquent pour dire à quel point le côtoyer fut enrichissant, tant professionnellement que personnellement. De lui, j'ai toujours reçu les encouragements dont le doctorant a tant besoin. Je tiens également à le remercier pour la confiance qu'il n'a cessée de me renouveler. j'ai été extrêmement sensible à ses qualités humaines d'écoute et de compréhension tout au long de cette thèse.

Je ne trouve pas vraiment les mots pour dire à quel point je remercie Etienne Prulière pour son encadrement au quotidien. Ce travail n'aurait pas été ce qu'il est sans lui, sans sa grande expérience scientifique et numérique, ses qualités humaines, le temps qu'il m'a consacré et encore tellement d'autres choses... J'ai apprécié nos discussions parfois divergentes mais toujours constructives. Je le remercie pour son suivi régulier, ses encouragements et pour la grande liberté qu'il m'a laissée. Son soutien m'a été précieux et m'a rassuré lors de l'épuisante dernière ligne droite (manuscrit et soutenance). Nous avons formé une très bonne équipe qui va beaucoup me manquer.

Je remercie aussi chaleureusement Frédéric Dau, encadrant de ce travail, pour ses interventions extrêmement bénéfiques. Je le remercie pour ses conseils et sa bonne humeur.

J'en profite également pour remercier mes différents collègues et surtout ami(e)s thésard(e)s. Pour ne pas en oublier, je ne prendrai pas le risque de vouloir les citer, ne m'en voulez pas, vous vous reconnaissez forcément.

La thèse a été égaillée par les enseignements que j'ai pu donner. Je remercie surtout tous mes étudiants.

Enfin, je remercie mes parents qui m'ont toujours accompagné et encouragé. Malgré la distance qui nous sépare, je n'ai jamais cessé de penser à vous. Papa merci pour être fait du souci pour moi sans jamais me le montrer et pour me procurer ce sentiment d'être unique pour toi.

Il me reste à remercier une personne sans qui tout serait tellement plus difficile. Celui qui a été à mes côtés dans les bons et mauvais moments de ce parcours. Merci donc à Hatem pour avoir toujours su me reconforter, me motiver, ou me distraire. Merci d'avoir été à l'écoute de mes satisfactions (parfois), de mes plaintes (souvent), et d'avoir toujours pris soin de moi. Merci pour ta patience et d'être celui sur qui je peux m'appuyer quoi qu'il arrive.

Pour ceux que j'aurais oublié qu'ils sachent que je les remercie aussi !

Contents

Acronyms	vii
List of Symbols	ix
1 Introduction	1
1.1 Context: composite materials	2
1.2 Scientific locks and solutions	3
1.3 Objective	4
1.4 Outline of thesis	6
2 The Proper Generalized Decomposition	7
2.1 Separated representations and PGD	8
2.2 Illustration of the PGD method	11
2.2.1 Mechanical model	11
2.2.2 Separation of space variables	12
2.2.3 Enriching the approximation basis	13
2.2.4 Alternating direction strategy	14
2.2.5 Convergence criteria	16
2.3 PGD: an efficient solution for parametric models	17
3 Delamination in composite laminates under static loading	23
3.1 Failure Modes of composite materials	24
3.2 Delamination in composite laminates	25
3.3 Overview of fracture mechanics tests	27
3.3.1 The mode I DCB specimen	27
3.3.2 The mode II ELS specimen	28
3.3.3 The mixed mode I/II MMELS specimen	29
3.4 Delamination analysis methods	31
3.4.1 Linear elastic fracture mechanics (LEFM)	31
3.4.2 Damage mechanics approach: cohesive zone model (CZM)	35
3.5 Numerical implementation	44

3.5.1	Kinematics of the interface element	44
3.5.2	Mathematical formulation for cohesive problem with the PGD	44
3.6	Numerical simulations	50
3.6.1	Tests results	52
3.6.2	3D simulation of a DCB test using the PGD	57
4	Delamination in composite laminates under dynamic loading	63
4.1	Why composites are vulnerable to impact damage ?	64
4.2	Low and high velocity impact	65
4.3	Failure mechanisms in low velocity impact	65
4.4	Types of impact response	68
4.5	Problem statement	69
4.5.1	Governing equation of motion	69
4.5.2	Time integration	70
4.5.3	Calculation of the contact force	71
4.5.4	Geometrical modelling and Boundary conditions	73
4.5.5	Numerical simulations	73
5	A multiscale modelling of composite materials with periodic structures	79
5.1	What are multiscale methods?	81
5.2	Heterogeneous materials with a periodic structure	82
5.3	Multiscale methods in computational mechanics	83
5.3.1	Periodic homogenization theory	83
5.3.2	Domain decomposition methods	85
5.3.3	Multigrid methods	92
5.4	A separated representation for 1D domains	94
5.4.1	Separated description of the 1D problem	94
5.4.2	First iteration	96
5.4.3	Other iterations	99
5.4.4	Boundary conditions	100
5.5	A separated representation for 2D/3D domains	101
5.5.1	Mechanical model	101
5.5.2	Separated description of 2D problems	102
5.5.3	First iteration and operators assembly	103
5.6	Numerical simulations	105
5.6.1	Numerical results of 2D problem	105
5.6.2	Numerical results of 3D problem	110
6	Conclusions and Perspectives	115
6.1	Conclusions	116
6.2	Perspectives	117

Résumé substantiel	119
Bibliography	139
List of Figures	153
List of Tables	157

Acronyms

ADCB	Asymmetrical Double Cantilever Beam
APHR	A Priori Hyper Reduction
ASTM	American Society for Testing and Materials
BDD	Balancing Domain Decomposition
BDDC	Balancing Domain Decomposition by Constraints
BVID	Barely Visible Impact Damage
CZM	Cohesive Zone Model
DCB	Double Cantilever Beam
DOF	Degrees of Freedom
ELS	End Load Split
ESIS	European Structural Integrity Society
FAS	Full Approximation Scheme
FE	Finite Element
FEM	Finite Element Method
FETI	Finite Element Tearing and Interconnecting
FETI-DP	Dual-Primal Finite Element Tearing and Interconnecting
FOD	Foreign Object Debris
IFT	Interlaminar Fracture Toughness
JIS	Japanese Industrial Standards group
LATIN	Large Time INcrement
LEFM	Linear Elastic Fracture Mechanics
MCS	Monte Carlo Simulation
MMELS	Mixed Mode End Load Split
NN	Neural Networks
PDEs	Partial Differential Equations
PGD	Proper Generalized Decomposition
POD	Proper Orthogonal Decomposition
RVE	Representative Volume Element
SIF	Stress Intensity Factor
VCCT	Virtual Crack Closure Technique

List of Symbols

$\mathbf{F} \circ \mathbf{G}$	Hadamard product of the two vectors \mathbf{F} and \mathbf{G}
$\mathbf{F} \otimes \mathbf{G}$	Tensor product
$F \times G$	Scalar product
$\frac{\partial F}{\partial x}$	Partial derivative of F with respect to x
$\frac{dF}{dx} = F_{,x}$	Total derivative of F with respect to x
$\nabla = \left(\frac{\partial}{\partial x}, \frac{\partial}{\partial y}, \frac{\partial}{\partial z} \right)^T$	Gradient operator
$\text{div } \mathbf{F}$	Divergence of a vector \mathbf{F}

$$\mathbf{u} = \underline{u} = \begin{pmatrix} u \\ v \\ w \end{pmatrix} = \begin{pmatrix} u_x \\ u_y \\ u_z \end{pmatrix} \quad \text{Displacement vector}$$

$\boldsymbol{\sigma}$	Stress tensor
$\boldsymbol{\varepsilon}$	Strain tensor
\mathbb{H}	Standard fourth-order elasticity tensor
G	Strain energy release rate
G_I, G_{II}, G_{III}	Strain energy release rate for mode I, II, and III
G_c	Critical strain energy release rate (fracture toughness)
$G_{Ic}, G_{IIc}, G_{IIIc}$	Critical strain energy release rate for mode I, II, and III
$G_{I/IIc}$	Critical strain energy release rate for mixed mode I/II
C	Compliance
K_{iI}	Mode I stress intensity factor
Π	Potential energy
K_I, K_{II}, K_{III}	Initial interface stiffness for mode I, II, and III
σ_c	Critical interfacial normal stress
τ_c	Critical interfacial shear stress

$\delta = \begin{pmatrix} \delta_u \\ \delta_v \\ \delta_w \end{pmatrix}$	Separation (relative displacements at the cohesive interface)
$T = \begin{pmatrix} \sigma \\ \tau \end{pmatrix}$	Cohesive traction
$\delta_c^I, \delta_c^{II}, \delta_c^m$	Critical separation for mode I, II, and mixed mode I/II
$\delta_m^I, \delta_m^{II}, \delta_m^m$	Maximum separation for mode I, II, and mixed mode I/II
δ^m	Mixed mode separation
a	Crack length
a_0	Initial crack length
Δa	Crack extension
l_{cz}	Length of process zone
N_e	Minimum number of elements in the process zone
l_e	Element length in the direction of crack propagation
E	Young's modulus
ν	Poisson's ratio
E_f	Fiber Young's modulus
E_m	Matrix Young's modulus
G_f	Fiber shear modulus
G_m	Matrix shear modulus
V_f	Fiber volume fraction
ν_f	Poisson's ratio of fibers
ν_m	Poisson's ratio of matrix
E_x	Modulus in the fibre direction
E_z, E_y	Moduli in the transverse direction
E_i, ν_i	Young's modulus and Poisson's ratio of the impactor
m_i, R_i	Mass and radius of the impactor
$w_i, \dot{w}_i, \ddot{w}_i$	Displacement, velocity and acceleration of the impactor
w_p	Deflection of the plate at the contact point
F_c	Contact force
F_m	Maximum contact force
k	Modified Hertz constant stiffness
Δt	Time increment
α_0	Permanent indentation
α_{cr}	Critical indentation
α_m	Maximum indentation

Chapter 1

Introduction

*“Education is the most powerful
weapon which you can use to
change the world.”*

Nelson Mandela

Contents

1.1	Context: composite materials	2
1.2	Scientific locks and solutions	3
1.3	Objective	4
1.4	Outline of thesis	6

1.1 Context: composite materials

Composite materials are increasingly used in a wide range of engineering applications including aerospace, aeronautics, automotive, sport equipments and offshore structures to take advantage of their good mechanical properties and weight saving ability. They have played an important role in the development of lightweight structures. Composite materials progressively replace traditional metallic materials due to their high strength-to-weight and high stiffness-to-weight ratios as well as improved corrosion resistance, superior fatigue life, design flexibility, durability, and potential reduction of life cycle cost. During the manufacturing process, composite materials may be formed into a variety of complex shapes.

Despite all their advantages, composites have certain disadvantages as well. The limitations include material degradation due to environmental factors such as temperature and humidity. The temperature resistance of composites is dependent on the matrix material used for binding the fibers. Composites absorb moisture which affects the way they behave.

Composite materials are made by combining two materials, a reinforcement material called fiber and a matrix material. They are connected with each other by means of interfacial bonding. In general, the fibers have very high tensile strength and modulus, but depend on the matrix to provide the transverse and compressive strength contributions. They are responsible for composite's high structural properties. The matrix, which are often a thermoset resins, thermoplastic polymers or metallic, binds together a cluster of fibers having a preferred orientation. The matrix acts as a load transfer medium between fibers and also protects fibers from environmental degradation. It is capable of absorbing energy by deforming under stress. The fibers are generally brittle. Reinforcement materials often used in composite applications are carbon, kevlar, glass and aramids. They can be in the form of long fibers, short fibers or particles. By combining different matrix materials with different reinforcement materials it is possible to obtain a wide range of composites having different mechanical properties.

Laminated composites are widely used because of the familiar manufacturing and mechanical characteristics. The laminates are built up by stacking layers of varying fibre orientations. The stacking sequence is generally given with respect to the primary loading axis of the material. The effective mechanical properties of the laminate vary with the orientations, thicknesses and stacking sequence of the individual layers. This grants the designer some flexibility to tailor the stiffness and strength of the laminate in order to satisfy the structural requirements. The unidirectional laminate exhibit excellent in-plane properties, but poor out-of-plane properties. To reduce the anisotropy of the laminate and provide strength in multiple directions, the fibers are generally laid up in varying configurations of 0° , 90°

and $+/- 45^\circ$ orientations.

With this material design methodology, the material anisotropy and heterogeneity are greatly increased. As a result, various damage modes can occur and these modes often interact. The damaging process in composite structures is of great complexity especially under dynamic solicitations. Organic matrix composites are generally composed of three characteristic scales. The microscopic scale is related to the fibers arrangement in the matrix, the mesoscopic scale is related to the plies and the macroscopic scale is related to the structures. Damages can occur at these three scales:

- Fibers breakage, fibers/matrix debonding and matrix cracking at microscopic scale;
- Delamination at mesoscopic scale;
- Full failure of the laminate at macroscopic scale.

Among these damage modes, delamination, the separation of two adjacent plies in composite laminates, represents one of the most predominant and most severe damage mechanisms.

Experimental tests is an efficient way to assess composite laminates behavior. However, the complex response of composite laminates together with the high costs and limited reproducibility of mechanical tests render experimental approaches expensive and time consuming. The associated costs of these mechanical tests increase rapidly as the complexity level increases. Due to the fact that testing is expensive in terms of both material and time, various numerical methods have been developed in order to replace a part of the physical tests with “virtual mechanical testing”.

1.2 Scientific locks and solutions

The development of efficient simulations for composite structures is a very challenging issue. There are many scientific locks:

- Multiscale simulations require a lot of computational resources and the management of big data. New numerical strategies have to be investigated to improve the performance of multiscale simulations;
- The modeling of damages can also lead to numerical difficulties. For example, the use of cohesive elements is an appealing choice. This kind of elements is particularly well adapted to treat delamination and fibers/matrix decohesion. However, cohesive elements needs very fined meshes to ensure the numerical stability;

- Composite structures have often a small dimension compared to the others (shell or plate structures). When using 3D elements, a fine mesh is required to keep a good precision in the thickness which results in a very high number of elements to cover the entire surface;
- Explicit dynamic calculations lead to a restrictive time step condition and introduce a numerical viscosity. In other hand, the use of implicit scheme causes solving some non linear problems many times. It is a problem, especially when considering the strong non linearity related to damage modeling.

In addition, models and numerical tools must be robust, efficient, and carefully validated against test data to ensure that they are capable of predicting consistently the response of structures in service.

Numerical methods for example, the so called classical methods like finite element method (FEM), can provide an approximate solutions for governing equations of the concerned problem. They convert partial differential equations into a system of algebraic equations, by the discretization of the problem geometry, which are then more easily solved. The number of these algebraic equations is limited by availability of computer storage.

1.3 Objective

The main objective is to develop efficient numerical solvers able to simulate the complex behavior of composite laminates (related with the lock mentioned above) with reasonable computational time and accuracy. To reach this objective, an approach based on reduced modeling is proposed in this work. This approach can reduce by several orders of magnitude the computational time and the memory requirement. The technique proposed is based on a separated representation of the solution. A few solvers exist to compute this kind of solution. Here, the Proper Generalized Decomposition (PGD) will be considered. This numerical method builds the separated representation of the solution using a greedy algorithm with no a priori knowledge of any reduced basis. It enables the reduction in size of multidimensional and parametric problems.

Two main problems are treated in this thesis:

- The modeling of damages and especially delamination;
- The development of a multiscale solver able to account for the interaction between scales.

Delamination modeling

Delamination, also referred to as interfacial cracking, is important because it can significantly reduce the capacity of the laminate to carry loads. Delamination cracks may propagate without being detected under the action of static or dynamic loads. The resistance to delamination, known as the interlaminar fracture toughness, is generally low. It is an important composite property. Delamination may arise under various circumstances, such as mechanical loading, low velocity impacts, temperature fluctuations that induce normal and/or shear stresses at the interfaces. It may cause local buckling, drastic reduction of the bending stiffness, catastrophic loss of compressive strength, excessive vibrations and reduction of fatigue life. This makes delamination a major obstacle in achieving the full weight saving potential of composite materials. It is then crucial to develop a better understanding of delamination.

When classical computational methods are used to study delamination initiation and propagation in composite laminates, very fine discretization is needed to increase accuracy, with volumic discretization of each ply and use of cohesive interfaces. Therefore, the computational cost and time associated with such modeling for large structures would be prohibitively high. To overcome this limitation, a solver is developed in this thesis based on the Proper Generalized Decomposition under static loading and impact loading.

Multiscale modeling

A simplified model of the composite laminates is used when only the macroscale is considered. In this case, the composite laminates are modeled as a stack of homogeneous orthotropic layers. In reality, each layer of the laminate consists of fiber reinforcement embedded in a matrix material. The fiber reinforcement can be unidirectional (UD), bidirectional (weaves) or randomly oriented (mat). The use of macroscale modeling leads to loss of microscopic information. In addition, a coupling between scales is often observed (the fiber scale, the ply scale and the laminate scale), generating a real need for multiscale models in many applications.

The main difficulty related to multiscale modeling is the need of multiscale solvers that require a lot of computational resources. In order to account for microscopic information and to reduce significantly the cost of a multiscale approach, a new modeling method will be proposed. The main idea is to use the periodicity of the microstructure to separate two scales: the scale of the periodic pattern and the macroscopic scale. This is done using a separated representation of the solution in the context of the proper generalized decomposition.

1.4 Outline of thesis

In order to accomplish the above aim, the work is organised as follows:

In **chapter 2**, we outline the limits of classical discretization methods when dealing with multidimensional and parametric problems. After presenting the proper generalized decomposition method, we detail the different steps necessary to the construction of a solution under a separated form.

In **chapter 3**, the description of the phenomena of delamination under quasi-static loading and the different approaches used in the literature to deal with the problem are addressed. A short review of the the most commonly used delamination tests is given. Various aspects of the cohesive zone modelling technique from basic parameters to its implementation are explained. Finally, all the numerical details of the proposed numerical approach, combining the cohesive zone model (CZM) with proper generalized decomposition (PGD), are presented. The PGD simulations is compared to the classical FEM simulations as well as to analytical solutions.

In **chapter 4**, the same approach described in the previous chapter is adopted to simulate delamination under low velocity impact. A brief literature review on impact and the related damage types is given.

In **chapter 5**, a generic review of multiscale methods in computational mechanics is presented, followed by the description of the numerical implementation of the multiscale separated representation. A comparison is made between the simulations performed with a macroscopically modeled structure and simulations performed with multiscale method.

In **chapter 6**, conclusions and prospects closes the manuscript with an overall summary of the work and a list of potential future developments.

Chapter 2

The Proper Generalized Decomposition

“ If we knew what it was we were doing, it would not be called research, would it? ”

Albert Einstein

Contents

2.1	Separated representations and PGD	8
2.2	Illustration of the PGD method	11
2.2.1	Mechanical model	11
2.2.2	Separation of space variables	12
2.2.3	Enriching the approximation basis	13
2.2.4	Alternating direction strategy	14
2.2.5	Convergence criteria	16
2.3	PGD: an efficient solution for parametric models	17

2.1 Separated representations and PGD

Composite laminates are generally thin structures like plates or shells. In this kind of domains, a 3D finite element simulation can be very costly if we want to have a sufficient number of nodes in the thickness to get the complex stress distributions accurately (shear stress in particular). In a mechanical simulation based on a displacement approach, the unknown field is the displacement vector $u(x, y, z)$. To reduce the cost of shell simulations a reduced basis may be defined over the thickness in order to approximate the solution:

$$u(x, y, z) = \sum_{i=1}^N F_i(x, y) \times G_i(z) \quad (2.1)$$

The function G_i for $i = 1, \dots, N$ are some predefined basis functions. For homogeneous materials, these functions can be derived from the Kirchhoff-Love or Mindlin-Reissner theories of plate. Some sophisticated plate elements can be built from this assumption. If N is small enough, the total number of degrees of freedom is cut down. Only a 2D mesh is required and the problem is greatly simplified in comparison to the full 3D approach. If we want to reduce even more the cost of a 3D computation in plate domain, we can extend the approximation given previously by:

$$u(x, y, z) = \sum_{i=1}^N F_i(x) \times G_i(y) \times H_i(z) \quad (2.2)$$

With this new approximation the number of degrees of freedom can be reduced even more. This kind of separated representations is the basis of model reduction techniques.

Let us describe in a general framework the model reduction techniques. If we are looking for a field (u) that depends on D coordinates (x_1, \dots, x_D) , a separated representation of (u) is built as a finite sum of N functional products (F^i) involving D functions of each coordinate. This can be written as:

$$u(x_1, \dots, x_D) \approx \sum_{i=1}^N F_1^i(x_1) \times \dots \times F_D^i(x_D) \quad (2.3)$$

In transient space/time problems a simple separated representation is:

$$u(x, \dots, t) \approx \sum_{i=1}^N F_1^i(x) \times \dots \times F_2^i(t) \quad (2.4)$$

Assume that some values of $F_1^i(x)$ can be determined for $i = 1, 2, \dots, N$. These values may be used instead of the classical finite element basis functions (the form functions) when solving the transient problem. In this case, the number of DOF

to solve at each time step becomes N and is no more related to the number of nodes. If N is very small compared to number of nodes, the model is reduced and the computational resources required to solve the problem is significantly lower. The functions $F_2^i(t)$ can simply be deduced from the solution of the reduced transient problem. This kind of technique required previously to determine some basis functions $F_1^i(x)$. The reduction is made “a posteriori” ie after an estimation of the basis functions.

To determine the basis functions, an useful tool is the Proper Orthogonal Decomposition (POD), also called the Karhunen-Loève decomposition [Lumley, 1967]. A full non-reduced simulation may be used to compute a sample of discret values (nodal values) of u for different times. This sample is assumed to be representatives of the solution. The Proper Orthogonal Decomposition will extract some orthogonal vectors that are able to approximate the sample of u up to a chosen precision. The so obtained vectors are an excellent choice to form a reduced basis. This basis is optimal: it is the most reduced basis in the sense of the euclidean norm when we want to represent the solution with a given precision. This a posteriori strategy can be used for real time computation or for extrapolation of the results, for instance when the solution is known for some boundary conditions and we want to determine it for some slightly different conditions. To treat parametric problems, some non-incremental Reduced Basis methods have also been developed. The idea is the same as the former POD but the time coordinate is replaced by a parametric coordinate.

Some a priori reduction methods have also been developed in order to avoid the prior need of a sample of the solution. The A Priori Hyper Reduction method (APHR) originally developed by Ryckelynck [Ryckelynck, 2009; Ryckelynck, 2005] is an efficient method able to solve the problem and build the reduced basis at the same time. The reduced basis is updated during the simulation when the norm of the residual exceeds a given tolerance. A finite element calculation is generally used to enrich the basis. The Hyper Reduction consists in the definition of reduced integration domain in which the equations are integrated. This is interesting for materials with complex non linear behaviours. As the POD, the APHR is an incremental method with a space/time representation. This method isn't well adapted to treat multi-dimensional problems.

Another recent a priori model reduction technique is more adapted to treat multi-dimensional problems. It is called Proper Generalized Decomposition (PGD) and is also based on the separated representation of the unknown field. The advantage of the PGD is that it isn't an incremental method and thus is not restricted to space/time separated representation. The aim of this method is to build directly the separated representation.

The PGD with a space-time separated representation was originally proposed by P. Ladeveze under the name “radial loading decomposition” in the context of the LATIN method. The idea was to develop a non-incremental solver [Ladeveze and Nouy, 2003; Ladeveze et al., 2010]. A. Ammar et al. [Ammar et al., 2006; Ammar et al., 2007] devised the first version of the PGD strategy for multi-dimensional problems. It was originally applied to the high-dimensional kinetic models of complex fluids. After that, the PGD was successfully applied to a wide variety of problems. For instance, the PGD procedure was applied by A. Ammar et al. [Ammar et al., 2012] to model the degradation of a plastic material which is a complex transient problem. A separated representation was also used by F. Chinesta et al. for solving the chemical master equation [Chinesta et al., 2010a] and stochastic equations within the brownian configuration field framework [Chinesta et al., 2007]. The PGD was applied in other studies for thermal problems in composite materials [Pruliere et al., 2010b]. A. Nouy used the PGD to study stochastic problems [Nouy, 2008; Nouy and Maitre, 2009]. The PGD approach constitute a new paradigm in scientific computing, allows the reduction in size of the multidimensional and parametric problems [Chinesta et al., 2010b; Pruliere et al., 2010a] and makes possible to solve models never until now solved.

This approach also allows for a fast computation of problems defined in plate or shell domains with significant computing time saving with respect to a standard mesh-based discretization technique. The advantage is that 3D solutions can be obtained with a computational cost characteristic of standard 2D solutions [Bognet et al., 2012]. The idea is to compute full 3D solutions (instead of shell models) using in-plane/out-of-plane separated representation. This approach has been applied to composites shell structures [Pruliere, 2014] and have been improved using high order interpolation in the thickness [Vidal et al., 2012; Vidal et al., 2013].

To solve a problem using the PGD, the functions F_j^i defined in the separated representation Eq. 2.3 have to be determined. These functions are computed by introducing the separated representation into the weak form of the problem and then the resulting nonlinear equations are solved. The PGD method often yields accurate solutions with a small number of terms N . For problems defined in a space of dimension D , if M nodes are used to discretize each coordinate, the total number of unknowns involved in the solution is $M.D$ instead of the M^D degrees of freedom involved in standard mesh-based discretizations. The key of the method is its ability to reduce the number of degrees of freedom: the complexity of the model scales linearly when D increases.

2.2 Illustration of the PGD method

In what follows we are illustrating the construction of the Proper Generalized Decomposition of a generic model defined in a 2D domain.

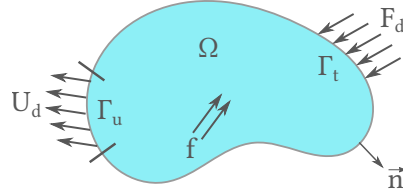


Figure 2.1 – Problem definition.

2.2.1 Mechanical model

We consider the displacement field \mathbf{u} of an elastic body defined in a domain $\Omega \in \mathbb{R}^2$. It is subject to prescribed displacements \mathbf{U}_d on part of its boundary Γ_u , to loads \mathbf{F}_d on another part of its boundary Γ_t and to a body force \mathbf{f} , as shown in Figure 2.1. The strong form of the static equilibrium equation can then be formulated as follows:

$$\begin{aligned} \nabla \cdot \boldsymbol{\sigma}(\mathbf{u}(x, y)) + \mathbf{f} &= 0, & \forall (x, y) \in \Omega \\ \boldsymbol{\sigma}(\mathbf{u}(x, y)) \cdot \mathbf{n}(x, y) &= \mathbf{F}_d, & \forall (x, y) \in \Gamma_t \\ \mathbf{u}(x, y) &= \mathbf{U}_d, & \forall (x, y) \in \Gamma_u \end{aligned} \quad (2.5)$$

where \mathbf{n} is the unit normal direction pointing outward at the boundary Γ_t . For linear elastic homogeneous materials, the stress tensor $\boldsymbol{\sigma}$ is connected with the strain tensor $\boldsymbol{\varepsilon}$ by the standard fourth-order elasticity tensor \mathbb{H} (Hooke's law).

$$\boldsymbol{\sigma} = \mathbb{H} : \boldsymbol{\varepsilon} \quad (2.6)$$

This relation can be written using matrix notations:

$$\begin{bmatrix} \sigma_{xx} \\ \sigma_{yy} \\ \sigma_{xy} \end{bmatrix} = \mathbb{H} \cdot \begin{bmatrix} \varepsilon_{xx} \\ \varepsilon_{yy} \\ 2 \cdot \varepsilon_{xy} \end{bmatrix} \quad (2.7)$$

By multiplying the strong form (Eq. 2.5) by a test function (or virtual displacements) \mathbf{u}^* and integrating over the domain Ω , we get the weak form of the equilibrium equation:

$$\iint_{\Omega} (\boldsymbol{\varepsilon}(\mathbf{u}^*) \cdot \mathbb{H} \cdot \boldsymbol{\varepsilon}(\mathbf{u})) d\Omega = \iint_{\Omega} \mathbf{u}^* \cdot \mathbf{f} d\Omega + \int_{\Gamma_t} (\mathbf{u}^* \cdot \mathbf{F}_d) d\Gamma \quad \forall u \in v^d \quad (2.8)$$

$$\forall u^* \in v^0$$

Using the 2D plane strain comporment law, we obtain:

$$\begin{bmatrix} \sigma_{xx} \\ \sigma_{yy} \\ \sigma_{xy} \end{bmatrix} = \begin{bmatrix} H_{11} & H_{12} & 0 \\ H_{12} & H_{22} & 0 \\ 0 & 0 & H_{66} \end{bmatrix} \begin{bmatrix} \varepsilon_{xx} \\ \varepsilon_{yy} \\ 2.\varepsilon_{xy} \end{bmatrix} \quad (2.9)$$

For an orthotropic material, \mathbb{H} is defined by:

$$\mathbb{H}^{-1} = \begin{bmatrix} \frac{1}{E_x} & -\frac{\nu_{xy}}{E_x} & 0 \\ -\frac{\nu_{xy}}{E_x} & \frac{1}{E_y} & 0 \\ 0 & 0 & \frac{1}{G_{xy}} \end{bmatrix} \quad (2.10)$$

Where E_x , E_y , ν_{xy} and G_{xy} are the material parameters (elastic modulus, Poisson ratio, and shear modulus).

In this present case, the weak form writes:

$$\begin{aligned} \iint_{\Omega} \varepsilon_{xx}^* (H_{11}\varepsilon_{xx} + H_{12}\varepsilon_{yy}) d\Omega + \iint_{\Omega} \varepsilon_{yy}^* (H_{12}\varepsilon_{xx} + H_{22}\varepsilon_{yy}) d\Omega + \iint_{\Omega} 4\varepsilon_{xy}^* H_{66}\varepsilon_{xy} d\Omega \\ = \iint_{\Omega} \mathbf{u}^* \cdot \mathbf{f} d\Omega + \int_{\Gamma_t} \mathbf{u}^* \cdot \mathbf{F}_d d\Gamma \end{aligned} \quad (2.11)$$

The strain-displacement relation, with small strain assumption, is given by:

$$\boldsymbol{\varepsilon} = \frac{1}{2}(\nabla \mathbf{u} + (\nabla \mathbf{u})^T) \quad (2.12)$$

Where ∇ is the gradient operator:

$$\nabla = \left(\frac{\partial}{\partial x}, \frac{\partial}{\partial y} \right)^T \quad (2.13)$$

Then the weak form becomes:

$$\begin{aligned} \iint_{\Omega} H_{11} \frac{\partial u^*}{\partial x} \frac{\partial u}{\partial x} + \iint_{\Omega} H_{22} \frac{\partial v^*}{\partial y} \frac{\partial v}{\partial y} + \iint_{\Omega} H_{12} \left(\frac{\partial u^*}{\partial x} \frac{\partial v}{\partial y} + \frac{\partial v^*}{\partial y} \frac{\partial u}{\partial x} \right) \\ + \iint_{\Omega} H_{66} \left(\frac{\partial u^*}{\partial y} + \frac{\partial v^*}{\partial x} \right) \left(\frac{\partial u}{\partial y} + \frac{\partial v}{\partial x} \right) = \iint_{\Omega} \mathbf{u}^* \cdot \mathbf{f} d\Omega + \int_{\Gamma_t} \mathbf{u}^* \cdot \mathbf{F}_d d\Gamma \end{aligned} \quad (2.14)$$

2.2.2 Separation of space variables

The original two-dimensional rectangular domain Ω of dimension $\Omega_x \times \Omega_y = (0, L) \times (0, H)$ has been transformed within the PGD framework into a two decoupled one-dimensional problems formulated in Ω_x and Ω_y (Figure 2.2). If the unknown field is the displacement \mathbf{u} , we can approximate it by a sum of product of functions, as follows:

$$\mathbf{u} \approx \mathbf{u}^n(x, y) = \sum_{i=1}^n \mathbf{F}_i(x) \circ \mathbf{G}_i(y) \quad \forall (x, y) \in \Omega \quad (2.15)$$

where \circ denotes the Hadamard product.

Eq. 2.15 is equivalent to:

$$\mathbf{u}^n = \begin{pmatrix} u_n(x, y) \\ v_n(x, y) \end{pmatrix} = \sum_{i=1}^n \begin{pmatrix} F_u^i G_u^i \\ F_v^i G_v^i \end{pmatrix} \quad (2.16)$$

Then, the separated representation of the strain tensor gives:

$$\varepsilon(\mathbf{u}^n(x, y)) = \sum_{i=1}^n \begin{pmatrix} F_{u,x}^i G_u^i \\ F_v^i G_{v,y}^i \\ F_u^i G_{u,y}^i + F_{v,x}^i G_v^i \end{pmatrix} \quad (2.17)$$

$f_{,x}$ denotes the derivative of a function f with respect to x .

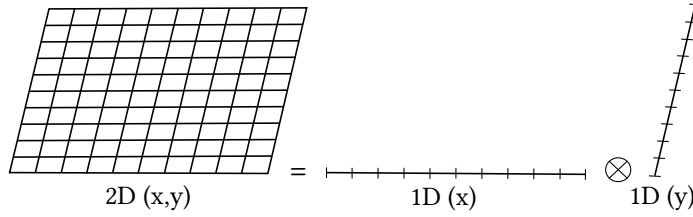


Figure 2.2 – 2D problem separated into two decoupled 1D problems.

2.2.3 Enriching the approximation basis

It is assumed that the first n terms of the approximation (Eq. 2.15) have been determined at previous iterations. At the first iteration, nothing is known a priori. In order to enrich the separated approximation, some new functions F_u^{n+1} , G_u^{n+1} , F_v^{n+1} and G_v^{n+1} have to be determined. The new approximation is then:

$$\mathbf{u}^{n+1}(x, y) = \mathbf{u}^n(x, y) + \begin{pmatrix} F_u^{n+1} G_u^{n+1} \\ F_v^{n+1} G_v^{n+1} \end{pmatrix} \quad (2.18)$$

That can also be written as:

$$\begin{aligned} \mathbf{u}^{n+1}(x, y) &= \mathbf{u}^n(x, y) + \begin{pmatrix} F_u^{n+1} \\ F_v^{n+1} \end{pmatrix} \circ \begin{pmatrix} G_u^{n+1} \\ G_v^{n+1} \end{pmatrix} \\ &= \mathbf{u}^n(x, y) + \mathbf{F}^{n+1} \circ \mathbf{G}^{n+1} \end{aligned} \quad (2.19)$$

The strain derived from Eq. 2.17 is:

$$\varepsilon(\mathbf{u}^{n+1}(x, y)) = \varepsilon(\mathbf{u}^n(x, y)) + \varepsilon(\mathbf{F}^{n+1} \circ \mathbf{G}^{n+1}) \quad (2.20)$$

And test function \mathbf{u}^* is defined from the separated representation:

$$\begin{aligned} \mathbf{u}^*(x, y) &= \begin{pmatrix} F_u^{n+1*}(x) G_u^{n+1}(y) + F_u^{n+1}(x) G_u^{n+1*}(y) \\ F_v^{n+1*}(x) G_v^{n+1}(y) + F_v^{n+1}(x) G_v^{n+1*}(y) \end{pmatrix} \\ &= \mathbf{F}^{n+1*} \circ \mathbf{G}^{n+1} + \mathbf{F}^{n+1} \circ \mathbf{G}^{n+1*} \end{aligned} \quad (2.21)$$

2.2.4 Alternating direction strategy

Finding the couple of functions $(\mathbf{F}^{n+1}, \mathbf{G}^{n+1})$ is a highly non-linear problem. For that purpose, an alternating directions strategy is used. It proceeds as follows: At each iteration, a single function \mathbf{F}^{n+1} and \mathbf{G}^{n+1} is computed alternately assuming the other is known. This procedure continues until reaching convergence. So there are two steps:

1. Step 1: finding \mathbf{F}^{n+1} assuming \mathbf{G}^{n+1}

2. Step 2: finding \mathbf{G}^{n+1} assuming \mathbf{F}^{n+1}

At the beginning of the procedure, the functions \mathbf{F}^{n+1} and \mathbf{G}^{n+1} are initialized with some arbitrary functions. In practice, the initialization values have a weak impact on the convergence.

Step 1 In step 1, \mathbf{G}^{n+1} is assumed known and \mathbf{F}^{n+1} is being searched for. As \mathbf{G}^{n+1} is known, only the test function F_u^{n+1*} is considered. Then the test function becomes:

$$\mathbf{u}^*(x, y) = \begin{pmatrix} F_u^{n+1*}(x)G_u^{n+1}(y) \\ F_v^{n+1*}(x)G_v^{n+1}(y) \end{pmatrix} = \mathbf{F}^{n+1*} \circ \mathbf{G}^{n+1} \quad (2.22)$$

Implying the strain tensor,

$$\varepsilon(\mathbf{u}^*(x, y)) = \varepsilon(\mathbf{F}^{n+1*}(x) \circ \mathbf{G}^{n+1}(y)) = \begin{pmatrix} F_{u,x}^{n+1*} G_u^{n+1} \\ F_v^{n+1*} G_{v,y}^{n+1} \\ F_u^{n+1*} G_{u,y}^{n+1} + F_{v,x}^{n+1*} G_v^{n+1} \end{pmatrix} \quad (2.23)$$

Substituting of Eqs. 2.18 and 2.22 into Eq. 2.14, we define the function A such as:

$$\begin{aligned}
A(\mathbf{F}^{i*}, \mathbf{F}^j, \mathbf{G}^i, \mathbf{G}^j) &= H_{11} \left[\int_{\Omega_x} \frac{dF_u^{i*}}{dx} \frac{dF_u^j}{dx} \right] \times \left[\int_{\Omega_y} G_u^i G_u^j \right] \\
&+ H_{22} \left[\int_{\Omega_x} F_v^{i*} F_v^j \right] \times \left[\int_{\Omega_y} \frac{dG_v^i}{dy} \frac{dG_v^j}{dy} \right] \\
&+ H_{12} \left[\int_{\Omega_x} F_v^{i*} \frac{dF_u^j}{dx} \right] \times \left[\int_{\Omega_y} \frac{dG_v^i}{dy} G_u^j \right] \\
&+ H_{12} \left[\int_{\Omega_x} \frac{dF_u^{i*}}{dx} F_v^j \right] \times \left[\int_{\Omega_y} G_u^i \frac{dG_v^j}{dy} \right] \\
&+ H_{66} \left[\int_{\Omega_x} F_u^{i*} F_u^j \right] \times \left[\int_{\Omega_y} \frac{dG_u^i}{dy} \frac{dG_u^j}{dy} \right] \\
&+ H_{66} \left[\int_{\Omega_x} F_u^{i*} \frac{dF_v^j}{dx} \right] \left[\int_{\Omega_y} \left(\frac{dG_u^i}{dy} G_v^j \right) \right] \\
&+ H_{66} \left[\int_{\Omega_x} \frac{dF_v^{i*}}{dx} F_u^j \right] \left[\int_{\Omega_y} \left(G_v^i \frac{dG_u^j}{dy} \right) \right] \\
&+ H_{66} \left[\int_{\Omega_x} \frac{dF_v^{i*}}{dx} \frac{dF_v^j}{dx} \right] \times \left[\int_{\Omega_y} G_v^i G_v^j \right]
\end{aligned} \tag{2.24}$$

With this function, the weak form using the separated representation reads:

$$A(\mathbf{F}^{n+1*}, \mathbf{F}^{n+1}, \mathbf{G}^{n+1}, \mathbf{G}^{n+1}) = \iint_{\Omega} \mathbf{u}^* \cdot \mathbf{f} \, d\Omega + \int_{\Gamma_t} \mathbf{u}^* \cdot \mathbf{F}_d \, d\Gamma - \sum_{i=1}^n A(\mathbf{F}^{n+1*}, \mathbf{F}^i, \mathbf{G}^{n+1}, \mathbf{G}^i) \tag{2.25}$$

In the right part of this equation, every terms are known. In Eq. 2.24 the integrals over Ω_y can be approximated numerically because the functions G_i are known $\forall i$. It remains only a problem defined over Ω_x . This reduces significantly the complexity of the problem.

Step 2 In step 2, \mathbf{F}^{n+1} is assumed known and \mathbf{G}^{n+1} is being searched for. Then the test function becomes:

$$\mathbf{u}^*(x, y) = \begin{pmatrix} F_u^{n+1}(x) G_u^{n+1*}(y) \\ F_v^{n+1}(x) G_v^{n+1*}(y) \end{pmatrix} = \mathbf{F}^{n+1} \circ \mathbf{G}^{n+1*} \tag{2.26}$$

implying the following strain tensor,

$$\varepsilon(\mathbf{u}^{n*}(x, y)) = \varepsilon(\mathbf{F}^{n+1}(x) \circ \mathbf{G}^{n+1*}(y)) = \begin{pmatrix} F_{u,x}^{n+1} G_u^{n+1*} \\ F_v^{n+1} G_{v,y}^{n+1*} \\ F_u^{n+1} G_{u,y}^{n+1*} + F_{v,x}^{n+1} G_v^{n+1*} \end{pmatrix} \tag{2.27}$$

Now, the weak form using the separated representation becomes:

$$A(\mathbf{F}^{n+1}, \mathbf{F}^{n+1}, \mathbf{G}^{n+1*}, \mathbf{G}^{n+1}) = \iint_{\Omega} \mathbf{u}^* \cdot \mathbf{f} \, d\Omega + \int_{\Gamma_t} \mathbf{u}^* \cdot \mathbf{F}_d \, d\Gamma - \sum_{i=1}^n A(\mathbf{F}^{n+1}, \mathbf{F}^i, \mathbf{G}^{n+1*}, \mathbf{G}^i) \quad (2.28)$$

The integrals over Ω_x can be approximated numerically because the functions F_i are known $\forall i$. It remains only a problem defined over Ω_y which can be solved using any suitable discretization technique (finite elements, finite volumes, ...).

The PGD solution involve a series of decoupled one-dimensional problems formulated in each subdomain. In this work, a finite element discretization is considered. Therefore, the solving of high-dimensional problems with the PGD is reduced to the solving of a series of simple 1D problems.

2.2.5 Convergence criteria

Starting with an arbitrary tentative functions \mathbf{G}^{n+1} , step 1 is performed and then step 2, and again both steps until reaching convergence of the alternate directions strategy. The convergence is obtained when the norm of the difference between the two last values of \mathbf{F}^{n+1} and \mathbf{G}^{n+1} are sufficiently small:

$$\frac{\iint_{\Omega} (\mathbf{F}^{n+1(i)}(x) \circ \mathbf{G}^{n+1(i)}(y) - \mathbf{F}^{n+1(i-1)}(x) \circ \mathbf{G}^{n+1(i-1)}(y))^2 \, d\Omega}{\iint_{\Omega} (\mathbf{F}^{n+1(i)}(x) \circ \mathbf{G}^{n+1(i)}(y))^2 \, d\Omega} \leq \varepsilon_{\text{fixed point}} \quad (2.29)$$

If the new term (n+1) is converged, it is added to the solution:

$$\mathbf{u}^{n+1}(x, y) = \mathbf{u}^n(x, y) + \mathbf{F}^{n+1(i)} \circ \mathbf{G}^{n+1(i)} \quad (2.30)$$

The enrichment procedure must continue until reaching the global convergence (that must be differentiated from the convergence of the alternating direction strategy). The convergence criterion is based on the norm of the residual.

The residual is computed from the finite element operators on each subspace.

$$\frac{\iint_{\Omega} (\text{div}(\mathbb{H} \cdot \boldsymbol{\varepsilon}(\mathbf{u}^{n+1}(x, y))) - \mathbf{f})^2 \, d\Omega}{\iint_{\Omega} (\mathbf{f})^2 \, d\Omega} \leq \varepsilon_{\text{residual}} \quad (2.31)$$

The PGD strategy is shown as a flow chart algorithm in Figure 2.3.

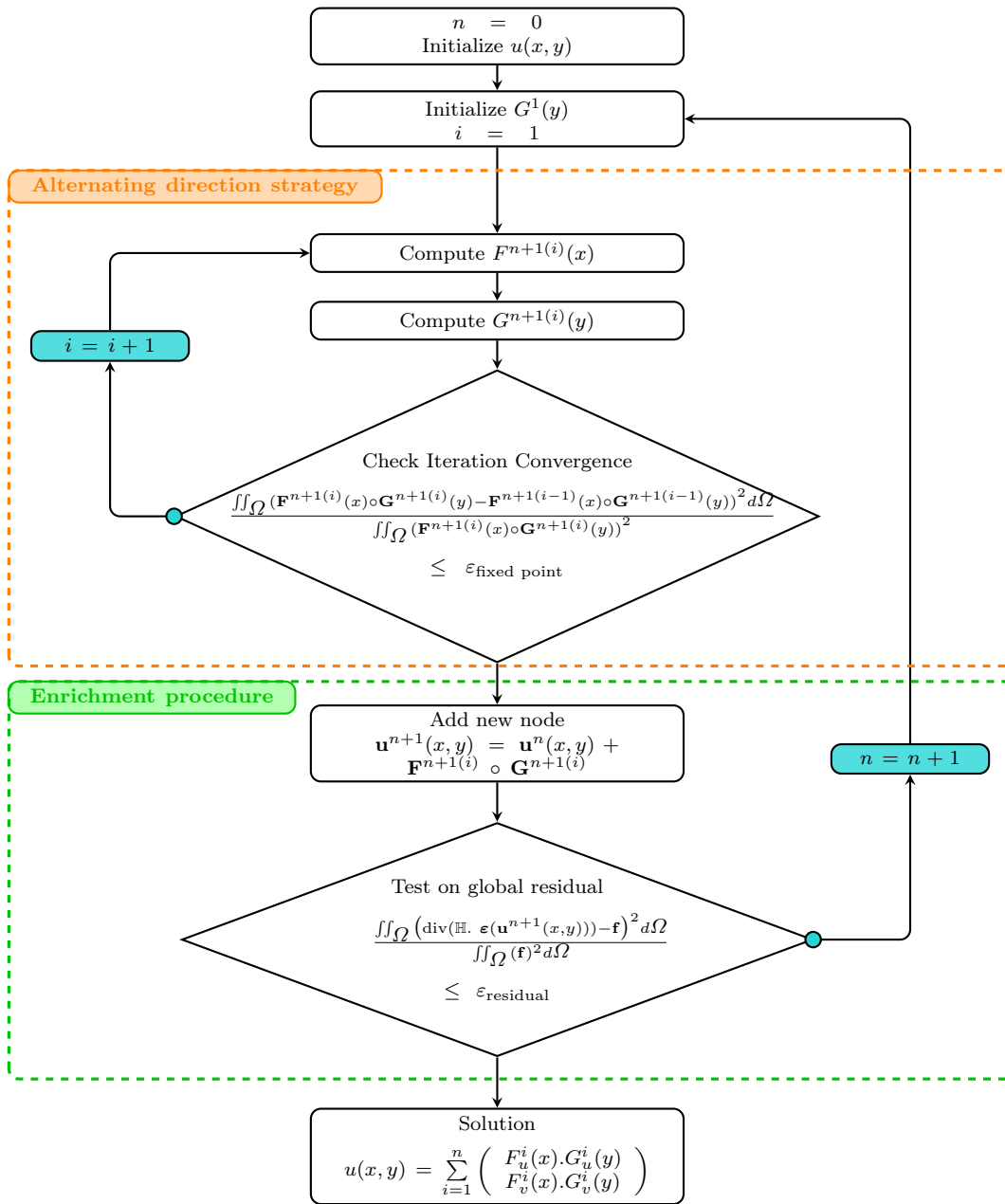


Figure 2.3 – Algorithm of solution by PGD strategy.

2.3 PGD: an efficient solution for parametric models

A major problem in the use of computer models to predict the mechanical behavior of structures is that the problem parameters are fraught with uncertainties, which generate dispersed mechanical behaviors. Accounting for these uncertainties and variability appears today as a crucial point in numerous branches of science and

engineering.

In order to illustrate this idea, let us have a look at the morphology of composite materials. These materials present some different sources of variability at different scales. The manufacturing process and the properties of the elementary constituents are in fact the principal cause of variability. The uncertainty sources can be modeled with a finite set of random variables. Several techniques, like neural networks (NN) and Monte Carlo simulations (MCS), have been proposed in order to propagate these uncertainties and to estimate their impact on the response of the model.

However, these techniques requires a huge number of calculations, which leads to high computational costs. Therefore, the PGD method is more promising when parametric models are addressed. The main idea consists in incorporating the random parameters into the coordinates of the model. The model parameters (materials properties, geometrical parameters, boundary conditions ...) could be considered as extra coordinates. This method drastically reduces computational costs and memory requirements of classical resolution techniques. The increase of the dimensionality of the resulting model does not significantly affect the possibility of computing the solution thanks to the PGD solver. By solving the resulting multidimensional model, we can have access to the model solution for any value of the model parameters. Thus, one may for example consider the Young's modulus of the fibers and the matrix (E_f and E_m) as extra-coordinates allowing the prediction of the displacement field u for any value of E_f and E_m through the solution of a single problem.

To illustrate this approach, we are considering a virtual microstructure (unit cell) of unidirectional carbon/epoxy material composed of 9 fibers (Figure 2.4). We apply the PGD method to simulate of the linear elastic behavior of this virtual unit cell. The virtual unit cell was presumed representative of the microstructure of the analyzed material.

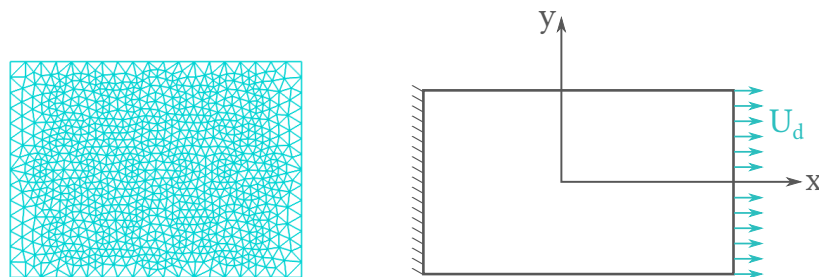


Figure 2.4 – Problem geometry and boundary conditions.

We are assuming that the Young's modulus of the matrix takes values in the inter-

val $\mathcal{I}_m = [3000 \text{ MPa}, 5000 \text{ MPa}]$, whereas the Young's modulus E_{fj} of each fiber j (with $j = 1, \dots, 9$) takes values in the interval $\mathcal{I}_{fj} = [220 \text{ GPa}, 250 \text{ GPa}]$.

In order to introduce another type of variability, which is the variation of the number of fibers in the virtual unit cell, two values were added to the interval \mathcal{I}_{fj} . These values are the minimum and maximum values of the given interval \mathcal{I}_m ($E_m^{\min} = 3000 \text{ MPa}$ and $E_m^{\max} = 5000 \text{ MPa}$). For example, if the Young's modulus of one of fibers will be equal to the Young's modulus of the matrix, the simulations will then be performed with a virtual cell composed of 8 fibers, as shown in Figure 2.6.

The unknown field u depends on the physical coordinates (x, y) , but also on the properties of the elementary constituents (E_m and E_{fj}). In the context of the PGD, u is approximated it by a sum of product of functions, as follows:

$$u(x, y, E_m, E_{fj}) \simeq \sum_{i=1}^N \left(F^i(x, y) G^i(E_m) \prod_{j=1}^9 H_j^i(E_{fj}) \right) \quad (2.32)$$

This parametric solution is defined in a space of dimension 12. The different functions involved in the separated representation are calculated by applying the PGD strategy previously described.

The applied load consists of a uniform displacement U_d applied on the right face of the virtual cell, as shown in Figure 2.4. When the parametric solution (2.32) has been computed, the displacement field u can be obtained for any configuration $E_m \in \mathcal{I}_m$ and $E_{fj} \in \mathcal{I}_{fj}$ by simple postprocessing. The PGD solution is depicted for two configurations in Figures 2.5 and 2.6.

In Figure 2.5, the displacements u_x and u_y , the stress σ_{xx} and the strain ε_{xx} are depicted for 9 fibers with some random values of the parameters. The same results are shown in Figure 2.6 with only 8 fibers. The property of the 9th fiber (central fiber) is set to be the same as the matrix (3 GPa). This corresponds to a case where this fiber is replaced by the matrix.

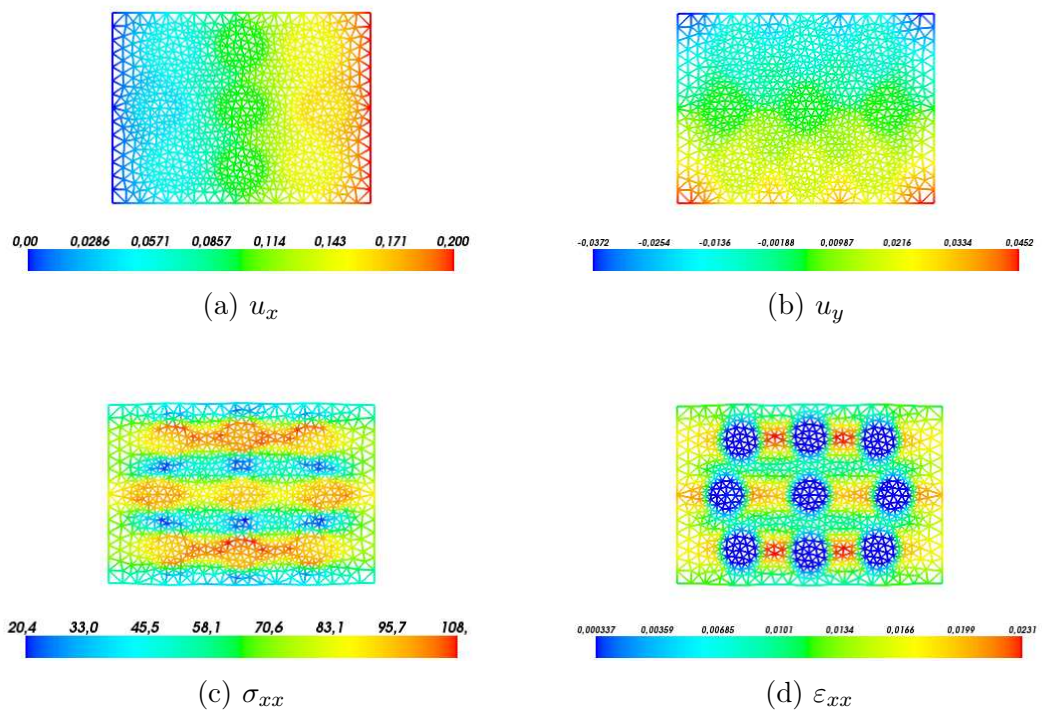


Figure 2.5 – PGD parametric solution for $E_m = 3.8$, $E_{f1} = 228.92$, $E_{f2} = 221.48$, $E_{f3} = 246.9$, $E_{f4} = 237.6$, $E_{f5} = 223.65$, $E_{f6} = 242.25$, $E_{f7} = 225.51$, $E_{f8} = 234.5$, $E_{f9} = 250$ (GPa).

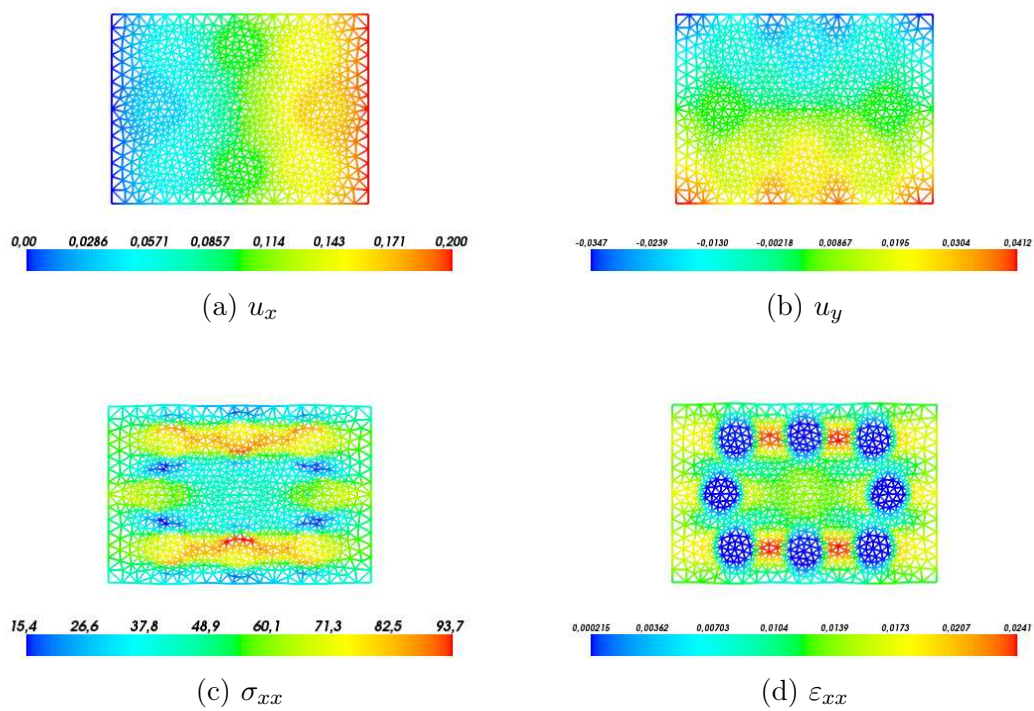


Figure 2.6 – PGD parametric solution for $E_m = 3$, $E_{f1} = 220.554$, $E_{f2} = 225.89$, $E_{f3} = 240.7$, $E_{f4} = 228.61$, $E_{f5} = 249.07$, $E_{f6} = 236.05$, $E_{f7} = 246.59$, $E_{f8} = 232.95$, $E_{f9} = 3$ (GPa).

Chapter 3

Delamination in composite laminates under static loading

“ The good thing about science is that it’s true whether or not you believe in it. ”

Neil deGrasse Tyson

Contents

3.1	Failure Modes of composite materials	24
3.2	Delamination in composite laminates	25
3.3	Overview of fracture mechanics tests	27
3.3.1	The mode I DCB specimen	27
3.3.2	The mode II ELS specimen	28
3.3.3	The mixed mode I/II MMELS specimen	29
3.4	Delamination analysis methods	31
3.4.1	Linear elastic fracture mechanics (LEFM)	31
3.4.2	Damage mechanics approach: cohesive zone model (CZM)	35
3.5	Numerical implementation	44
3.5.1	Kinematics of the interface element	44
3.5.2	Mathematical formulation for cohesive problem with the PGD	44
3.6	Numerical simulations	50
3.6.1	Tests results	52
3.6.2	3D simulation of a DCB test using the PGD	57

Delamination failure is one of the predominant forms of failure in composite laminates, that should be investigated deeply. The aim of this chapter is to develop and investigate a new approach based on reduced order modeling, in order to simulate this kind of failure. Before describing the proposed method, a literature review of the fracture process, the principles of the delamination mechanics and the different models available will be addressed.

3.1 Failure Modes of composite materials

There are many kinds of failure and damage modes in composite structures. This is due to the heterogeneous structure of composites. The fracture process is quite complex and it involves intralaminar damage mechanisms, like matrix cracking or fiber fracture, and interlaminar damage, which is the delamination. Damage is a multi-scale phenomenon that occurs from the microscopic scale (μm) to structural scale (m), as shown in Figure 3.1. All failure modes have a scale of action [Kur-

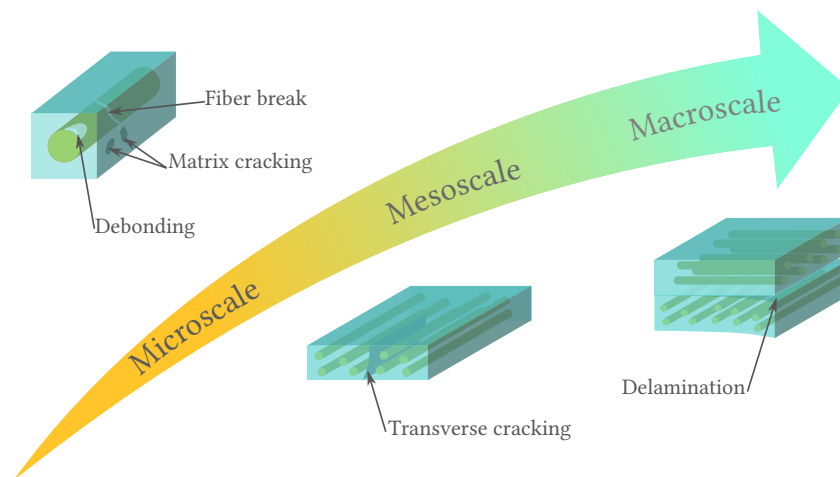


Figure 3.1 – Illustration of the major failure modes in composite laminates.

natowski and Matzenmiller, 2012]. The damage process in laminated composites has a progressive nature [Ochoa and Engblom, 1987; Chen et al., 2014]. This process involves the accumulation of several types of damage. This accumulation has a direct impact on the response of the material [Lee, 1982; Joffe, 1999]. However, it is important to understand the factors influencing damage development under various loading and environmental conditions.

Static damage evolution in unidirectional composites

Under quasi-static loading, the extent of each failure mode may vary from ply to ply depending on the stacking sequence and loading directions. For in-plane

tension loading, the first type of damage to appear is the matrix failure in regions of high stress gradients. In transverse loading direction, especially in 90° , transverse matrix cracking can occur [McCartney, 1998]. On the other hand for 0° plies, the matrix shear cracks develop between fiber pairs. As matrix damage accumulates, the loads are transferred to the plies with fiber orientation aligned close to the direction of applied loads [Zubillaga et al., 2015]. The fiber/matrix interfaces are fractured in these plies. This is accompanied by the fracture of the fibers. For out-of-plane tension loading, delamination failure occurred which can be defined as separation of two adjacent plies [Lorriot et al., 2003; Lagunegrand et al., 2006], as shown in Figure 3.2.



Figure 3.2 – Damage modes in unidirectional carbon/epoxy composite.

3.2 Delamination in composite laminates

Interlaminar failure also referred to as delamination is frequently encountered in composite structures. It is considered to be the most critical mode of failure in composite laminates due to their weak interlaminar properties (strength, energy release rate). Delamination can appear at any moment of the life of the structure [Pagano and Schoeppner, 2000]:

- During the manufacturing stage, due to the shrinkage of the matrix during cooling, or formation of resin-rich areas due to poor quality in laying-up the plies [Bolotin, 1996; Bolotin, 2001];
- During service, internal damage in the interface between plies may arise under various circumstances, such as in the case of low velocity impacts due to the drop of a tool during maintenance.

Delamination can be also caused by the residual stresses due to the differential contractions between plies during the curing process [Tay and Shen, 2002]. These differential contractions are generated by the difference between the thermal coefficients of matrix and reinforcement. The presence of delamination, initiated by transverse matrix cracking leads to stress redistribution between adjacent laminae. Thus, it usually results in a significant loss of stiffness and strength. Delamination may develop under in-plane tensile loads without being detected because it does

not influence the tensile strength performance. However, it can significantly reduce the compressive strength, when compression loads are applied. This characteristic makes the delamination insidious.

Owing to this uncertainty associated with delamination, it is apparent that this failure mode should be identified. As the use of composites increased, it was found that more research was needed on delamination. Understanding the delamination behavior and its internal micro events is therefore of fundamental importance in the development of composite materials, because it is difficult to detect during inspection. Insufficient adhesion at the interface, which is often brittle, is likely to prevent such structures from supporting the expected loadings.

Fracture modes

Generally speaking, the growth or propagation of delamination may develop in any one of or any combination of three basic modes of interlaminar fracture. These modes are mode I, the opening mode, mode II, the in-plane shear mode, and mode III, the out-of-plane shear mode, as shown in Figure 3.3.

- The opening mode (I): fracture mode in which the delamination faces open away from each other and no relative crack face sliding occurs;
- The in plane shear mode (II): fracture mode in which the delamination faces slide over each other in the direction normal to the leading edge and no relative crack face opening occurs;
- The out of plane shear mode (III): fracture mode in which the delamination faces slide over each other in the direction parallel to the leading edge.

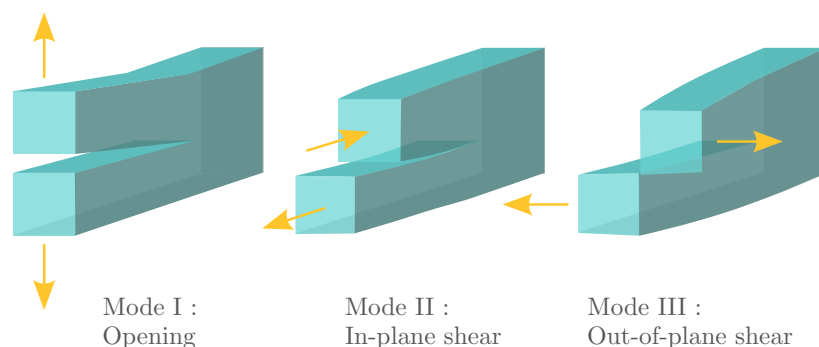


Figure 3.3 – Fracture crack separation modes.

The case where more than one mode of fracture is present is known as mixed mode. The fracture toughness (G_c) is a measure of the total energy necessary for

crack initiation. Thus, there are three G_c values: G_{Ic} , G_{IIc} and G_{IIIc} for mode I, mode II and mode III respectively. Therefore, delamination is prone to appear and propagate if the energy release rate applied to the system equals the fracture toughness ($G \geq G_c$). To understand the nature of delamination fracture and to develop appropriate models to predict this kind of failure, the G_c values must be measured. To measure the interlaminar fracture toughness of composite materials different kinds of experimental methods are available. Generally, delamination are mostly studied under pure modes (I and II) and mixed mode (I/II) [Ding, 1999]. Mode III contribution can be neglected for delamination growth in composite structures [Jensen and Sheinman, 2001; Glaessgen et al., 2002]. The fracture toughness associated to this mode is higher than for the other modes [Glaessgen and Hodgkinson, 2000].

3.3 Overview of fracture mechanics tests for delamination

Similarly to the metals, the failure process in composite materials is investigated by using different type of interlaminar fracture toughness (IFT) testing. The aims for any IFT testing are to obtain a fracture toughness value, that can reliably characterize tested materials for structural applications. A large number of publications address experimental techniques that can be used for each fracture mode. Some of the fracture testing were standardized by three major standardization organizations: the American Society for Testing and Materials (ASTM), the European Structural Integrity Society (ESIS) and the Japanese Industrial Standards group (JIS). The main feature is that they exhibit an artificial defect, which is called the pre-crack.

However, obtaining consistent values for the fracture toughness is not always a straightforward task. The problem lies in the fact that after initiation of the crack in unidirectional composites, the fiber bridging phenomenon may appear at the crack surfaces. This is a phenomenon where fibers are pulled out from the matrix during the crack propagation, as shown in Figure 3.4. The fiber bridging form bundles which can bridge the crack, slow-down its propagation and absorb vast amounts of fracture energy [Tamuzs et al., 2001]. This phenomenon can over estimate fracture toughness [Huang and Hull, 1989]. This is the major cause of resistance to delamination [Airolidi and Dávila, 2012]. In this section, the widely-used interlaminar fracture toughness testing are briefly described.

3.3.1 The mode I DCB specimen

For mode I delamination, the double cantilever beam (DCB) specimen is the most commonly used test to measure the mode I fracture properties [ASTM-D5528-94,

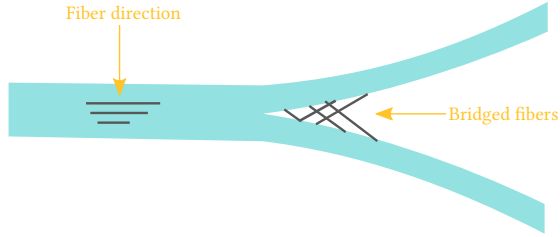


Figure 3.4 – Schematic of fiber bridging.

1997; ASTM-D5528-01, 2003; Davies, 1992]. The simplicity of the DCB test have made it a natural candidate for characterizing mode I delamination in composite materials. The initial crack (a_0) is introduced in the mid-plane of the beam [Davies, 1998]. The initial delamination is forced to grow by applying two opposite forces (P) or displacements (W) that pull the upper and lower parts of the specimen. Several researchers investigated the methods of load applications in the DCB test [Bascom et al., 1980; Chai, 1984; Devitt et al., 1980; Whitney et al., 1982]. A schematic illustration of the DCB test with loading and unloading conditions is given below in Figure 3.5.

The force-displacement response are generated for each crack length during the test. The strain energy release rate G_I , is basically a function of the force, the displacement, the crack length and other material and structural parameters of the specimen. The value of G_I can be calculated from these recorded data using the beam theory. The analytical solutions based on the beam theory approach for the compliance (C) [Valoroso et al., 2013] and on the fracture mechanics for the propagation of delamination are:

$$C = \frac{\delta}{P} = \frac{8a^3}{bE_x h^3} \quad (3.1)$$

$$G_I = \frac{1}{2b} P^2 \frac{dC}{da} = \frac{12P^2 a^2}{b^2 E_x h^3} \quad (3.2)$$

Where E_x is the longitudinal modulus of the material, h is the half-thickness, b the specimen width, a the instantaneous crack length and P the reaction force. The energy G_I can also be expressed as a function of the relative separation (δ) according to:

$$G_I = \frac{3E_x h^3 \delta^2}{16a^4} \quad (3.3)$$

3.3.2 The mode II ELS specimen

The geometry of the end load split (ELS) specimens was the same as that for DCB test. The specimen is loaded applying an external loads or displacements to one

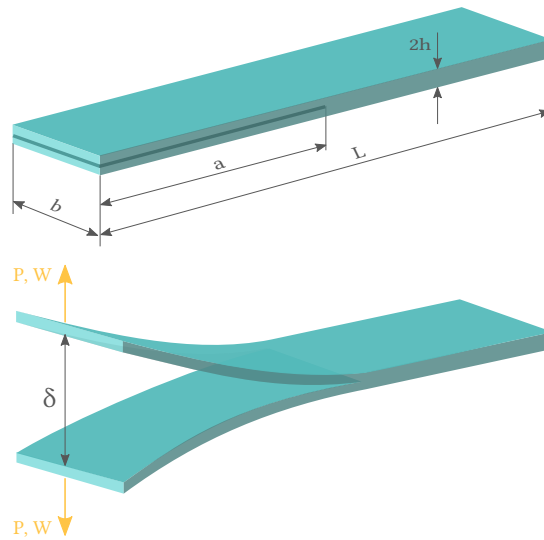


Figure 3.5 – Double cantilever beam specimen.

of the specimen beams [Blackman et al., 2006; de Moura and de Morais, 2008]. Although, only one beam is loaded as shown in Figure 3.6. The pure mode II loading is favored by the relative sliding of the upper surface of the lower beam with respect to the lower surface of the upper beam.

The ELS test allows stable propagation provided that $a_0/L > 0.55$. The relative friction between the two fracture surfaces occurs due to the rotation of the upper and lower beams of the specimen. According to the beam theory approach, the compliance (C) and the analytical energy release rate for the ELS test can be determined as:

$$C = \frac{\delta}{P} = \frac{3a^3 + L^3}{2bE_x h^3} \quad (3.4)$$

$$G_{II} = \frac{9P^2 a^2}{4b^2 E_x h^3} \quad (3.5)$$

Combining both equations gives:

$$G_{II} = \frac{9\delta^2 E_x h^3 a^2}{(3a^3 + L^3)^2} \quad (3.6)$$

3.3.3 The mixed mode I/II MMELS specimen

The mixed mode end load split test (MMELS) test, is also known as asymmetrical double cantilever beam (ADCDB) [Davies, 1992]. Simple to use, it only provides a single ratio of 3/4 of mode II component to mode I component. In this case,

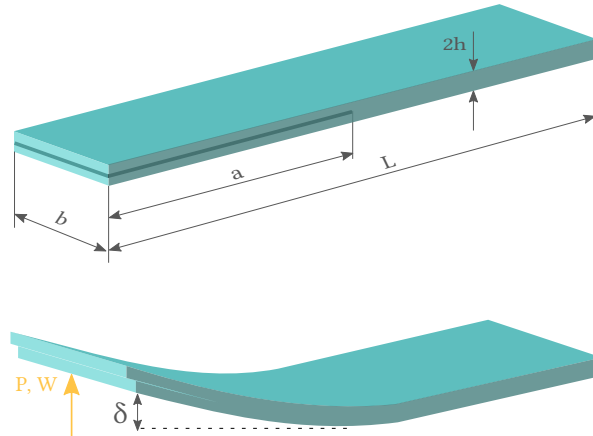


Figure 3.6 – End load split specimen.

the force is applied on the upper beam in the direction of the thickness, while the lower beam remains unloaded [Harper and Hallett, 2008]. Figure 3.7 shows the MMELS specimen and how it is loaded. The initial crack is forced to propagate

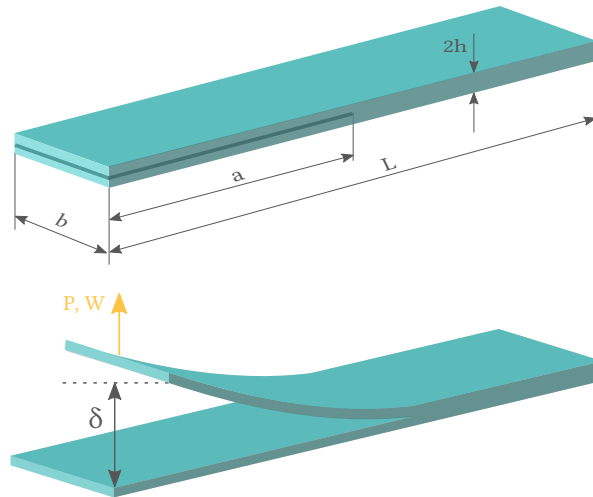


Figure 3.7 – Mixed mode end load split specimen.

by both opening and shearing actions. To ensure the mixed mode, the length of the pre-crack must respect the condition $a_0/L > 0.41$. The analytical expressions for the compliance and for the mode I and mode II energy release rates related to the MMELS test can be given as:

$$C = \frac{7a^3 + L^3}{2bE_x h^3} \quad (3.7)$$

$$G_I = \frac{3P^2 a^2}{b^2 E_x h^3} \quad (3.8)$$

$$G_{II} = \frac{9P^2 a^2}{4b^2 E_x h^3} \quad (3.9)$$

If the thickness of the two layers are equal, the analytical total energy release rate is given by:

$$G_T = G_I + G_{II} = \frac{21E_x h^3 a^2 \delta^2}{(7a^3 + L^3)^2} \quad (3.10)$$

Using the power law interaction between the energies of pure modes (Eq. 3.11), the critical value of the total energy release rate $G_{I/IIc}$ under mixed mode loading can be expressed as follows:

$$\left(\frac{G_I}{G_{Ic}}\right)^2 + \left(\frac{G_{II}}{G_{IIc}}\right)^2 = 1 \quad (3.11)$$

$$G_{I/IIc} = \frac{(1 + \beta^2)G_{Ic}G_{IIc}}{[(G_{IIc})^2 + (\beta^2 G_{Ic})^2]^{1/2}} \quad (3.12)$$

With:

$$\beta^2 = \frac{G_{II}}{G_I} \quad (3.13)$$

3.4 Delamination analysis methods

In addition to experimental methods, numerical methods, such as finite element method, are valuable tools for prediction of fracture in composite materials using fracture mechanics principles. Fracture mechanics was invented by Griffith [Griffith, 1921] to explain the failure of brittle materials. Griffith was focusing on the prediction of crack propagation in deformable body. The use of fracture mechanics for describing and solving crack problems in homogeneous materials is almost mature. However, in heterogeneous materials such as composites, there are interface fracture problems. Conventional fracture mechanics analysis for homogeneous fracture is not sufficient for studying delamination in composite materials. The extension of fracture mechanics to heterogeneous materials interface crack has become of interests. There are two approaches in fracture analysis: the linear elastic fracture mechanics (LEFM) and damage mechanics approach. In this section, a brief background and some basic theory of fracture mechanics for interfaces are given.

3.4.1 Linear elastic fracture mechanics (LEFM)

Linear elastic fracture mechanics was introduced to study and analyse the relationship between crack, stresses and fracture toughness. It has been proven to be reliable in predicting the crack propagation when the nonlinearities are negligible. These nonlinearities are confined to a small zone around the crack tip compared

to the size of the crack.

LEFM assumes that the material is isotropic and linear elastic. Based on this assumption, the stress field and the energy near the crack tip are calculated by means of the theory of elasticity. This theory applies when assuming an initial crack with given size, shape, location and orientation. In reality, location and size of the initial crack is not known a priori. In the LEFM approach, crack growth is predicted when the loading criterion exceed the failure criterion. In general, stress intensity factor (SIF) and energy release rate are used to evaluate failure criteria around the crack tip.

In an energy based fracture criterion, the initial crack will propagate if the energy release rate (G) is equals or exceeds the surface energy required to create new crack surfaces:

$$G \geq G_c \quad (3.14)$$

According to the Griffith energy balance [Anderson, 2005], G is defined by:

$$G = -\frac{d\Pi}{da} \quad (3.15)$$

Where Π is the potential energy per unit width and a is the crack length.

Irwin extended Griffith's work and showed that for a mode I crack, G_I varies directly with the stress intensity factor K_I according to the following equation [Alfredsson and Stigh, 2012]:

$$G_I = \begin{cases} \frac{K_I^2}{E} & \text{plane stress} \\ \frac{(1-\nu^2)K_I^2}{E} & \text{plane strain} \end{cases} \quad (3.16)$$

Where E is the Young's modulus, ν is Poisson's ratio. Irwin also showed that G can be expressed in terms of mode II and mode III stress intensity factors. However, Griffith's approach, based on the energy balance, was not relevant in many fields of engineering because it is restricted to quasi brittle materials.

In the case of ductile materials, the characteristic size of the plastic zone at the crack tip is not negligible in comparison with the crack length. It is referred to as fracture process zone. In this case the stress intensity factor loses any physical sense because of the limited validity of the asymptotic formulae. To overcome this limitation, other techniques will be discussed.

J-Integral technique

The J-integral was proposed by Rice as a way to calculate the energy release rate in a cracked nonlinear elastic material [Rice, 1968]. It was introduced as a path-

independent integral, which can be drawn around the crack tip. For the elastic case, J-integral is identical to the energy release rate for a plane crack [Cherepanov, 1967]. For a 2D case and with reference to Figure 3.8, it can be written as:

$$J = \int_{\Gamma} (Y dy - T_i \frac{\partial U_i}{\partial x} ds) \quad (3.17)$$

Where Y is the strain energy density, $T_i = \sigma_{ij}n_j$ are the components of the traction vector, U_i are the displacement vector components and ds is an incremental length along the contour Γ . The strain energy density Y is given by [Rice, 1968]:

$$Y = \int_0^{\varepsilon_{ij}} \sigma_{ij} d\varepsilon_{ij} \quad i = 1, 2 \quad (3.18)$$

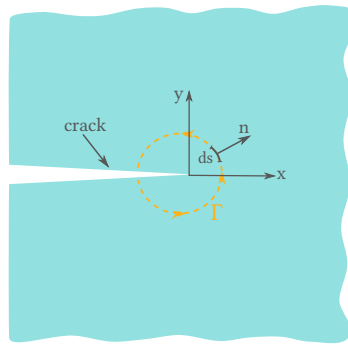


Figure 3.8 – J-integral contour path enclosing the crack tip.

Virtual crack closure technique (VCCT)

The virtual crack closure technique (VCCT) is one of the most widely used techniques for modeling crack propagation in composite materials. It was first proposed by Rybicki and Kanninen for two-dimensional problems [Rybicki and Kanninen, 1977], and later extended to three-dimensional problems by Shivakumar et al. [Shivakumar et al., 1988]. The VCCT approach is based on Irwin's assumptions [Irwin, 1958]:

- The energy released when the crack has been extended from a to $a + \Delta a$ is equal to the work required to close the crack to its original length;
- The crack progression from length a to $a + \Delta a$ does not significantly alter the state at the crack tip.

This technique has gained great popularity for the study of delamination in composite materials. It is used to compute not only the energy release rate along a crack front, but also the contributions of the three fracture modes [Krueger, 2004].

The mode I, mode II and mode III energy release rate, G_I , G_{II} and G_{III} respectively, can be computed from the nodal forces and relative displacements obtained with a finite element simulation [Zou et al., 2001]. The crack tip geometry is shown in Figure 3.9.

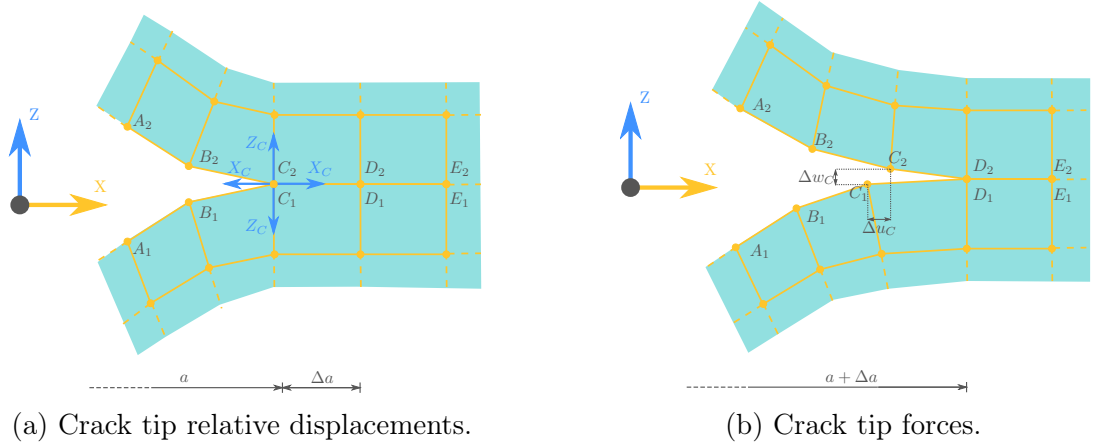


Figure 3.9 – VCCT for 2D 4-node element.

The crack tip is modeled by leaving nodes uncoupled along a crack length a . In two-dimensional plane stress or plane strain model, the mode I and mode II components of the energy release rate, G_I and G_{II} , for a 2D 4-node element are calculated by Eq. 3.19 and Eq. 3.20, respectively.

$$G_I = \frac{1}{2\Delta a} Z_C \Delta w_C \quad (3.19)$$

$$G_{II} = \frac{1}{2\Delta a} X_C \Delta u_C \quad (3.20)$$

Where Z_C and X_C are the magnitudes of nodal forces at nodes C_1 and C_2 in the Z and X directions, respectively. Δw_C and Δu_C are the relative displacements before nodes C_1 and C_2 are pulled together.

$$\Delta w_C = w_{C2} - w_{C1} \quad (3.21)$$

$$\Delta u_C = u_{C2} - u_{C1} \quad (3.22)$$

When crack growth occurs under mixed mode I/II fracture condition:

$$G_T = G_I + G_{II} \quad (3.23)$$

Crack propagation is predicted when the computed energy is equal to the critical value G_c :

$$G_T = G_c \quad (3.24)$$

3.4.2 Damage mechanics approach: cohesive zone model (CZM)

The main drawback of the LEFM is that it cannot be applied without knowledge of initial crack shape, location and geometry. Only crack propagation could be predicted. In this situation, approaches combining a stress criterion to predict the crack initiation, with an energy criterion to model the crack growth have been applied. One of these approaches is the cohesive zone model (CZM). Compared with the VCCT method, the CZM has the capability to predict both onset and propagation of the delamination, in conjunction with a finite element model [Balzani and Wagner, 2008; Tenchev and Falzon, 2006]. With a small nonlinear zone (called the process zone), the linear elastic fracture mechanics has been proven to be reliable to predict crack growth. If this is not the case, the cohesive forces acting in the process zone along the crack path must be considered in the damage model analysis [Borst et al., 2004]. A candidate to achieve this is offered by the damage mechanics approach.

Cohesive zone model (CZM)

The cohesive zone model was introduced by Barenblatt and Dugdale [Barenblatt, 1962; Dugdale, 1960]. The main difference between LEFM and CZM is that the CZM uses an explicit representation of the process zone, while in LEFM is assigned to a point process located at the crack tip [Cox and Yang, 2006], as shown in Figure 3.10. The introduction of cohesive forces acting ahead of the crack allows removal of the crack tip singularity given by LEFM. This singular crack leads to infinite stresses at the crack tip, which is physically not possible.

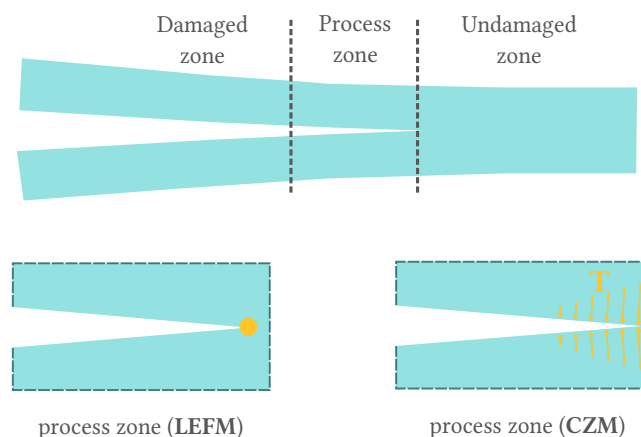


Figure 3.10 – Schematic illustration of fracture process zone.

The CZM is based on the use of interfacial finite elements between two adjacent layers of the laminated composite. These cohesive elements are delimited by two

cohesive surfaces, linked together by cohesive forces. The degradation mechanism in the process zone of a cohesive crack is described by a constitutive law, which links the relative separation (δ) of the cohesive surfaces to the cohesive traction (T), as shown in Figure 3.11.

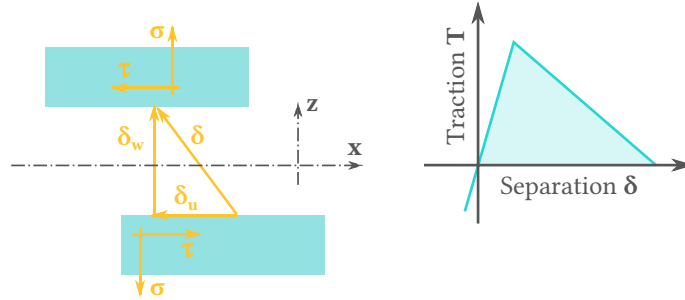


Figure 3.11 – Principle of cohesive crack models.

The separation components of δ are the normal separation δ_w and tangential separation δ_u . The nominal traction vector T , consists of two components in two-dimensional problems: the normal stress σ and the shear stress τ . This constitutive equation is based on the assumption that when the separation between the interfaces increases, the cohesive stresses reach the maximum stresses and then decrease progressively to become equal to zero up to complete fracture. The area under the traction-separation law should be equal to the fracture toughness G_c . The thickness of a cohesive element can be as small as zero before loading is applied.

Several shapes of cohesive zone law, proposed by different authors, are available for describing interfacial behaviors that cannot be captured with fracture mechanics, as shown in Table 3.1. The Dugdale model, introduced in 1960, was for ductile materials [Dugdale, 1960]. In this model, the maximal normal stress in the cohesive zone is constant and equal to the material yield stress. The Barenblatt model, introduced in 1962, investigated the fracture of brittle materials [Barenblatt, 1962]. Barenblatt assumes a nonlinear cohesive forces to be distributed over a sufficiently large zone along the crack plane. The Needleman model (introduced in 1987) was the first, who used polynomial shape of the traction-separation curve to simulate particle/metal matrix decohesion [Needleman, 1987], using the finite element method for the first time [Xu and Needleman, 1994].

Tvergaard and Hutchinson in 1992, proposed a trapezoidal type of cohesive zone model to determine crack growth resistance in elasto-plastic materials [Tvergaard and Hutchinson, 1992]. Camacho and Ortiz (1996) utilized a linear softening cohesive model to simulate multiple cracking along arbitrary paths during impact damage in brittle materials [Camacho and Ortiz, 1996]. A bilinear cohesive model,

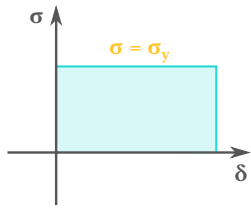
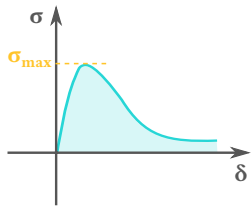
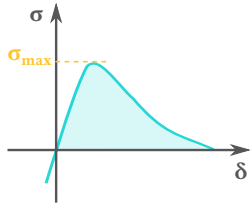
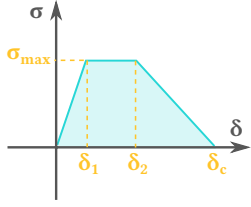
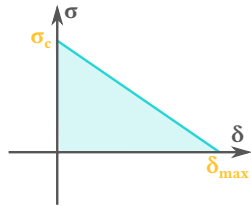
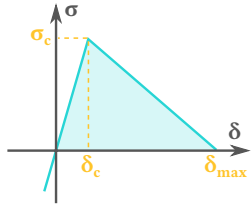
Author and Year	Proposed Model	Cohesive shape	Problem Solved
Dugdale (1960)		Elasto-perfectly-plastic	Yielding of thin ideal elastic-plastic steel sheets containing slits
Barenblatt (1962)		Exponential	Perfectly brittle materials
Needleman (1987)		Polynomial	Particle-matrix decohesion
Tvergaard and Hutchinson (1992)		Trapezoidal	Crack growth in elasto-plastic material, peeling of adhesive joint
Camacho and Ortiz (1996)		Linear softening	Impact damage in brittle materials
Crisfield (1999)		Bilinear softening	Delamination in composite materials

Table 3.1 – Various traction-separation relationships.

was developed by Crisfield (1999) [Chen et al., 1999] and later modified by Alfano and Crisfield (2001) [Alfano and Crisfield, 2001] to simulate initiation and propagation of delamination in composite plates. Some researchers have investigated the effect of the cohesive law shape on numerical results of fracture simulation [Alfano, 2006; Chandra and Shet, 2004; Volokh, 2004].

It was found that the shape of the traction-separation curve makes no vital difference concerning the numerical results. The effect of the cohesive law was found on the degree of accuracy achieved and on the algorithmic numerical performance. It is worth mentioning that in [Alfano, 2006] the trapezoidal law has turned out to give the worst results both in terms of numerical stability and in terms of convergence of the finite element solution. The exponential law was found to be optimal in terms of accuracy while the bilinear law represented the best compromise between computational cost and accuracy.

However, cohesive laws with initial slope, as shown in Figure 3.12, are usually used in numerical simulations. It is interesting to note that an initial slope is appropriate, when the cohesive zone represents an adhesive layer or a resin rich interface between two adjacent layers. In all cohesive models, the traction-separation

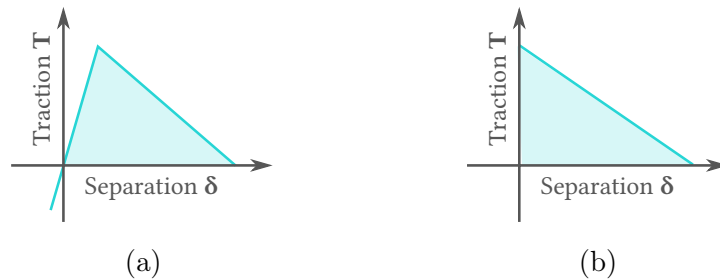


Figure 3.12 – Linear softening: (a) with initial slope, (b) without initial slope.

law can be defined by cohesive parameters. The key cohesive parameters consist of the cohesive strength, defined by the peak cohesive traction and the fracture toughness, represented by the area under the traction-separation curve. The initial stiffness is also a crucial parameter that affects the compliance of the structure. The formulation of the cohesive zone model used in this work is the Crisfield cohesive law [Alfano and Crisfield, 2001] for its robustness and accuracy.

Bilinear traction-separation law

The bilinear cohesive law is well-suited to be implemented in finite element codes. It is widely used for delamination problems in mode I, mode II and mixed mode problems. It involves three stages, initial elastic loading, damage initiation and damage evolution.

Constitutive cohesive law under single mode delamination The Crisfield law is used to describe the behaviour of the interface, which presents linear elastic and linear softening behaviour. The process of degradation begins when the stresses satisfy one imposed damage initiation criterion. The Crisfield law supposes that, under strain reversal, the material unloads toward the origin. A two-parameter bilinear linear cohesive law was defined, for each pure mode.

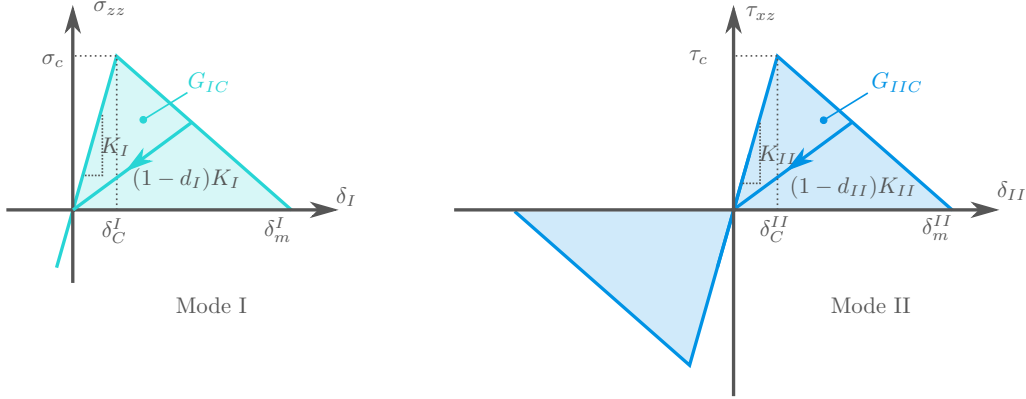


Figure 3.13 – Cohesive law for the mode I and mode II.

These two parameters are the maximum stress (σ_c and τ_c) and the energy release rate (G_{Ic} and G_{IIc}) for respectively mode I and mode II. The critical value of the energy release rate of the interface is equal to the area under the interfacial stress-separation curve. K_I and K_{II} are the interface element stiffness. The critical separations (δ_c^I and δ_c^{II}) are defined when the interfacial stress reaches maximum, and the maximum separations (δ_m^I and δ_m^{II}) are defined when the stress becomes zero. These separations can be evaluated by the following expressions:

$$\delta_c^I = \frac{\sigma_c}{K_I}, \quad \delta_c^{II} = \frac{\tau_c}{K_{II}} \quad (3.25)$$

$$\delta_m^I = \frac{2G_{Ic}}{\sigma_c}, \quad \delta_m^{II} = \frac{2G_{IIc}}{\tau_c} \quad (3.26)$$

The relation between local separation and interface stress, shown in Figure 3.13, can be expressed as:

$$\sigma_{zz}, \tau_{xz} = \begin{cases} K_i \delta_i & \delta_i < \delta_c^i \\ (1 - d_i) K_i \delta_i & \delta_c^i \leq \delta_i < \delta_m^i \\ 0 & \delta_i \geq \delta_m^i \end{cases} \quad (3.27)$$

$$d_i = \frac{\delta_m^i (\delta_i - \delta_c^i)}{\delta_i (\delta_m^i - \delta_c^i)} \quad i = I, II; \quad d_i \in [0, 1] \quad (3.28)$$

Constitutive cohesive law under mixed mode delamination The description of the delamination under mixed-mode loading requires [Lee et al., 2010]:

- The definition of the interfacial stress and the critical energy release rate for each pure mode and;
- The proposition of criteria or laws relating these parameters for mixed loading.

From these laws, the critical and maximum separations (δ_c^m and δ_m^m) under mixed mode loading can be determined, as illustrated in Figure 3.14. Each failure mechanism consists of two parts: a damage initiation criterion and a damage evolution law. The damage initiation can be predicted using the quadratic failure criterion, defined as:

$$\left(\frac{\langle \sigma_{zz} \rangle_+}{\sigma_c} \right)^2 + \left(\frac{\tau_{xz}}{\tau_c} \right)^2 = 1 \quad (3.29)$$

Where $\langle \cdot \rangle_+$ denotes the positive value. This mixed-mode criterion assumes the coupling between the failure modes and considers that compressive normal stress has no influence on the delamination onset. The "power law criterion" appears to be the most advisable in order to predict delamination propagation in carbon/epoxy composite laminates under mixed-mode loading. It states that the damage under mixed loading is governed by a power law interaction between the energies of pure modes, that is:

$$\left(\frac{G_I}{G_{Ic}} \right)^2 + \left(\frac{G_{II}}{G_{IIc}} \right)^2 = 1 \quad (3.30)$$

Where G_I and G_{II} are the energy release rates respectively in mode I and mode II, G_{Ic} and G_{IIc} are the critical energy release rates. The total mixed mode relative displacement δ^m can be defined as the norm of the two normal and tangential relative displacements:

$$\delta^m = \sqrt{\delta_{II}^2 + \langle \delta_I \rangle_+^2} \quad (3.31)$$

Numerical aspects of cohesive zone model

When cohesive zone model are used to simulate fracture problems, the predicted response may be affected by the parameters of the cohesive law. As the size of the process zone increases relative to others geometric lengths, different parameters and features of the cohesive formulation influence the results [Needleman, 2014; Wisnom, 2010; Chandra et al., 2002]. In references [Chandra et al., 2002; Alfano, 2006; P. W. Harper and Hallet, 2012; Gustafson and Waas, 2009; Sills and Thouless, 2013], the authors suggest that all aspects of the cohesive formulation should

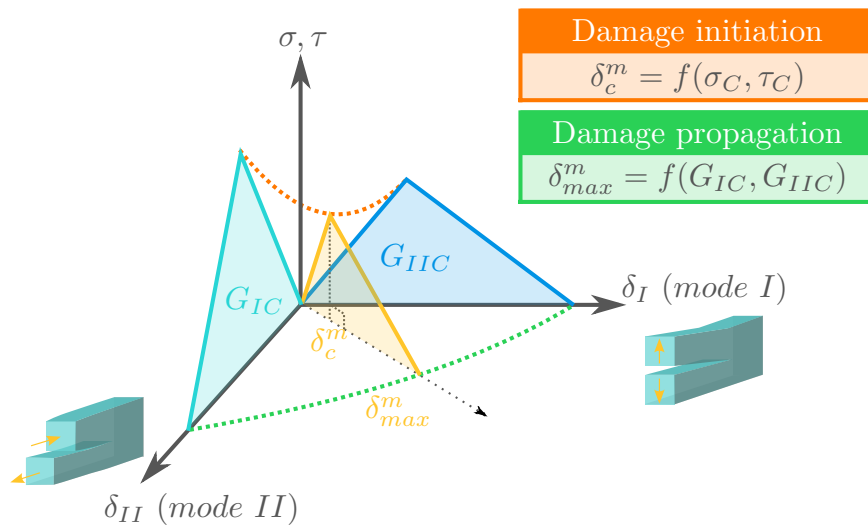


Figure 3.14 – Cohesive law for the mixed mode.

be carefully chosen and some details that seems unimportant significantly affect the global response.

However, to obtain a successful numerical simulation of delamination, an appropriate implementation of CZM is required. For this purpose, the effect of some features of the cohesive law are discussed: the process zone length, the mesh sensitivity, the interfacial strength and the initial stiffness.

Process zone length The use of CZM in a quasi-static finite element framework suffers from an intrinsic mesh sensitivity. It is necessary to have a sufficiently fine discretization within the process zone to capture the stress fields. The required cohesive element size can be precisely determined by evaluating the length of the process zone l_{cz} and the number of elements N_e that are needed in the zone [Song et al., 2008]. The length of the process zone is defined as the distance from the crack tip to the point where the maximum cohesive stress is reached [Turon et al., 2005].

There are different models available in the literature intended to estimate the length of the process zone. For infinite body, l_{cz} is a material property, and can be evaluated by the following expression:

$$l_{cz} = ME \frac{G_c}{\tau_c^2} \quad (3.32)$$

where E is the Young's modulus of the material, G_c is the fracture toughness, τ_c is the critical interfacial strength, and M is a parameter that depends on cohesive

zone formulation used to derive the expression for the process zone length. For the case of orthotropic materials, the value of the Young's modulus in Eq. 3.32 is the transverse modulus of the material, E_{33} .

	l_{cz}	M
Hui et al. [Hui et al., 2003]	$\frac{2}{3\pi} E \frac{G_c}{\tau_c^2}$	0.21
Irwin [Irwin, 1960]	$\frac{1}{\pi} E \frac{G_c}{\tau_c^2}$	0.31
Dugdale [Dugdale, 1960], Barenblatt [Barenblatt, 1962]	$\frac{\pi}{8} E \frac{G_c}{\tau_c^2}$	0.4
Rice [Rice, 1980], Falk et al. [Falk et al., 2001]	$\frac{9\pi}{32} E \frac{G_c}{\tau_c^2}$	0.88
Hillerborg et al. [Hillerborg et al., 1976]	$E \frac{G_c}{\tau_c^2}$	1

Table 3.2 – Length of the process zone and equivalent value of the parameter M .

A general review of various models commonly used in the literature, and the equivalent parameter M for plane stress are presented by Turon et al. [Turon et al., 2005] and summarized in Table 3.2. Hillerborg's model [Hillerborg et al., 1976] and Rice's model [Rice, 1980] are the most commonly used models in the literature. In these models, the parameter M is either close or exactly equal to unity.

Mesh sensitivity The main drawback of the CZM is that very fine meshes are needed to obtain accurate results using FEM. In case of a coarse mesh, softening of the local behavior in an interfacial element will result in a sudden release of the elastic strain energy stored in the surrounding bulk material, which in turn leads to instantaneous failure of the element. In such a case, a non-physical oscillations arises in the numerical solution, which is also known as a solution jump. This leads to convergence problems, numerical instabilities and major difficulties in solving the global system. To overcome these issues, a minimum number of elements N_e is needed in the process zone. The number of elements in this zone is obtained using the following equation [Turon et al., 2005]:

$$N_e = \frac{l_{cz}}{l_e} \quad (3.33)$$

Where l_e is the mesh size in the direction of crack propagation. However, this minimum number is not well established. A summary of different authors' suggestions is shown in Table 3.3. Turon et al. [Turon, 2007] proposed a novel procedure that allows the use of coarser meshes of cohesive elements in large-scale computations.

Moës and Belytschko [Moës and Belytschko, 2002]	$N_e \geq 10$
Turon [Turon, 2007]	$N_e \geq 3$
Falk et al. [Falk et al., 2001]	$2 \leq N_e \leq 5$
Mi et al. [Mi et al., 1998]	$N_e \geq 2$

Table 3.3 – The minimum number of required cohesive elements within the process zone.

Initial interface stiffness The effective elastic properties of the composite depend on the properties of both the cohesive surfaces and the bulk constitutive relations. The elasticity modulus in the direction normal to the interface can be expressed by:

$$E_{eff} = E_z \frac{1}{1 + \frac{E_z}{Kh}} \quad (3.34)$$

Where E_z is the through-the-thickness Young's modulus of the material, h is the thickness of an adjacent sublaminar, and K is the interface stiffness. It is suggested that if the inequality $E_z \ll Kh$ is being accomplished, the effective elastic properties of the composite will not be affected by the cohesive surface [Turon et al., 2005]:

$$K = \alpha \frac{E_z}{h} \quad (3.35)$$

Where α is a parameter much larger than 1 ($\alpha \gg 1$). However, as demonstrated in [Turon, 2007], large values of the interface stiffness may result in spurious stress oscillations that precludes solution convergence. Thus, the authors [Turon, 2007; Song et al., 2008] suggest that K should be large enough to provide a reasonable stiffness but small enough to avoid numerical problems. It is suggested that a minimum value of $\alpha \geq 50$ that results in a global stiffness loss less than 2%. Different guidelines have been proposed for selecting the stiffness of the interface for a carbon/epoxy composite [Turon et al., 2005].

Interfacial strength Alfano and Crisfield [Alfano and Crisfield, 2001] highlighted that the lowering of interfacial strength can improve the convergence rate of the solution. Harper and Hallett [Harper and Hallett, 2008] showed that excessively low interfacial strength would affect the global response of the structure. An explanation is that, with decreasing interfacial strength, the length of the process zone and the number of elements in the cohesive zone increase. A higher interfacial strength would result in a smaller process zone and hence a more brittle interfacial behavior. Therefore, the authors emphasize that the lowering of interfacial strength should be carefully done.

The interfacial normal and shear strengths (σ^e and τ^e) required for a needed num-

ber of elements (N_e) in the process zone [Song et al., 2008] can be expressed by:

$$\sigma^e = \sqrt{\frac{E_y G_{IIc}}{N_e l_e}} \quad \text{and} \quad \tau^e = \sqrt{\frac{E_y G_{Ic}}{N_e l_e}} \quad (3.36)$$

Therefore, the interfacial strengths are chosen as:

$$\bar{\sigma} = \min\{\sigma^e, \sigma_c\} \quad \text{and} \quad \bar{\tau} = \min\{\tau^e, \tau_c\} \quad (3.37)$$

The enlargement of the process zone, when the interfacial strength is reduced, is of significance in correctly capturing the distribution of tractions ahead of the crack tip.

3.5 Numerical implementation

This section is focused on PGD implementation of the cohesive zone model. It presents some computational aspects and details of the implementation.

3.5.1 Kinematics of the interface element

Two approaches are compared in this chapter: the PGD-CZM and the FEM-CZM. These two approaches use different interface elements. The cohesive surface of a laminate denoted Γ_{coh} is illustrated in Figure 3.15. In FEM, the cohesive surface is modeled using zero-thickness linear quadrilateral cohesive elements with four nodes. The zero-thickness linear one-dimensional (1D) cohesive element shown in Figure 3.15 is used to simulate delamination problems in conjunction with the PGD. The constitutive equations of these elements are mentioned in the previous sections in the case of single or mixed mode delamination.

The displacement discontinuity δ across the interface Γ_{coh} can be expressed in terms of the displacement vector \mathbf{u} computed on the two sides of the discontinuity (\mathbf{u}^+ for the upper side and \mathbf{u}^- for the lower side):

$$\delta = \mathbf{u}^+ - \mathbf{u}^- \Leftrightarrow \begin{pmatrix} \delta_{II} \\ \delta_I \end{pmatrix} = \begin{pmatrix} u^+ - u^- \\ w^+ - w^- \end{pmatrix} \quad (3.38)$$

In the case of the finite element approach, the number of cohesive elements is related to the number of nodes in the mid-plane surface and to the number of layers. In the PGD approach, the number of cohesive elements in the thickness is only equal to the number of interfaces between layers.

3.5.2 Mathematical formulation for cohesive problem with the PGD

This subsection focuses on the development of the PGD formulation in conjunction with a bilinear CZM in a two-dimensional (2D) domain $\Omega = \Omega_x \times \Omega_z$. The



Composite laminate

Interface

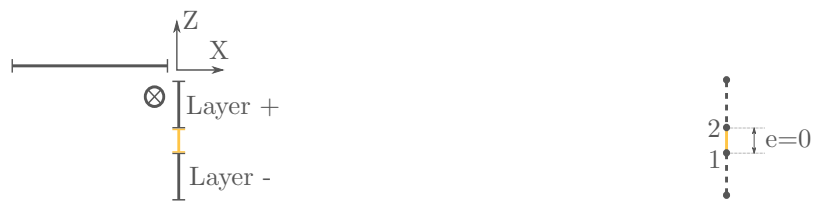
(a) Interface description



2D Finite element discretization

A linear 2D interface cohesive element

(b) FEM - CZM



1D/1D PGD discretization

A linear 1D interface cohesive element

(c) PGD - CZM

Figure 3.15 – Definition of cohesive surfaces.

boundary of Ω is noted Γ . For the sake of simplicity and without loss of generality, only two layers with the same thickness h are considered. There is then only one interface between layers, which is assumed being normal to the mid-plane surface as represented 3.15. Furthermore, the problem is treated in 2D using plane strain hypothesis. The weak form of the equilibrium equation for linear elastic materials with a cohesive surface Γ_{coh} and a cohesive stress vector \mathbf{T}_{coh} , without body force, gives:

$$\int \int_{\Omega} \varepsilon(\mathbf{u}^*) \cdot (\mathbb{H}\varepsilon(\mathbf{u})) d\Omega + \int_{\Gamma_{coh}} \mathbf{T}_{coh} \delta^* d\Gamma = \int_{\Gamma} \mathbf{T}_{ext} \mathbf{u}^* d\Gamma \quad (3.39)$$

Where \mathbf{u}^* and δ^* are the virtual displacement and virtual separation, respectively. ε is the strain tensor using the matrix form:

$$\varepsilon = \begin{pmatrix} \varepsilon_{xx} \\ \varepsilon_{zz} \\ 2\varepsilon_{xz} \end{pmatrix} \quad (3.40)$$

\mathbf{T}_{ext} is the external force on the boundary Γ . \mathbb{H} is a matrix related to the constitutive equation in each layer. For an orthotropic material with plane strain hypothesis, \mathbb{H} is defined by:

$$\mathbb{H}^{-1} = \begin{bmatrix} \frac{1}{E_x} & -\frac{\nu_{xz}}{E_x} & 0 \\ -\frac{\nu_{xz}}{E_x} & \frac{1}{E_z} & 0 \\ 0 & 0 & \frac{1}{G_{xz}} \end{bmatrix} \quad (3.41)$$

Where E_x , E_z , ν_{xz} and G_{xz} are the material parameters (elastic modulus, Poisson ratio, and shear modulus). The displacement field $\mathbf{u}(x, z)$ is approximated using the following separated form:

$$\mathbf{u} \approx \mathbf{u}^n(x, z) = \sum_{i=1}^n \mathbf{F}_i(x) \circ \mathbf{G}_i(z) \quad \forall (x, z) \in \Omega \quad (3.42)$$

$\mathbf{F}_i(x) = \begin{pmatrix} F_u^i(x) \\ F_w^i(x) \end{pmatrix}$ are functions of the in-plane coordinate.

$\mathbf{G}_i(z) = \begin{pmatrix} G_u^i(z) \\ G_w^i(z) \end{pmatrix}$ are functions involving the thickness coordinate.

\circ denotes the Hadamard product.

Eq. 3.42 is then equivalent to:

$$\mathbf{u}^n = \begin{pmatrix} u_n \\ w_n \end{pmatrix} = \begin{pmatrix} \sum_{i=1}^n F_u^i G_u^i \\ \sum_{i=1}^n F_w^i G_w^i \end{pmatrix} \quad (3.43)$$

Then, the separated representation of the strain tensor in Lagrangian description gives:

$$\varepsilon(\mathbf{u}^n(x, z)) = \sum_{i=1}^n \begin{pmatrix} F_{u,x}^i G_u^i \\ F_w^i G_{w,z}^i \\ F_u^i G_{u,z}^i + F_{w,x}^i G_w^i \end{pmatrix} \quad (3.44)$$

$f_{,x}$ denotes the derivative of a function f with respect to x . It is assumed that the first n modes have been determined at previous iterations. In order to enrich the separated approximation, some new functions $R_u(x)$, $S_u(x)$, $R_w(x)$ and $S_w(x)$ have to be determined. The new approximation is then:

$$\mathbf{u}^{n+1}(x, z) = \mathbf{u}^n(x, z) + \begin{pmatrix} R_u(x)S_u(z) \\ R_w(x)S_w(z) \end{pmatrix} \quad (3.45)$$

That can also be written as:

$$\begin{aligned} \mathbf{u}^{n+1}(x, z) &= \mathbf{u}^n(x, z) + \begin{pmatrix} R_u(x) \\ R_w(x) \end{pmatrix} \circ \begin{pmatrix} S_u(z) \\ S_w(z) \end{pmatrix} \\ &= \mathbf{u}^n(x, z) + \mathbf{R}(x) \circ \mathbf{S}(z) \end{aligned} \quad (3.46)$$

The strain derived from Eq. 3.46 is:

$$\varepsilon(\mathbf{u}^{n+1}(x, z)) = \varepsilon(\mathbf{u}^n(x, z)) + \varepsilon(\mathbf{R}(x) \circ \mathbf{S}(z)) \quad (3.47)$$

And test function \mathbf{u}^* is defined from the separated representation:

$$\begin{aligned} \mathbf{u}^*(x, z) &= \begin{pmatrix} R_u^*(x)S_u(z) + R_u(x)S_u^*(z) \\ R_w^*(x)S_w(z) + R_w(x)S_w^*(z) \end{pmatrix} \\ &= \mathbf{R}^*(x) \circ \mathbf{S}(z) + \mathbf{R}(x) \circ \mathbf{S}^*(z) \end{aligned} \quad (3.48)$$

The interlaminar normal stress σ_{zz} and shear stress τ_{xz} on the interface are computed from the relative displacement vector defined in Eq. 3.38 using the bilinear cohesive law.

$$\mathbf{T}_{coh} = \begin{pmatrix} \sigma_{zz} \\ \tau_{xz} \end{pmatrix} = \begin{pmatrix} \lambda_I K_I \delta_I \\ \lambda_{II} K_{II} \delta_{II} \end{pmatrix} \quad (3.49)$$

In pure modes, the values of λ_j with $j = I, II$ are computed from Eq. 3.27.

$$\lambda_j = \begin{cases} 1 & \delta_j < \delta_c^j \\ (1 - d_j) & \delta_c^j \leq \delta_j < \delta_m^j \\ 0 & \delta_j \geq \delta_m^j \end{cases}, \quad j = I, II \quad (3.50)$$

In mixed mode, the damage of the interface is described by $\lambda = \lambda_I = \lambda_{II}$.

λ is computed from the relations given by the cohesive law under mixed mode delamination. Introducing Eq. 3.46 and Eq. 3.49 into the weak form (Eq. 3.39) it results:

$$\begin{aligned} &\int \int_{\Omega} \varepsilon(\mathbf{u}^*) \cdot [\mathbb{H}\varepsilon(\mathbf{R} \circ \mathbf{S})] d\Omega \\ &+ \int_{\Gamma_{coh}} \lambda_I K_I (w_{n+1}^+ - w_{n+1}^-) (w_{n+1}^{+*} - w_{n+1}^{-*}) d\Gamma \\ &+ \int_{\Gamma_{coh}} \lambda_{II} K_{II} (u_{n+1}^+ - u_{n+1}^-) (u_{n+1}^{+*} - u_{n+1}^{-*}) d\Gamma \\ &= - \int \int_{\Omega} \varepsilon(\mathbf{u}^*) \cdot [\mathbb{H}(\mathbf{u}^n)] d\Omega + \int_{\Gamma} \mathbf{T}_{ext} \mathbf{u}^* d\Gamma \end{aligned} \quad (3.51)$$

The cohesive surface is normal to the thickness so that $\Gamma_{coh} \equiv \Omega_x$. The initial position of the two faces of the cohesive zone is defined by their coordinates on Ω_z denoted z^+ and z^- for all $x \in \Omega_x$. After discretization, z^+ and z^- define the coordinates of two nodes on Ω_z that may be initially at the same position.

$$\begin{cases} u_{n+1}^+ - u_{n+1}^- = R_u(x) (S_u(z^+) - S_u(z^-)) + \sum_{i=1}^n F_u^i(x) (G_u^i(z^+) - G_u^i(z^-)) \\ w_{n+1}^+ - w_{n+1}^- = R_w(x) (S_w(z^+) - S_w(z^-)) + \sum_{i=1}^n F_w^i(x) (G_w^i(z^+) - G_w^i(z^-)) \end{cases} \quad (3.52)$$

Finding the couple of functions (\mathbf{R}, \mathbf{S}) is a highly non-linear problem. For that purpose, an alternating directions strategy is used. It proceeds as follows: At each iteration, a single function \mathbf{R} and \mathbf{S} is computed alternately assuming the other is known. This procedure continues until convergence. So there are two steps:

1. finding \mathbf{R} assuming \mathbf{S}
2. finding \mathbf{S} assuming \mathbf{R}

At the beginning of the procedure, the functions \mathbf{R} and \mathbf{S} are initialized with some arbitrary functions. In practice, the initialization values have a weak impact on the convergence. Random functions coherent with boundary conditions are used in this work. Only the first step is described in the following because the second step is very similar. From now on, $\mathbf{R}(x)$ is assumed known and the solution of $\mathbf{S}(z)$ has to be determined. The test function then becomes:

$$\mathbf{u}^*(x, z) = \begin{pmatrix} R_u(x) S_u^*(z) \\ R_w(x) S_w^*(z) \end{pmatrix} = \mathbf{R}(x) \circ \mathbf{S}^*(z) \quad (3.53)$$

Implying the strain tensor,

$$\varepsilon(\mathbf{u}^{n*}(x, z)) = \varepsilon(\mathbf{R}(x) \circ \mathbf{S}^*(z)) = \sum_{i=1}^n \begin{pmatrix} R_{u,x} S_u^* \\ R_w S_{w,z}^* \\ R_u S_{u,z}^* + R_{w,x} S_w^* \end{pmatrix} \quad (3.54)$$

The weak form becomes:

$$\begin{aligned}
& \int \int_{\Omega} \varepsilon(\mathbf{R} \circ \mathbf{S}^*) \cdot [\mathbb{H}\varepsilon(\mathbf{R} \circ \mathbf{S})] d\Omega \\
& + \int_{\Gamma_{coh}} \lambda_I K_I \left[\left(\sum_{i=1}^n F_w^i(x) G_w^i(z^+) + R_w(x) S_w(z^+) \right) \right. \\
& \left. - \left(\sum_{i=1}^n F_w^i(x) G_w^i(z^-) + R_w(x) S_w(z^-) \right) \right] [R_w(x) S_w^*(z^+) - R_w(x) S_w^*(z^-)] d\Gamma \\
& + \int_{\Gamma_{coh}} \lambda_{II} K_{II} \left[\left(\sum_{i=1}^n F_u^i(x) G_u^i(z^+) + R_u(x) S_u(z^+) \right) \right. \\
& \left. - \left(\sum_{i=1}^n F_u^i(x) G_u^i(z^-) + R_u(x) S_u(z^-) \right) \right] [R_u(x) S_u^*(z^+) - R_u(x) S_u^*(z^-)] d\Gamma \\
& = - \int \int_{\Omega} \varepsilon(\mathbf{R} \circ \mathbf{S}^*) \cdot [\mathbb{H}\varepsilon(\mathbf{u}^n)] d\Omega + \int_{\Gamma} \mathbf{T}_{ext}(\mathbf{R} \circ \mathbf{S}^*) d\Gamma
\end{aligned} \tag{3.55}$$

The following coefficients are defined:

$$\left\{ \begin{array}{l} \alpha_j^k = \int_{\Gamma_{coh}} \lambda_j K_j R_k(x) \sum_{i=1}^n F_k^i(x) G_k^i(z^+) d\Gamma \\ \beta_j^k = \int_{\Gamma_{coh}} \lambda_j K_j (R_k(x))^2 d\Gamma \\ \gamma_j^k = \int_{\Gamma_{coh}} \lambda_j K_j R_k(x) \sum_{i=1}^n F_k^i(x) G_k^i(z^-) d\Gamma \end{array} \right. \quad j = (I, II); \quad k = (u, w) \tag{3.56}$$

These coefficients can be calculated numerically with $\Gamma_{coh} \equiv \Omega_x$. Using the previous notations, Eq. 3.55 becomes:

$$\begin{aligned}
& \int \int_{\Omega} \varepsilon(\mathbf{R} \circ \mathbf{S}^*) \cdot [\mathbb{H}\varepsilon(\mathbf{R} \circ \mathbf{S})] d\Omega \\
& + \alpha_I^w \cdot S_w^*(z^+) + \beta_I^w \cdot S_w^*(z^+) S_w(z^+) - \gamma_I^w \cdot S_w^*(z^+) - \beta_I^w \cdot S_w^*(z^+) S_w(z^-) \\
& - \alpha_I^w \cdot S_w^*(z^-) - \beta_I^w \cdot S_w^*(z^-) S_w(z^+) + \gamma_I^w \cdot S_w^*(z^-) + \beta_I^w \cdot S_w^*(z^-) S_w(z^-) \\
& + \alpha_{II}^u \cdot S_u^*(z^+) + \beta_{II}^u \cdot S_u^*(z^+) S_u(z^+) - \gamma_{II}^u \cdot S_u^*(z^+) - \beta_{II}^u \cdot S_u^*(z^+) S_u(z^-) \\
& - \alpha_{II}^u \cdot S_u^*(z^-) - \beta_{II}^u \cdot S_u^*(z^-) S_u(z^+) + \gamma_{II}^u \cdot S_u^*(z^-) + \beta_{II}^u \cdot S_u^*(z^-) S_u(z^-) \\
& = - \int \int_{\Omega} \varepsilon(\mathbf{R} \circ \mathbf{S}^*) \cdot [\mathbb{H}\varepsilon(\mathbf{u}^n)] d\Omega + \int_{\Gamma} \mathbf{T}_{ext}(\mathbf{R} \circ \mathbf{S}^*) d\Gamma
\end{aligned} \tag{3.57}$$

At this point, a classical PGD solver can be used.

The terms $\int \int_{\Omega} \varepsilon(\mathbf{R} \circ \mathbf{S}^*) \cdot [\mathbb{H}\varepsilon(\mathbf{R} \circ \mathbf{S})] d\Omega$ and $\int \int_{\Omega} \varepsilon(\mathbf{R} \circ \mathbf{S}^*) \cdot [\mathbb{H}\varepsilon(\mathbf{u}^n)] d\Omega$ can be developed as a sum of simple integrals using the expression of ε and \mathbb{H} . These

integrals on Ω can be separated as a product of integrals on Ω_x and on Ω_z . The integrals on Ω_x can be calculated numerically because all functions defined on Ω_x are known. It remains a problem on Ω_z that can be solved using the finite element method.

3.6 Numerical simulations

Three fracture mechanic tests were selected to validate the proposed modeling for 2D fracture problems. Each test is related to a particular mode of propagation of the crack. The first test carried out was the DCB test, in which the delamination happens mainly in mode I. The second was the ELS test, related to the failure in mode II. The last one was the MMELS test for mixed mode damage.

Results of numerical simulations performed using the PGD are compared with results of classical FEM implementation with the same set of parameters. The aims are to validate the PGD approach and to evaluate its response with respect to damage formulations and cohesive zone key parameters. In the two cases, a static simulation is performed. In the FEM, a fixed point algorithm is used to treat the non-linearity related to the behavior of the cohesive law (Eq. 3.49).

The PGD is by nature a non-linear solver. The linearization of the operators required can be performed at each iteration of the PGD. There are many ways to do this. The following strategy is chosen:

1. The operators related to the cohesive zones are linearized using a fixed value of λ ($\lambda = 1$ at the first iteration).
2. A new term of the PGD expansion defined in Eq. 3.42 is computed with the linearized operators.
3. The partial PGD solution is used to determine the values of the displacement discontinuity δ along the cohesive zone. Then, the cohesive law gives new values for λ .
4. The PGD residual error is computed. If the convergence is not reached, return to 1.

Material and cohesive properties

The specimen geometries used in this work are shown in Figure 3.16. The properties of the material (a unidirectional carbon/epoxy composite) and the ones of the cohesive interface are listed in Table 3.4. The upper and lower layers (unidirectional layers) of the specimen are modeled with a transverse isotropic constitutive law. The element size for the solid and the cohesive elements is the same for

all models and is equal 0.2mm . The interface element stiffnesses (K_I and K_{II})

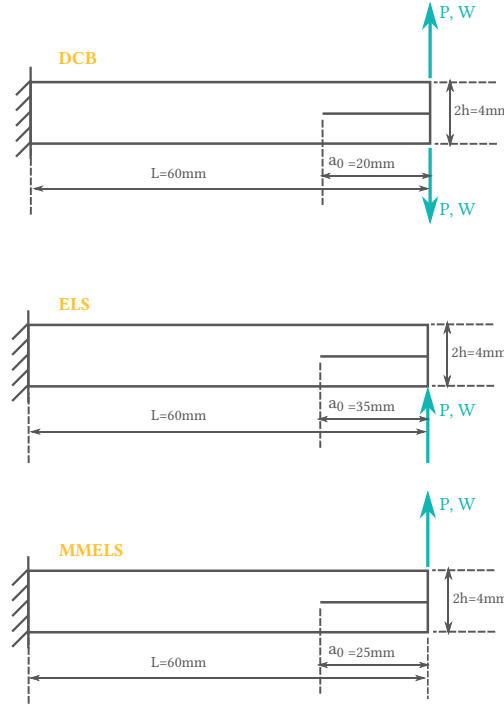


Figure 3.16 – Specimen dimensions.

are chosen to obtain a good compromise between convergence calculation, computation time, and elastic properties of the laminate [Turon et al., 2005]. The computational cost strongly depends on the initial stiffness values. As a matter of fact, the CPU time increases when K_I and K_{II} are raised. For a high value of the failure stresses (σ_c and τ_c), convergence problems may occur. Those problems are due to a significant drop in the slope of the interface stiffness after the failure stresses are reached. As τ_c has a large influence on the interface behavior, we chose to link it to σ_c according to the following dependence, already noted in [Turon et al., 2010]:

$$\tau_c = \sigma_c \sqrt{\frac{G_{IIc}}{G_{Ic}}} \quad (3.58)$$

The $\frac{\delta_c^i}{\delta_m^i}$ ratio ($i = I, II$) is also an important factor to validate the Crisfield law [Vandellos et al., 2009]. We found that, for certain values of this ratio, the critical energy release rate required to propagate the crack was less than imposed in our calculation. This observation was already made by Vandellos et al. [Vandellos et al., 2009] who varied the $\frac{\delta_c^i}{\delta_m^i}$ ratio in order to obtain the correct rate. We applied the same method, which enabled us to assume a consistent value for G_{Ic} and G_{IIc} . It is those values that are presented in Table 3.4.

Material properties		Interfacial properties			
$E_z(MPa)$	11873	$G_{Ic}(N/mm)$	0.3 ;	$G_{IIc}(N/mm)$	1.6
$E_x(MPa)$	157380	$\sigma_c(MPa)$	60 ;	$\tau_c(MPa)$	139
$G_{xz}(MPa)$	5051	$K_I(N/mm^3)$	1.10^4 ;	$K_{II}(N/mm^3)$	5.10^4
ν_{xz}	0.31				

Table 3.4 – Material properties for carbon/epoxy.

Definition of mixed boundary conditions with the PGD

PGD does not enable direct introduction of mixed boundary conditions as required in the MMELS test. Although several methods have been proposed to incorporate such boundary conditions like penalization method and Lagrangian method [Ammar et al., 2012]. In our case, these two methods lead to convergence problems. Therefore, a third method more efficient was designed in this work. It consists in the addition of some elements that are located at the place where the mixed boundary conditions are imposed. Figure 3.17 represents the introduction of such virtual elements.

The added elements that undergo imposed displacement (the ones situated in the upper part of the specimen) are defined with an elastic modulus E_a equal to E_x or higher. The other elements corresponding to a free surface (situated in the lower part of the specimen) are defined with an elastic modulus E_b equal to zero. In that way, a uniform displacement can be enforced on the right side. The load is transmitted only on the elements situated in the upper part. There is no numerical difficulties with $E_b \approx 0$ because the problem is solved in the context of the PGD. Only 1D problems are treated in practice with no numerical error.

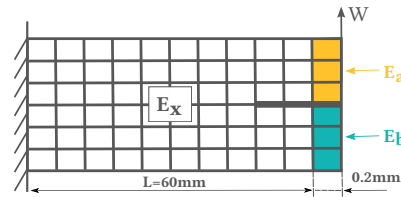


Figure 3.17 – Implementation of mixed boundary conditions in PGD. E_x is the longitudinal elastic modulus, the new elements (in colors) are incorporated at the surface where mixed boundary conditions are imposed.

3.6.1 Tests results

The solution obtained with the PGD gives the functions \mathbf{F}_i and \mathbf{G}_i from which the displacement field is built (using Eq. 3.42). These functions are depicted for the DCB test in Figure 3.18. In all the test cases, the global force–displacement

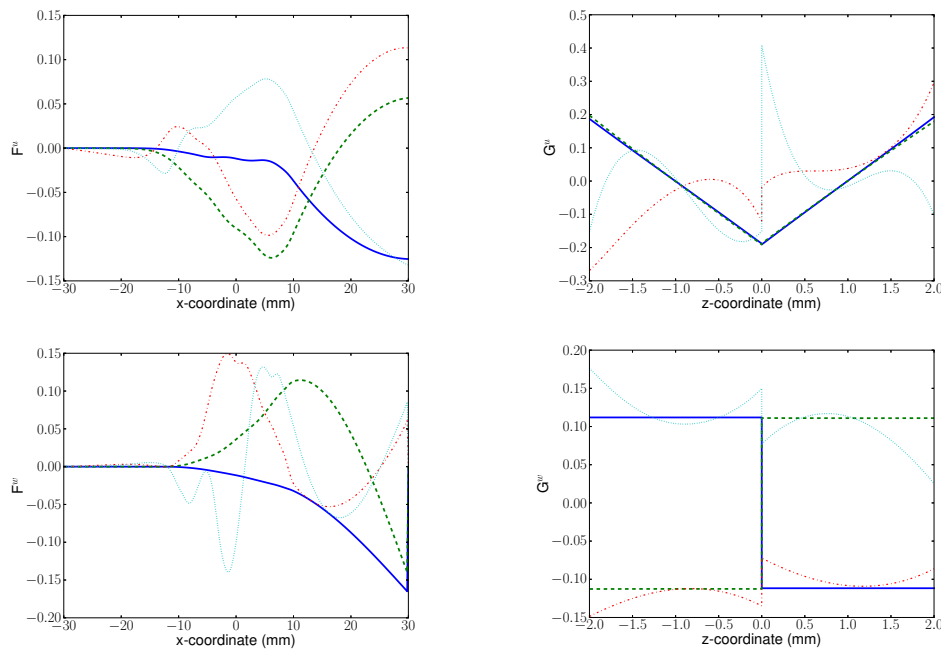


Figure 3.18 – Functions \mathbf{F}_i and \mathbf{G}_i in the separated representation of the displacement field.

curves are shown in Figure 3.19. These curves can be divided in two parts: (i) linear elastic response before damage is initiated and (ii) crack propagation. In the linear part, when the opening displacement increases, the load increases as well. On the contrary, the load decreases during the crack propagation. A slight nonlinear behavior may be observed before the maximum load point, especially in the MMELS test. A very good agreement is observed between PGD and finite element simulations. The analytical model is based on beam theory and underestimates the compliance and the strain energy release rate.

For these simulations, Figure 3.20 shows the damage variable along the crack path for an imposed displacement. The process zone was defined as the zone in which the damage variable is strictly between 0 and 1, as shown in Figure 3.21. The length of the process zone is given in Table 3.5, for a common mesh size of 0.2mm . In these simulations, it is mandatory to obtain a number of element in the process zone, which is larger than a critical number (three or five elements according to Turon et al. [Turon et al., 2005]). In our simulations, we found sufficient number of elements in the process zone, as mentioned in Table 3.5.

The evolution of the local interface separations along the crack path for each test cases are shown in Figure 3.22. The relative separation decreased from the edge on which the displacement is applied, and tends toward zero in the undamaged zone

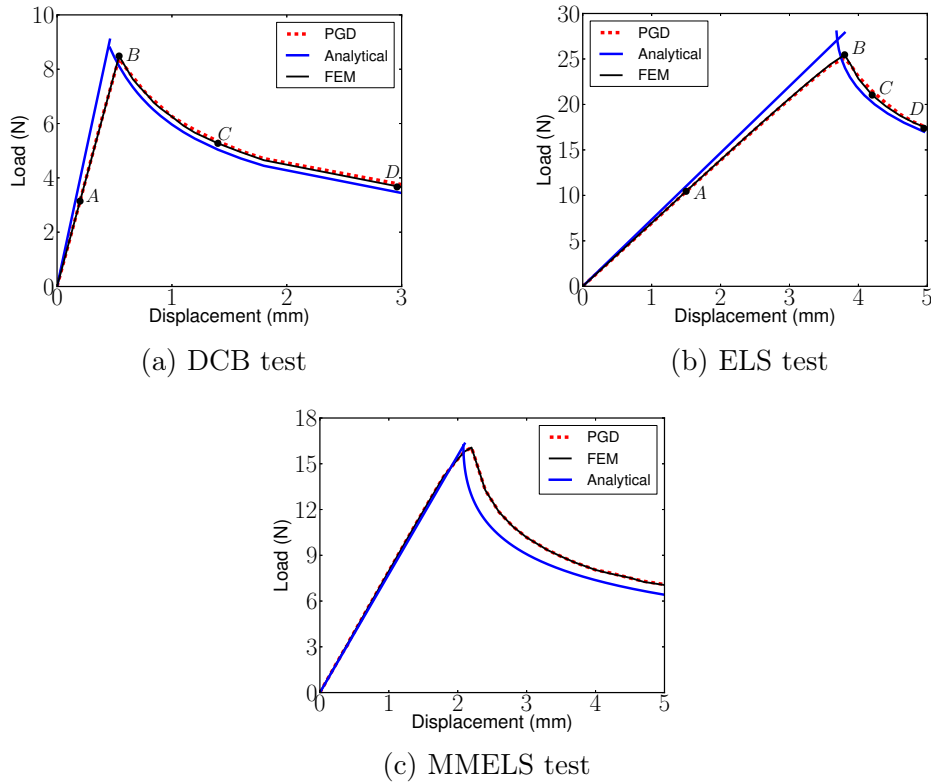


Figure 3.19 – Force vs. displacement curves.

	DCB test	ELS test	MMELS test
Length (mm)	4.6	2.2	1.8
Number of Elements	23	11	9

Table 3.5 – Quantification of the simulated process zone length using PGD method.

after the process zone. This figure shows that for an imposed displacement equal to 1.5, 5, and 4mm in the case of DCB, ELS, and MMELS tests, respectively, the pre-existing crack was propagated by 22, 20.2 and 26.8mm. In all cases, a good accordance between the PGD and FEM is obtained at the interface. The σ_{xx} and σ_{zz} stress distributions are plotted for the three fracture tests in Figures 3.23, 3.24 and 3.25. The PGD approach and the classical FEM approach give here again very similar results. The mean relative errors of the stress between the PGD and the FEM for each tests are mentioned in Table 3.6. A tension zone and a compressive zone are observed near the crack tip in the stress distributions of the DCB test. The compression is generated by the bending moment applied by the upper and lower beams of the specimen [Tàvara et al., 2013]. Four stages were isolated in Figure 3.19: (i) **A** the elastic region, (ii) **B** damage initiation, (iii) **C** crack growth, and (iv) **D** advanced growth of the crack. The cohesive stresses at

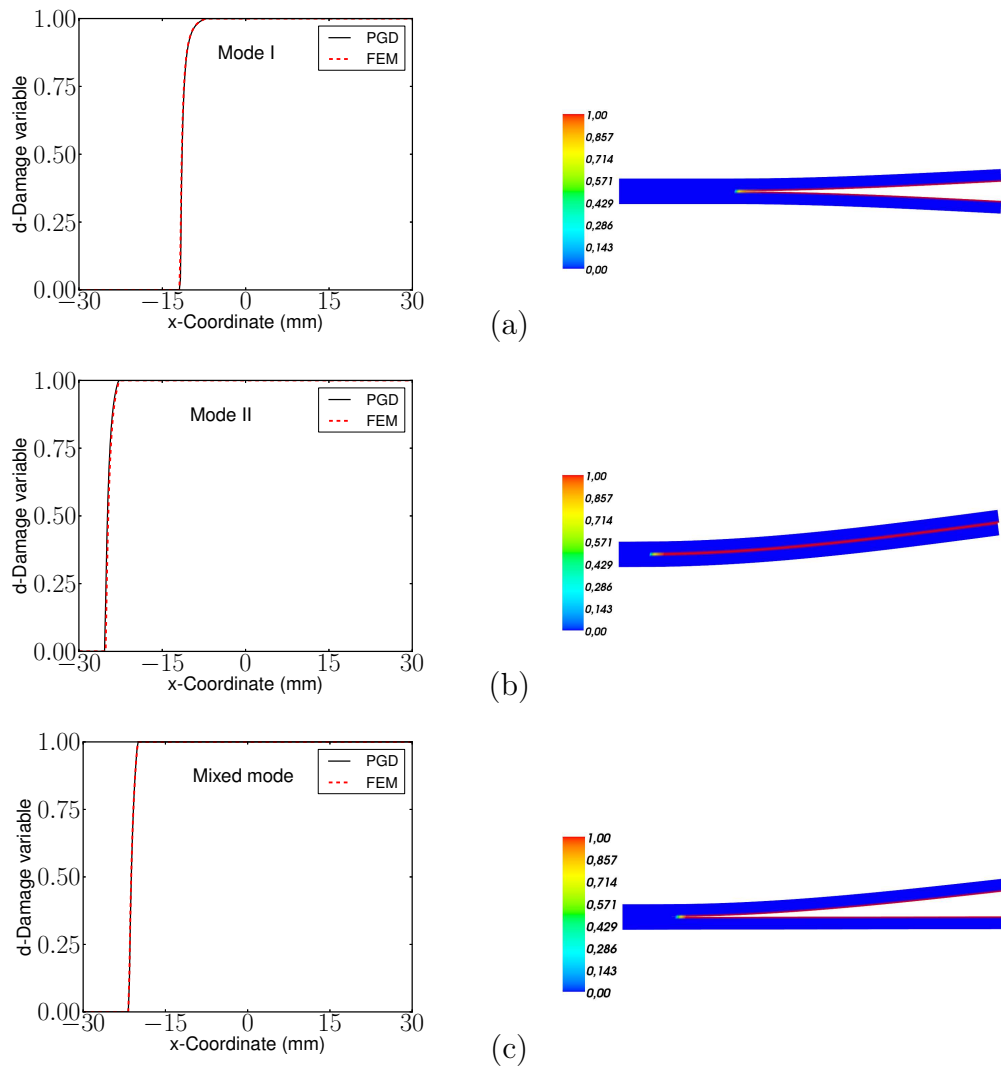


Figure 3.20 – Damage variable evolution along the crack path for an imposed displacement: (a) DCB test, (b) ELS test and (c) MMELS test.

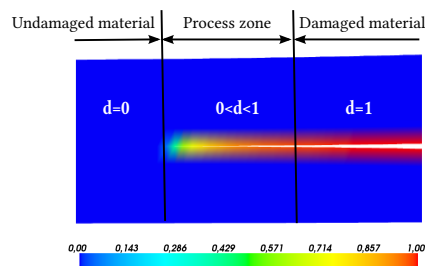


Figure 3.21 – Crack tip in the case of DCB test.

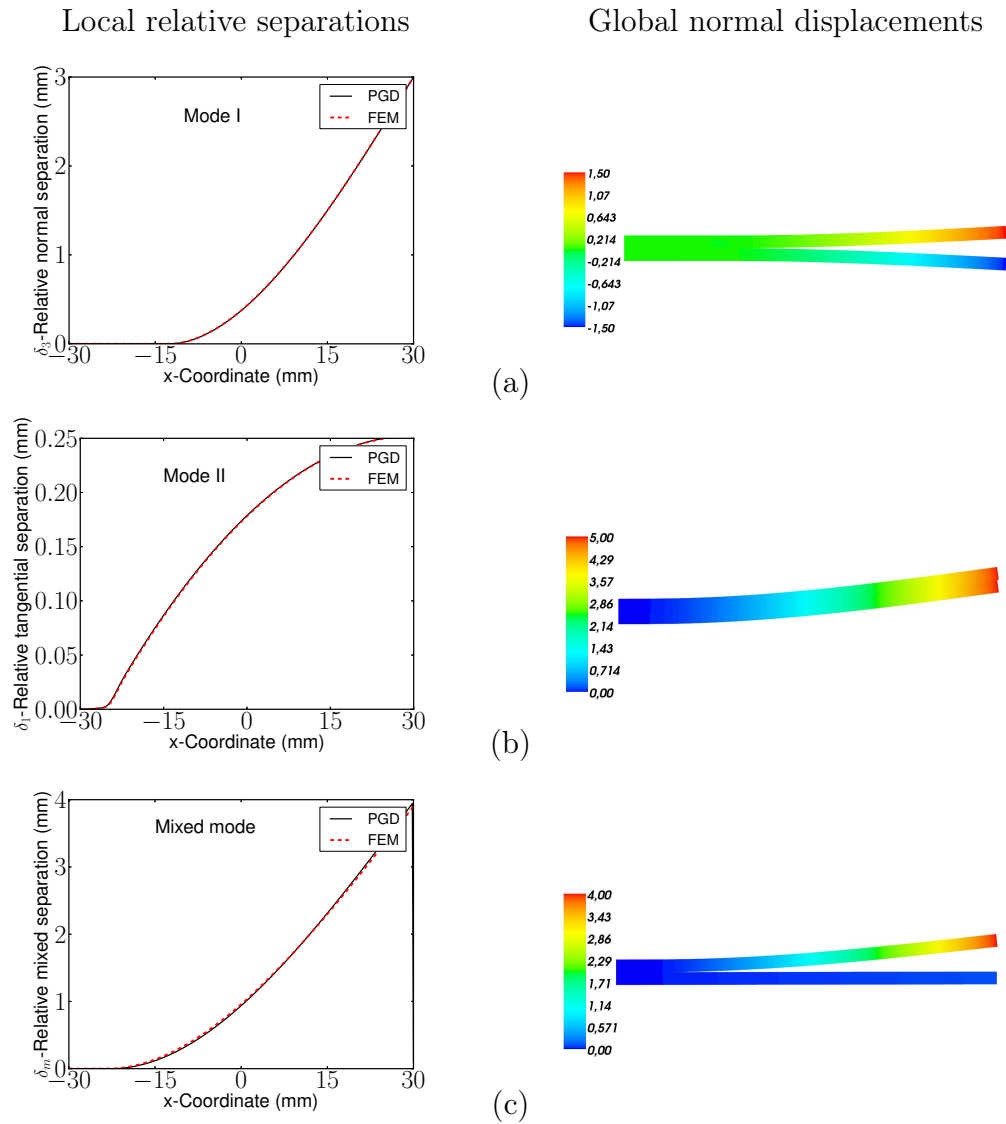


Figure 3.22 – Interface separations evolution along the crack path: (a) DCB test, (b) ELS test and (c) MMELS test.

Mean relative errors (%)	DCB test	ELS test	MMELS test
σ_{xx} stresses	0.3	0.2	0.3
σ_{zz} stresses	1.6	-	2
σ_{xz} stresses	-	3	3

Table 3.6 – Mean relative error.

the different stages are depicted in Figures 3.26 and 3.27 for the DCB and ELS test. In the DCB test, the tension and compressive zones mentioned above are present at all stages. The cohesive stress behind the crack tip (tensile stress) fol-

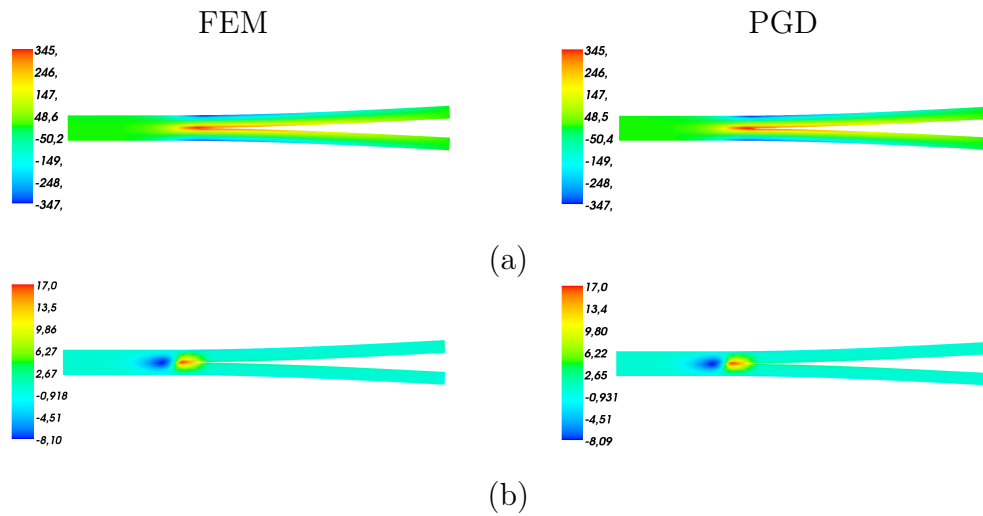


Figure 3.23 – The normal stress distributions in the longitudinal and thickness direction for the DCB specimen: (a) Stress σ_{xx} , (b) Stress σ_{zz} .

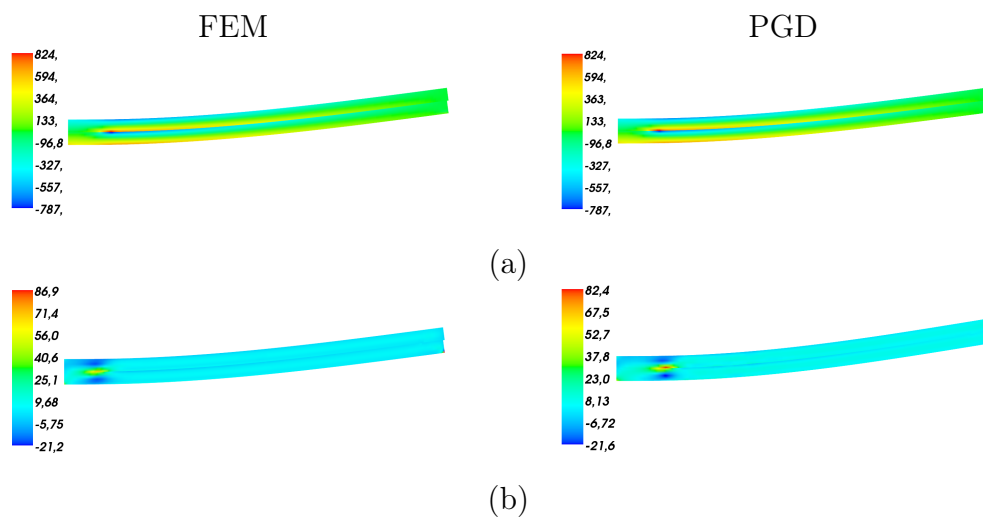


Figure 3.24 – The distribution of normal and shear stresses for the ELS specimen: (a) Stress σ_{xx} , (b) Stress σ_{xz} .

lows the evolution of Figure 3.19 (case of DCB test). The compressive stresses increase continuously when the load increase. In 2D the computational time using the PGD was decreased by a factor of 4 in comparison with the finite element simulation with very similar results.

3.6.2 3D simulation of a DCB test using the PGD

The main advantage of the PGD approach in comparison with the FEM approach is the reduction of the computational time. Previous 2D simulations showed that

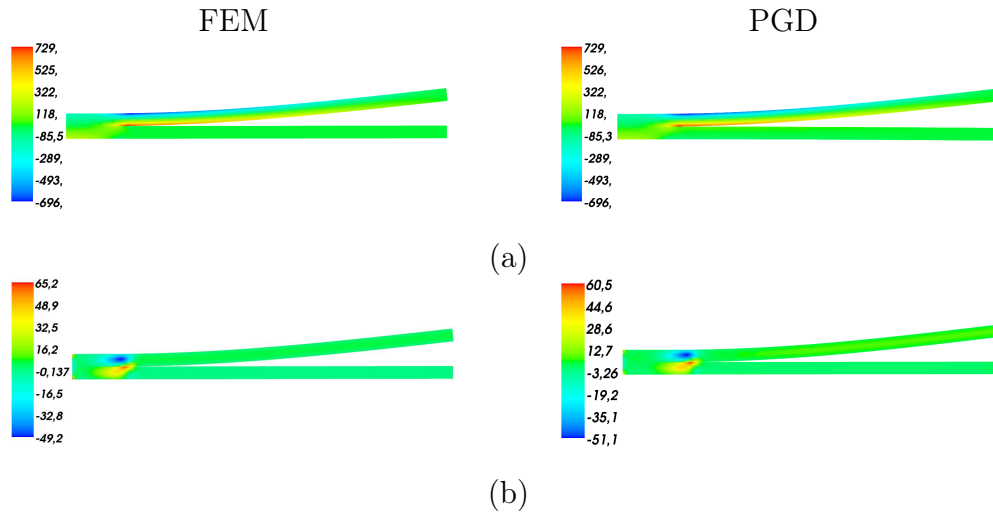


Figure 3.25 – The distribution of normal and shear stresses for the MMELS specimen: (a) Stress σ_{xx} , (b) Stress σ_{zz} and (c) Stress σ_{xz} .

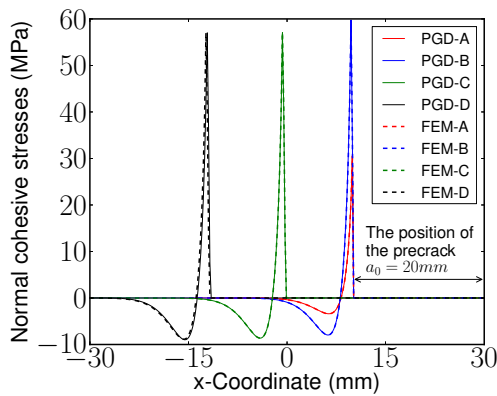


Figure 3.26 – Normal cohesive stresses vs. position for different load stages of DCB test.

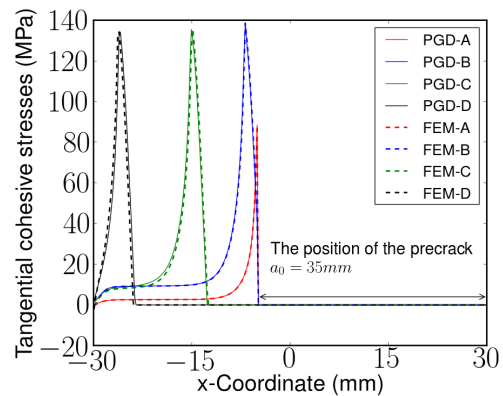


Figure 3.27 – Tangential cohesive stresses vs. position for different load stages of ELS test.

PGD is about four times faster than FEM, and the agreement between FEM and PGD is very good. Another asset is the easy insertion of the cohesive elements. In FEM-CZM, a whole mesh refinement is required when inserting cohesive elements. Whereas in PGD-CZM the cohesive elements are only required in the subspace corresponding to the z axis. A 3D DCB test case is realized to focus on the efficiency of PGD when increasing the number of nodes in the mesh. To do that, the same specimen geometry as shown in Figure 3.16 is used, together with the same precrack length as in the one shown in previous 2D DCB test. The specimen width is equal to 20mm . The properties of the material are described in Table 5.1. The 3D mesh is separated into 2D and 1D meshes as represented in Figure 3.28.

In this case, the displacement field denoted $u(x, y, z)$ is approximated using the separated form:

$$\mathbf{u} \approx \mathbf{u}^n(x, y, z) = \sum_{i=1}^n \mathbf{F}_i(x, y) \circ \mathbf{G}_i(z) \quad \forall (x, y, z) \in \Omega \quad (3.59)$$

where $\mathbf{F}_i(x, y) = \begin{pmatrix} F_u^i(x, y) \\ F_v^i(x, y) \\ F_w^i(x, y) \end{pmatrix}$ are functions of the mid-plane coordinate, and $\mathbf{G}_i(z) = \begin{pmatrix} G_u^i(z) \\ G_v^i(z) \\ G_w^i(z) \end{pmatrix}$ are functions involving the thickness coordinate.

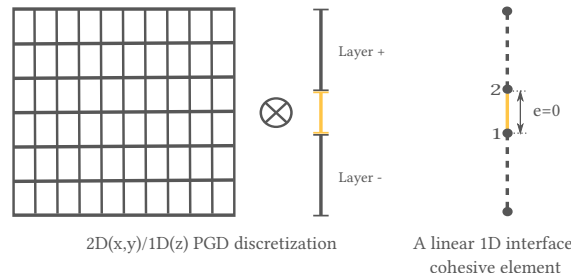


Figure 3.28 – 2D/1D PGD discretization.

After solving the problem, the functions F_w^i and G_w^i for $i = [1, 2]$ are depicted in Figure 3.29. The deformed shape and the longitudinal stress distribution (σ_{xx}) for

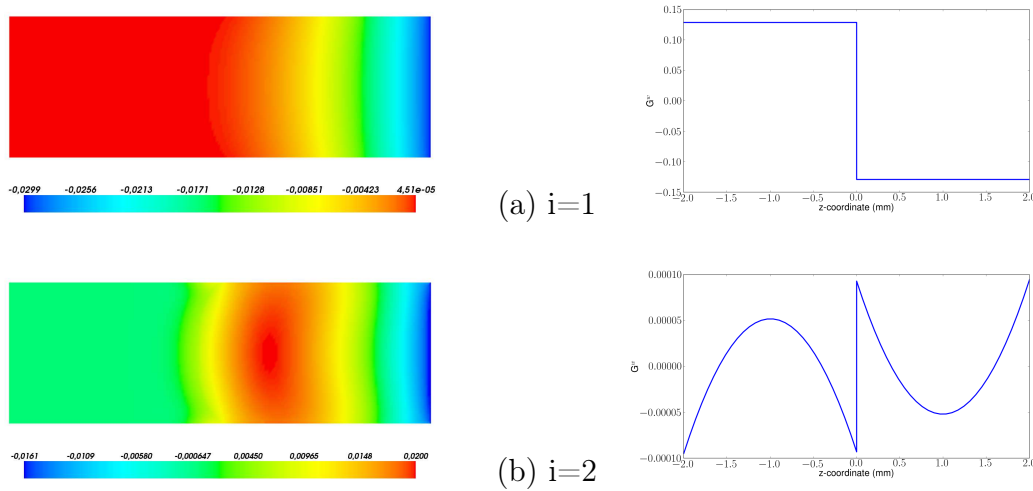


Figure 3.29 – Functions F_w^i and G_w^i in the separated representation of the displacement field: (a) $i=1$, (b) $i=2$.

an imposed displacement equal to $8mm$ are shown in Figure 3.30. The cohesive surface at several iterations is shown in Figure 3.31. In this figure, blue indicates

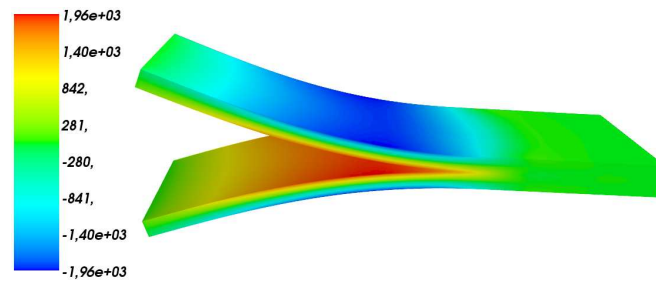


Figure 3.30 – The σ_{xx} stress distribution for the 3D DCB specimen.

the undamaged zone, red indicates the damaged zone, and the process zone is the small part between them. The initial precrack front shape is straight. It is possible to see that the crack initiates at the center of the specimen width. As the crack propagates, the crack front shape becomes slightly convex.

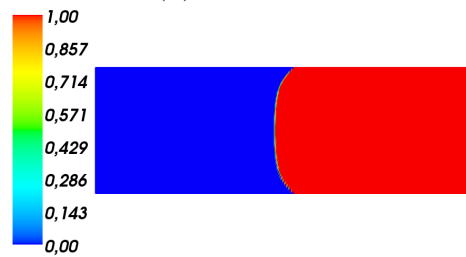
This simulation was performed with 20000 nodes in the $2D$ mesh and with 30 nodes in the $1D$ mesh (thickness). In $3D$, that represents a total of 1.8×10^6 degrees of freedom. The PGD algorithm enabled running the simulation on a simple laptop in less than 15 min. This represents an enormous gain of time when compared with classical $3D$ FEM simulations with comparable mesh refinement. With our code, the full $3D$ simulation can't be achieved on our laptop.



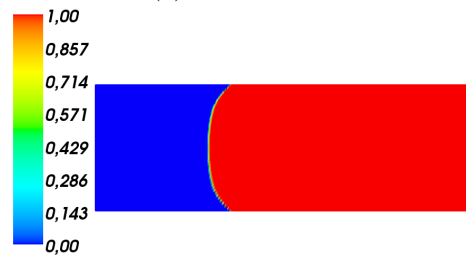
(a) iteration 3



(b) iteration 5



(c) iteration 40



(d) final iteration

Figure 3.31 – Crack surfaces of 3D DCB test: (a) iteration 3, (b) iteration 5, (c) iteration 40 and (d) final iteration.

Chapter **4**

Delamination in composite laminates under dynamic loading

“ Science, my lad, is made up of mistakes, but they are mistakes which it is useful to make, because they lead little by little to the truth. ”

Jules Verne

Contents

4.1	Why composites are vulnerable to impact damage ?	64
4.2	Low and high velocity impact	65
4.3	Failure mechanisms in low velocity impact	65
4.4	Types of impact response	68
4.5	Problem statement	69
4.5.1	Governing equation of motion	69
4.5.2	Time integration	70
4.5.3	Calculation of the contact force	71
4.5.4	Geometrical modelling and Boundary conditions	73
4.5.5	Numerical simulations	73

The method described in the previous chapter has proved its efficiency to simulate delamination evolution under quasi-static loading, especially in the case of standard fracture tests. In the present chapter, this strategy will be enhanced to simulate the low-velocity impact response of laminated composites.

The ever growing demand for lighter structures resulted in the increasing replacement of metallic materials by composite materials. While composite materials offer a number of superior design characteristics, composite structures are much more susceptible to impact damage than similar metallic structures. Impact can result in numerous damage mechanisms, ranging from barely visible impact damage (BVID) to complete penetration, which nevertheless severely reduces the stiffness and the residual strength of the composite structures. Impacts caused by foreign objects may arise during the life span of a structure including manufacturing, service, and maintenance operations. In the present work only low velocity impact events will be considered.

4.1 Why composites are vulnerable to impact damage ?

Damage in composites are different from those in metals because composite failure is a progressive accumulation of damages. Impact damages in metallic structures appears on the impacted surface, which makes them easy to detect. Due to the ductile nature of the metallic material, large amounts of energy may be absorbed, making it much less susceptible to impact damage. In contrast, impact damage in composites is often undetected or underestimated by visual inspection, beginning on the non-impacted surface or in the form of an internal hidden damage. Owing to the brittle nature of most composite materials, energy is absorbed in elastic deformation and through damage creation/propagation [Richardson and Wisheart, 1996], and not via plastic deformation.

The majority of impacts on composite plates occurs in the transverse direction. In addition, lack of through-thickness reinforcement leads to a low delamination resistance and poor impact damage tolerance. Even when the impact event creates non-visible damage in the material, its effect on the mechanical properties of the composite has to be taken into account. The resulting damage modes are a function of the type of loading, the stacking sequence, the properties of the impacting object and of the structure, and the boundary conditions.

4.2 Low and high velocity impact

Generally, impacts are classified into two main categories: (a) low velocity impact and (b) high velocity impact. Both categories produce different types of damages in the composite structure. Low velocity impact may be caused by accidentally dropped tools on the structure during manufacturing, service, or maintenance. High velocity impact may include situations such as a ballistic impact, bird strike, hail or foreign object debris (FOD). There are a number of different definitions by various researchers to distinguish a low velocity impact from a high velocity impact, but there is no universal agreement.

According to Sjöblom et al. [Sjöblom et al., 1988] and Shivakumar et al. [Shivakumar et al., 1985], low velocity impact is associated with an impact event which can be treated as quasi-static. The upper velocity limit of the impactor can vary from 1 to 10 m/s depending on the target stiffness, material properties and the impactor's mass and stiffness. Cantwell and Morton [Cantwell and Morton, 1991] classify low velocity impact as up to 10 m/s. However, Abrate [Abrate, 1991] suggested that low velocity impacts could occur at speeds less than 100 m/s. Liu and Malvern [Liu and Malvern, 1987] and Joshi and Sun [Joshi and Sun, 1987b] stated that the type of impact can be classed according to the damage incurred.

Low velocity impact damages are initiated by matrix cracks which induce delaminations at interfaces between plies of different orientations. These failure mechanisms dissipate the majority of the energy. In contrast, high velocity impact leads to very localized damage. High velocity impact is characterized by penetration induced fiber breakage. It should be noted that the energy level of the impacts can be separated into two types: low energy (low velocity/low mass) and high energy (low velocity/high mass, high velocity/low mass or high velocity/high mass).

4.3 Failure mechanisms in low velocity impact

Low velocity impact damage in composites is especially insidious due to the invisible damages (BVID) they cause. These damages can drastically decrease the residual strength of composite structure. It has been shown that, for unidirectional (UD) laminates under low velocity impact, significant amount of permanent damage in the form of matrix cracking, delaminations and fiber breakage may be present without being detectable by visual inspection. The failure mechanisms generally occur in the listed order with increasing impact energy. Matrix cracking has been widely reported as the first type of failure induced by transverse low velocity impact [Choi et al., 1991a; Choi et al., 1991b; Joshi and Sun, 1987a]. It acts as a starting point for the propagation of delamination. Figure 4.1 shows the typical matrix cracking and delamination damage found in an impacted com-

posite specimen. Matrix cracks appear parallel to the fibers due to tension or shear.

The initiation and propagation of matrix cracks are strongly dependent on the stacking sequence [Poon and N. Bellinger, 1993; Majeed, 1995; Fuoss, 1996]. Two types of matrix cracking can be observed: tensile matrix cracks and shear matrix cracks. Tensile matrix cracks are formed by the flexural deformations due to the tensile bending stresses. These cracks are generally located at the lower plies. Shear matrix cracks form in the upper plies directly under the impact zone and are induced by the high transverse shear stress through the material, and are inclined at approximately 45° . The matrix cracks first appear in the lowest ply [Lin and Lee, 1990]. Due to the coupling between delamination and matrix cracking, the initiation of delamination will occur at the locations of the initial matrix cracks.

Delamination is often considered to be the most energy consuming damage mechanism during the impact event. The majority of the energy absorbed in the laminate during impact dissipates into delamination propagation. Delaminations always occur at the interfaces between plies with different fiber orientations and tend to initiate at the bottom interface and progressively becomes smaller towards the impact face. The shape of the delaminated area changes with the orientation of plies and is generally a peanut with its major axis oriented in the fiber direction of the lowermost layer at the interface, as depicted in Figure 4.2. The peanut shape is a result of the shear stress distribution around the impactor, the interlamina shear strength along the fiber direction and the matrix cracking. Most of the available literature on impact behavior of composite laminates refer to impact damage in terms of its delamination size. The delamination length is defined as the size of the delaminated area along the fiber direction of the the lowermost layer. The delamination width is defined as the size of the delamination along a direction normal to the fiber direction. Fiber failure mostly appears after matrix cracking and delamination. This failure mode may occur at the zone under the impactor due to locally high stresses and indentation effects.

The type of damage resulting from impact on composites depends on the energy level of the impact [Majeed, 1995]:

- At low impact energie, minor damage in the form of a small plastic indentation is formed on the impact surface;
- At low to moderate impact energie, damage is initiated by matrix cracks in the lowest ply of the laminate as previously described. It creates delaminations at interfaces between plies with different fiber orientations. Damage propagates upward through the laminate to give the conical shape;
- At higher impact energies, fiber breakage and matrix cracking occurs on the back face of the laminate. Fiber microbuckling may occur on the impacted

face near the contact zone. As the impact energy increases, a complete penetration of the specimen occurs.

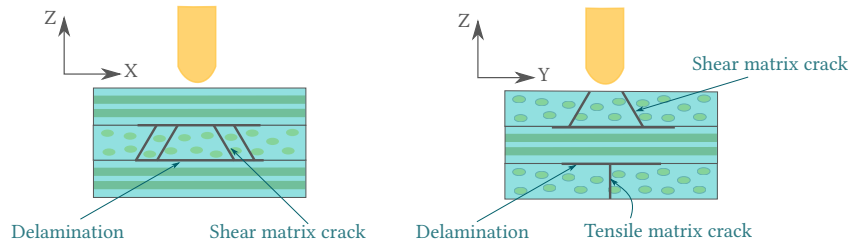


Figure 4.1 – Typical matrix cracking and delamination damage in a [0/90/0] UD laminated composite (longitudinal and transverse views).

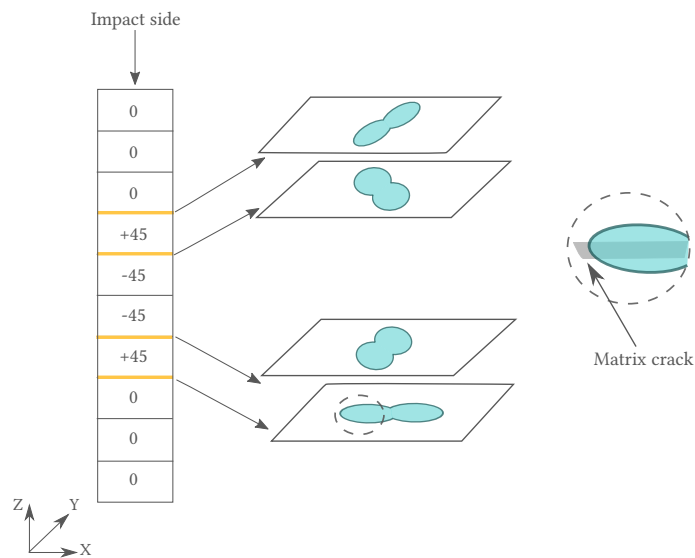


Figure 4.2 – Shape of the delamination.

The shape of impact damage through the section of the specimen appears to be approximately conical (Figure 4.3). The problem of impact damage analysis may

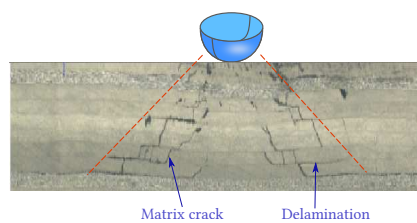


Figure 4.3 – Conical shape of impact damage.

be divided into two sub-problems [Olsson, 1999]:

- Impact damage resistance, which deals with the response and damage caused by an impact;
- Impact damage tolerance, which deals with the reduced strength and stability of the structure due to the presence of damage.

4.4 Types of impact response

In literature one can find that the impact response of a composite plate is different between the case of large mass impact and small mass impact [Abrate, 1994; Abrate, 2001; Olsson, 2001; Olsson, 2003]. Olsson [Olsson, 2001; Olsson et al., 2006] has demonstrated that the mass ratio between the impactor and the plate has a significant influence on the impact response (Figure 4.4). For small mass impactors (high velocity impact), the response is dominated by the flexural waves propagation and the impact time is short. The load and deflection are out of phase and independent on boundary conditions and plate size [Olsson, 2003]. Whereas, large mass impactors (low velocity impacts) with the same impact energy involves long contact time between impactor and target, and produces deformation of the entire structure with internal damage at points far from the contact region. Low velocity impact response is equivalent to a quasi-static response and the plate essentially deforms in the same way as under static loading.

As indicated by Troussset [Troussset, 2013], during finite element simulation of low velocity impact, about 90% of the total computation time is spent in the contact algorithm, regardless of the complexity of the composite plies behavior. For these reasons, low velocity impact tests are often simulated by simple static indentation tests, neglecting the influence of dynamic effects on the structural response. To avoid contact management during the impact simulation, the Hertzian contact law is commonly employed to deal with the contact between the impactor and the laminate. Various researchers have developed finite element models in conjunction

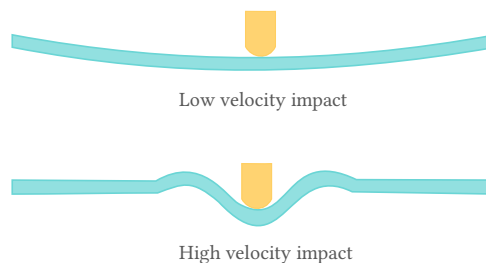


Figure 4.4 – Response types during impact on plates.

with the Hertzian contact law to study the impact response of laminated composite plates. Some important works on this subject can be found in references [Tan and Sun, 1985; Yigit and Christoforou, 1995; Yigit and Christoforou, 1998; Roy and Chakraborty, 2008; Choi and Lim, 2004; Li et al., 2014].

4.5 Problem statement

4.5.1 Governing equation of motion

According to principle of virtual work, and by assembling all mass and stiffness matrices with respect to the global coordinates, the discretized motion equations of the laminate by neglecting the damping take the following form:

$$[\mathbf{M}]\{\ddot{u}\} + [\mathbf{K}]\{u\} = \{F\} \quad (4.1)$$

Here $[\mathbf{M}]$ and $[\mathbf{K}]$ are the mass and stiffness matrices of the composite laminate, $\{\ddot{u}\}$ and $\{u\}$ are respectively the nodal displacement and acceleration vectors.

In order to develop the PGD formulation, the displacement field denoted as $u(x, y, z)$ is approximated using the separated form:

$$\mathbf{u} \approx \mathbf{u}^n(x, y, z) = \begin{pmatrix} u_n(x, y, z) \\ v_n(x, y, z) \\ w_n(x, y, z) \end{pmatrix} = \sum_{i=1}^n \mathbf{F}_i(x, y) \circ \mathbf{G}_i(z) \quad \forall (x, y, z) \in \Omega \quad (4.2)$$

where $\mathbf{F}_i(x, y) = \begin{pmatrix} F_u^i(x, y) \\ F_v^i(x, y) \\ F_w^i(x, y) \end{pmatrix}$ are functions of the mid-plane coordinate,

and $\mathbf{G}_i(z) = \begin{pmatrix} G_u^i(z) \\ G_v^i(z) \\ G_w^i(z) \end{pmatrix}$ are functions involving the thickness coordinate.

The acceleration and velocity vectors are also approximated using the separated form:

$$\ddot{\mathbf{u}}(x, y, z) = \sum_{i=1}^n \ddot{\mathbf{F}}_i(x, y) \circ \ddot{\mathbf{G}}_i(z) \quad (4.3)$$

$$\dot{\mathbf{u}}(x, y, z) = \sum_{i=1}^n \dot{\mathbf{F}}_i(x, y) \circ \dot{\mathbf{G}}_i(z) \quad (4.4)$$

$\{F\}$ is the external force vector which includes the contact force (impact force) between impactor and the plate. Under low velocity impact, $\{F\}$ is given by:

$$\{F\} = \{0 \ 0 \ 0 \ \dots \ F_c \ \dots \ 0 \ 0 \ 0\}^T \quad (4.5)$$

where F_c is the contact force. The magnitude of contact force is not known a priori and needs to be calculated using a contact law. We note that $\{F\}$ depends on the displacements and time.

4.5.2 Time integration

There are many methods to increment the solution of 4.1 in time. In the present work the solution of the problem is determined by applying the implicit Newmark's integration scheme. The Newmark method, originally introduced by Newmark [Newmark, 1959], is quite popular for the numerical integration of the equations of motion, especially for nonlinear systems. It has been applied in numerical evaluation of the dynamic response of many engineering structures. The time dimension is represented by a set of discrete points, where Δt is the time increment. The system is solved at each of these points in time using the data of the solution at a previous time.

The Eq. 4.1 can be written at time $t + \Delta t$ as:

$$[\mathbf{M}]\{\ddot{u}_{t+\Delta t}\} + [\mathbf{K}]\{u_{t+\Delta t}\} = \{F_{t+\Delta t}\} \quad (4.6)$$

The acceleration and velocity vectors at time $t + \Delta t$ are written as:

$$\{\ddot{u}_{t+\Delta t}\} = \frac{1}{\beta(\Delta t)^2} \left[\{u_{t+\Delta t}\} - \{u_t\} - (\Delta t)\{\dot{u}_t\} \right] - \frac{1}{\beta} \left(\frac{1}{2} - \beta \right) \{\ddot{u}_t\} \quad (4.7)$$

$$\{\dot{u}_{t+\Delta t}\} = \{\dot{u}_t\} + (\Delta t) \left[(1 - \gamma)\{\ddot{u}_t\} + \gamma\{\ddot{u}_{t+\Delta t}\} \right] \quad (4.8)$$

The variables β and γ are numerical parameters that control both the stability of the method and the amount of numerical damping introduced into the system by the method. For $\gamma = \frac{1}{2}$ there is no numerical damping, for $\gamma \geq \frac{1}{2}$ numerical damping is introduced.

Newmark method is unconditionally stable when $\frac{1}{2} \leq \gamma \leq 2\beta$ and it is unstable when $\gamma < \frac{1}{2}$.

To avoid numerical instability, high frequency dissipation is required. It is achieved when: $\beta = \frac{1}{4}(\gamma + \frac{1}{2})^2$.

In this work, the constant average acceleration version of Newmark method is used, which is implicit and unconditionally stable. For this method γ is $\frac{1}{2}$ and β is $\frac{1}{4}$. Substituting Eq. 4.7 into Eq. 4.6, we obtain a set of nonlinear equations in which the unknowns are $\{u_{t+\Delta t}\}$ and $\{F_{t+\Delta t}\}$. The terms at time (t) are all known. The new system can then be formulated as:

$$[\mathbf{K}^*]\{u_{t+\Delta t}\} = \{F_{t+\Delta t}^*\} \quad (4.9)$$

where $[\mathbf{K}^*]$ is the effective stiffness matrix, and $\{F_{t+\Delta t}^*\}$ is the force vector, which are defined as:

$$[\mathbf{K}^*] = \left[[\mathbf{K}] + \frac{1}{\beta(\Delta t)^2} [\mathbf{M}] \right]$$

$$\{F_{t+\Delta t}^*\} = \{F_{t+\Delta t}\} + [\mathbf{M}] \left\{ \frac{1}{\beta(\Delta t)^2} \{u_t\} + \frac{1}{\beta(\Delta t)} \{\dot{u}_t\} + \left(\frac{1}{2\beta} - 1 \right) \{\ddot{u}_t\} \right\}$$

4.5.3 Calculation of the contact force

In the present work, the contact force is calculated using a modified nonlinear Hertzian contact law proposed by Tan and Sun [Tan and Sun, 1985]. The impactor is modelled as a rigid body with isotropic properties and of higher stiffness compared to the composite plate in the direction of impact. The impactor has radius R_i , mass m_i , Young's modulus E_i and Poisson's ratio ν_i . The initial velocity and displacement of the impactor are $\dot{w}_i = V_0$ and $w_i = 0$. The contact is located at the center of the plate as shown in Figure 4.5. The dynamic equation of the impactor is obtained through Newton's second law, with \ddot{w}_i is the acceleration of the impactor:

$$m_i \ddot{w}_i = -F_c \quad (4.10)$$

The contact force F_c is related to the local indentation α according the contact law, where α is defined as the difference between the displacement of the impactor $w_i(t)$ and the deflection of the plate at the contact point $w_p(t)$:

$$\alpha(t) = w_i(t) - w_p(t) \quad (4.11)$$

During the loading and unloading, the contact force is expressed as follows:

$$F_c = \begin{cases} k\alpha^{3/2} & \text{loading} \\ F_m \left(\frac{\alpha - \alpha_0}{\alpha_m - \alpha_0} \right)^{5/2} & \text{unloading} \end{cases} \quad (4.12)$$

where F_m is the maximum contact force at the beginning of unloading, α_m is the indentation corresponding to F_m . For laminated plate with orthotropic layers, the modified Hertz constant stiffness k can be calculated by:

$$k = \frac{4}{3} \frac{\sqrt{R_i}}{\left(\frac{1-\nu_i^2}{E_i} + \frac{1}{E_z} \right)} \quad (4.13)$$

Where E_z is the transverse modulus normal to the fiber direction in the uppermost composite layer. The permanent indentation α_0 is zero when the maximum indentation α_m is less than a critical value α_{cr} , otherwise α_0 is expressed as:

$$\alpha_0 = \begin{cases} 0 & \alpha_m < \alpha_{cr} \\ \alpha_m \left[1 - \left(\frac{\alpha_{cr}}{\alpha_m} \right)^{2/5} \right] & \alpha_m \geq \alpha_{cr} \end{cases} \quad (4.14)$$

The velocity \dot{w}_i^{n+1} and displacement w_i^{n+1} of the impactor at the time step $n + 1$ are determined by applying implicit Newmark's integration scheme ($\gamma = \frac{1}{2}$ and $\beta = \frac{1}{4}$):

$$\dot{w}_i^{n+1} = \dot{w}_i^n + \ddot{w}_i^n \left(\frac{\Delta t}{2} \right) - F_c^{n+1} \left(\frac{\Delta t}{2m_i} \right) \quad (4.15)$$

$$w_i^{n+1} = w_i^n + \dot{w}_i^n \Delta t + \ddot{w}_i^n \left(\frac{\Delta t^2}{4} \right) - F_c^{n+1} \left(\frac{\Delta t^2}{4m_i} \right) \quad (4.16)$$

Hert'z law is applied at each time step to calculate the contact force. The contact force at time step $n + 1$ is calculated from the impactor and plate displacements of the previous time step n . Substituting Eq. 4.16 into Eq. 4.12, we obtain the contact force at time step $n + 1$:

$$F_c^{n+1} = \begin{cases} k \left[q - w_p^{n+1} - \left(\frac{\Delta t^2}{4m_i} \right) F_c^{n+1} \right]^{3/2} & \text{loading} \\ \frac{F_m}{(\alpha_m - \alpha_0)^{5/2}} \left[q - w_p^{n+1} - \alpha_0 - \left(\frac{\Delta t^2}{4m_i} \right) F_c^{n+1} \right]^{5/2} & \text{unloading} \end{cases} \quad (4.17)$$

Where $q = w_i^n + \dot{w}_i^n \Delta t + \ddot{w}_i^n \left(\frac{\Delta t^2}{4} \right)$.

To seek the solution of the nonlinear problem defined in Eq. 4.17, the Newton-Raphson iteration technique is adopted. Using the initial conditions ($\dot{w}_i = V_0$ and $w_i = w_p = 0$) and a root finding algorithm (Newton-Raphson method), an approximate value of the impact force F_c is obtained from the implicit expressions of the modified nonlinear Hertzian contact law (the first equation of Eq. 4.17). This force is now applied as external load at the contact point of the plate. The nodal displacement w_p of the laminated plate is next found from Eq. 4.9. Using this value of w_p , the impact force F_c is recomputed from Eq. 4.17. The process is repeated until the required accuracy is achieved. The convergence criteria for the satisfaction of the local equilibrium related to the contact force is:

$$|F_c^{n+1}| - |F_c^n| \leq 1.0 \times 10^{-6}$$

The contact force is then used to calculate acceleration, velocity, and displacement of the impactor for the next time step.

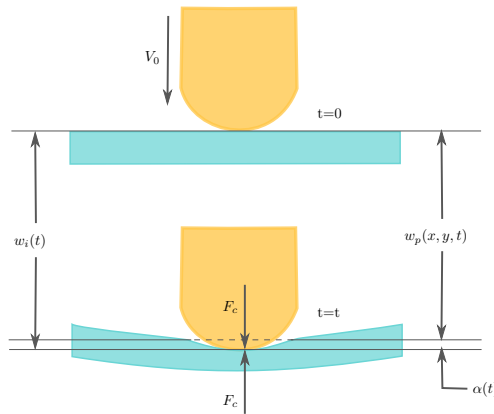


Figure 4.5 – Schematic Illustration of the impact procedure.

4.5.4 Geometrical modelling and Boundary conditions

We have demonstrated in previous chapters that PGD can be used as an alternative to overcome the computational drawbacks of FEM such as the rapid increase in the number of degrees of freedom, the large computational time, and the storage limitation. Now, the predictive capabilities of the PGD approach are evaluated by simulating the low velocity impact response of cross-ply laminates. The impact response analysis is also performed using FE approach.

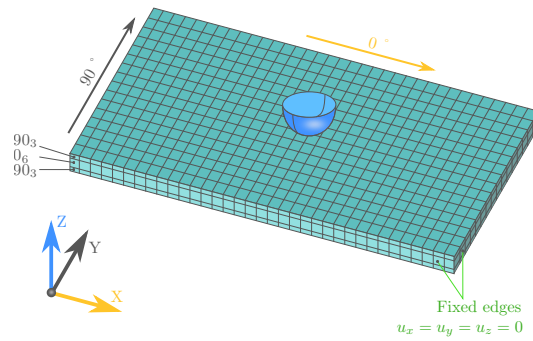
We consider a rectangular plate $60 \times 40 \times 3$ mm made of unidirectional carbon/epoxy material, with stacking sequence $[90_3/0_3]_s$. The cross-ply laminate is assumed to be clamped along all the four edges and impacted at the center by a 12.7 mm diameter aluminum sphere. An initial velocity V_0 is applied to the impactor. All the nodes of the plate edge are fixed in all directions (x, y, z) to simulate the experimental clamped conditions. Figure 4.6 shows the mesh configuration of the finite element model and the PGD model. The boundary conditions are also shown in the same figure. The main advantage of the PGD approach in comparison with the basic FEM approach is the reduction of the computational time. To do that, the 3D mesh is separated into 2D and 1D meshes as represented in Figure 4.6b. The material properties used in the simulations are listed in Table 4.2.

Cohesive properties	$K_I = 1.10^4 \text{ N/mm}^3$; $K_{II} = K_{III} = 5.10^4 \text{ N/mm}^3$ $\sigma_c = 60 \text{ MPa}$; $\tau_c = 139 \text{ MPa}$ $G_{Ic} = 0.3 \text{ N/mm}$; $G_{IIc} = 1.6 \text{ N/mm}$
---------------------	--

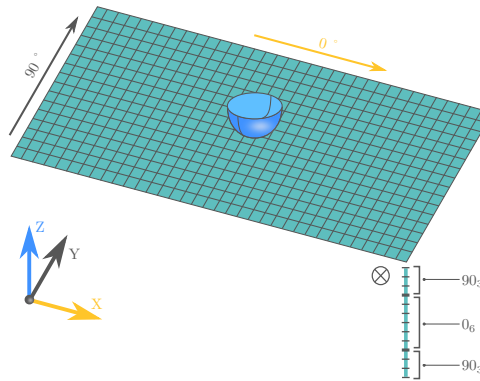
Table 4.1 – Cohesive properties.

4.5.5 Numerical simulations

The modeling of damages is integrated into the impact simulation previously described. The damages due to the low velocity impact is modeled by using a cohesive zone model. The bilinear cohesive law is used to describe both crack initiation and crack propagation. The implementation details and the parameters calibration of the cohesive zone model have already been presented in the previous chapter. The mathematical formulation for a PGD-Cohesive crack problem has also been developed in the previous chapter. Only the practical details are provided in this section. In the PGD model, the smallest element size in the impact zone is $0.3 \text{ mm} \times 0.3 \text{ mm}$. The size of the elements was selected by sensitivity analysis in terms of convergence, structural response and damage propagation. The sensitivity analysis showed that the PGD model is less sensitive to mesh size than the FE model. The fine mesh region on the laminate plane is $40 \text{ mm} \times 20 \text{ mm}$, as shown in Figure 4.6. Each element layer represents one lamina ply.



(a) FE model.



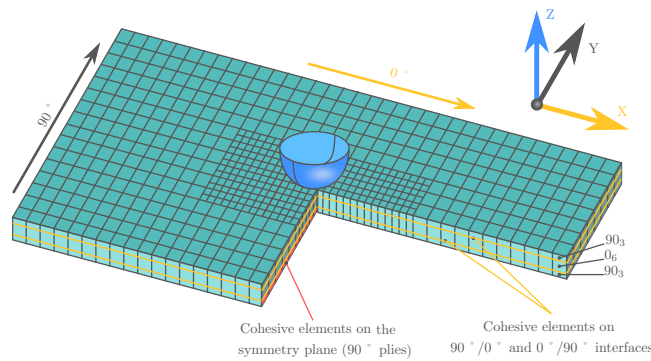
(b) PGD model.

Figure 4.6 – Numerical models used for impact analysis.

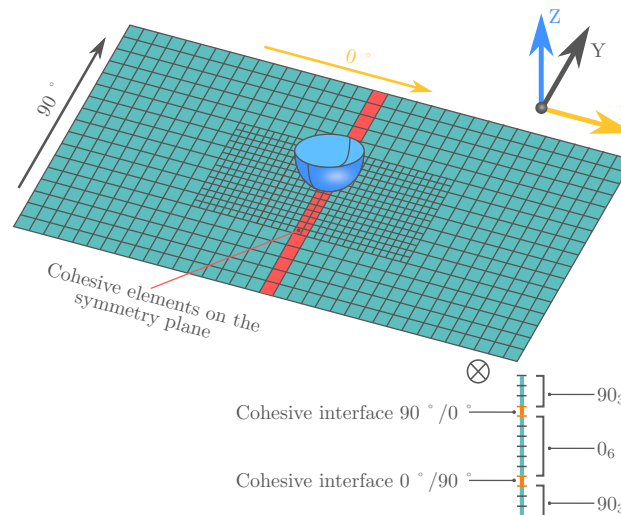
A refined mesh at the center of the plate where the impact load is applied is used as shown in Figure 4.7. As discussed previously, under low-velocity impact, damage is initiated by matrix cracks in the lowest ply of the laminate, which create delaminations at interfaces between plies with different fiber orientations. Based on this analysis and as done in [Aymerich et al., 2009], two rows of vertical cohesive elements are placed on the symmetry plane parallel to the 90° direction to simulate the initiation and growth of the major intralaminar matrix crack (bending crack), typically developing along the fibre direction in the lower block of layers (Figure 4.7). To simulate the initiation and propagation of the delamination, cohesive elements are also inserted at the interfaces between layers with different fiber orientations ($0^\circ/90^\circ$ and $90^\circ/0^\circ$ interfaces). The properties of the cohesive elements are presented in the Table 4.1. The cohesive elements share nodes with the solid elements and have zero thickness.

The PGD-CZM discretization allows a reduction of the number of interface elements in comparison with the FEM discretization, which minimizes modeling complexity. Another asset of the PGD discretization is the easy insertion of the co-

hesive elements. The impact simulation described in the previous section were



(a) FE model.



(b) PGD model.

Figure 4.7 – Location of cohesive elements.

performed with two different initial impact velocities: 1 m.s^{-1} and 3 m.s^{-1} . The mass of the impactor is equal to 2.3 kg . The time step used for the implicit newmark algorithm is 10^{-4} ms . The evolution of the impact force for the two initial impact velocities obtained with the PGD and the FEM are depicted in Figure 4.8. The PGD and the FEM gives very similar results. Figure 4.9 shows the velocity of the impactor-time history. In Figures 4.10 and 4.11 the deflexion of the plate at the contact point and the displacement of the impactor versus time are shown. All the results shows a good agreement between FEM and PGD. The PGD is adapted to perform impact simulation using an incremental implicit newmark scheme. Delamination shape obtained from the PGD simulation at the upper and lower interfaces is shown in Figure 4.12. The simulated results were found coherent with the ones from [Aymerich et al., 2009].

Laminated plate	$E_x = 157380 \text{ MPa}$; $E_y = E_z = 11873 \text{ MPa}$ $G_{xy} = G_{yz} = G_{xz} = 5051 \text{ MPa}$ $\nu_{xy} = \nu_{yz} = \nu_{xz} = 0.31$
Impactor	$E_i = 207 \text{ GPa}$; $\nu_i = 0.30$ $\rho_i = 7800 \text{ kg/m}^3$; $R_i = 12.7 \text{ mm}$

Table 4.2 – Material properties of the laminate and impactor properties.

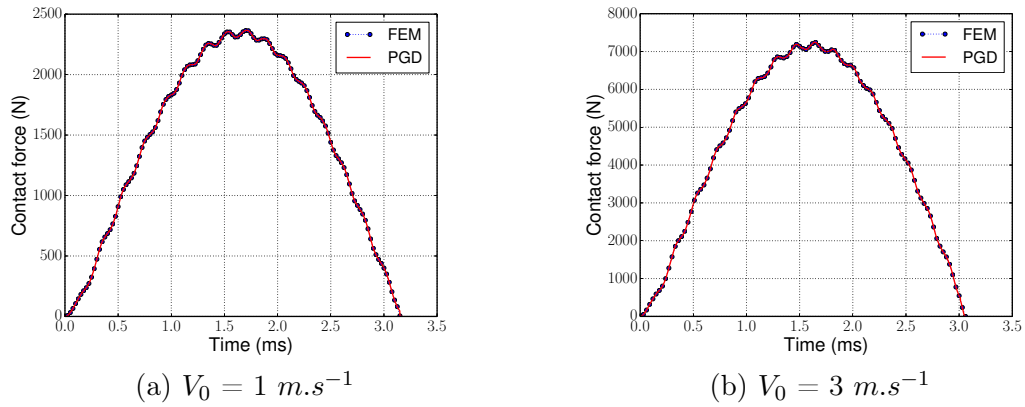


Figure 4.8 – Comparison of contact force-time history.

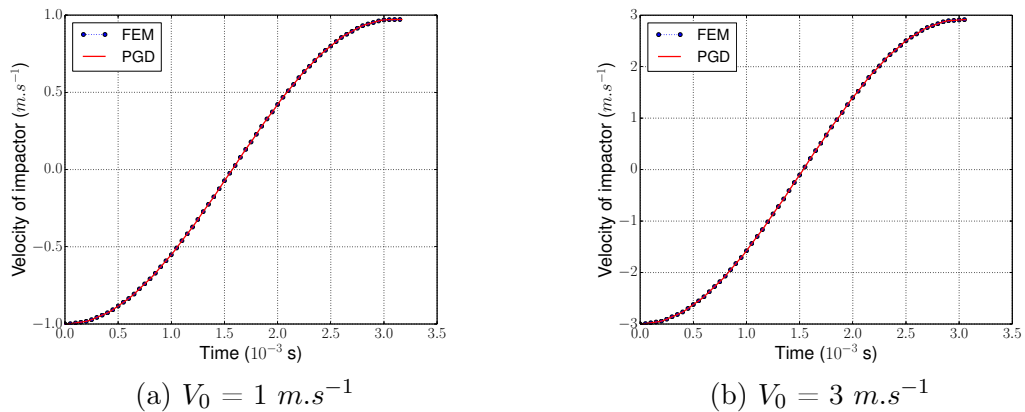
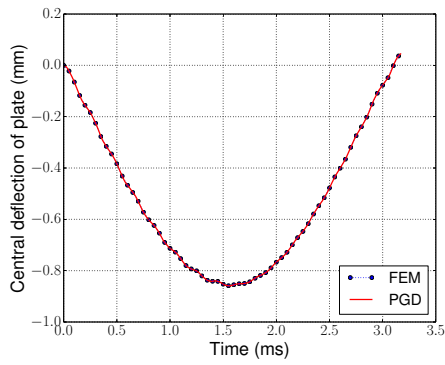
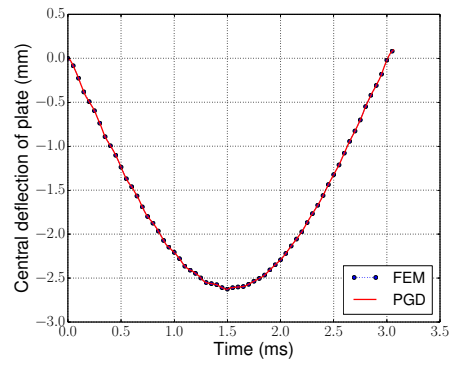


Figure 4.9 – Velocity of the impactor.

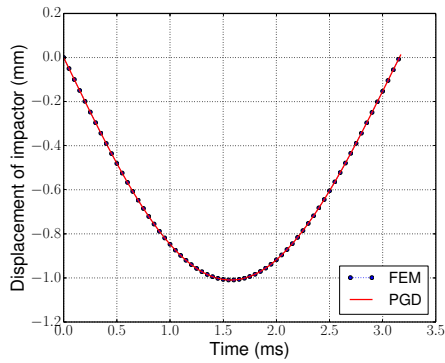


(a) $V_0 = 1 \text{ m.s}^{-1}$

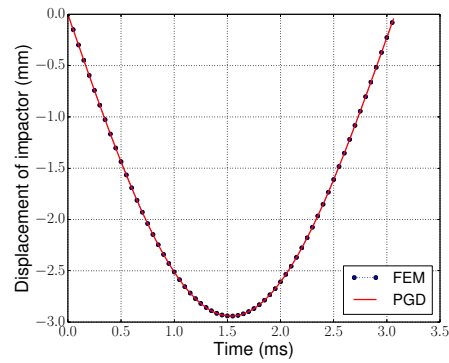


(b) $V_0 = 3 \text{ m.s}^{-1}$

Figure 4.10 – Comparison of plate central displacement-time history.

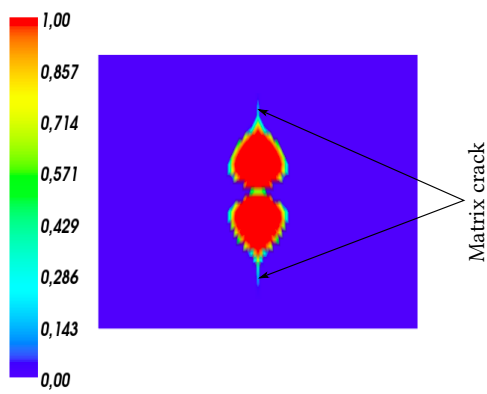


(a) $V_0 = 1 \text{ m.s}^{-1}$

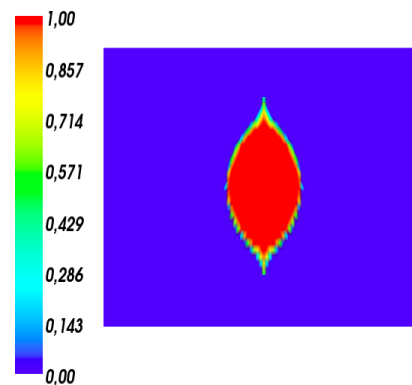


(b) $V_0 = 3 \text{ m.s}^{-1}$

Figure 4.11 – Displacement of the impactor.



(a) Lower interface $0^\circ/90^\circ$.



(b) Upper $90^\circ/0^\circ$.

Figure 4.12 – Delamination areas predicted by the PGD impact model for the laminate $[90_3/0_3]_s$ subjected to impact velocity 3 m.s^{-1} .

Chapter 5

A multiscale modelling of composite materials with periodic structures

“ The important thing in science is not so much to obtain new facts as to discover new ways of thinking about them. ”

Sir William Bragg

Contents

5.1	What are multiscale methods?	81
5.2	Heterogeneous materials with a periodic structure	82
5.3	Multiscale methods in computational mechanics	83
5.3.1	Periodic homogenization theory	83
5.3.2	Domain decomposition methods	85
5.3.3	Multigrid methods	92
5.4	A separated representation for 1D domains	94
5.4.1	Separated description of the 1D problem	94
5.4.2	First iteration	96
5.4.3	Other iterations	99
5.4.4	Boundary conditions	100
5.5	A separated representation for 2D/3D domains	101
5.5.1	Mechanical model	101
5.5.2	Separated description of 2D problems	102
5.5.3	First iteration and operators assembly	103

5.6	Numerical simulations	105
5.6.1	Numerical results of 2D problem	105
5.6.2	Numerical results of 3D problem	110

One of the main challenges in mechanics and engineering is to account for physical phenomena that occur at different scales. A coupling between scales is often observed, generating a real need for multiscale models in many applications. A major difficulty related to multiscale modeling is the need of multiscale solvers that require a lot of computational resources. Therefore, there is a real need for computational methods able to reduce the cost of such simulations. To reduce significantly the cost of a multiscale approach, additional hypotheses have to be introduced. In this work, materials with periodic structures are considered with an obvious application in composite materials. The key idea in this work is to use the periodicity of a microstructure to separate two scales: the scale of the periodic pattern and the macroscopic scale. This is done using a separated representation of the solution in the context of the PGD.

5.1 What are multiscale methods, and why do we need them ?

Multiscale phenomena are part of our daily lives. We organize our time in days, months and years, as a result of the multiscale dynamics of the solar system. Our society is organized in a hierarchical structure, from towns to states, countries and continents. Such a structure has its historical and political origin, but it is also a reflection of the multiscale geographical structure of the earth [Weinan, 2011]. From the viewpoint of physics (as is the case in materials science, mechanical, civil, chemistry, electrical and other engineering disciplines), many problems involve several coupled phenomena that occur over a range of time and length scales, which are difficult to capture in a single simulation. These problems are often multiphysics by nature. The simplest approach to model multiscale phenomena is to focus on the macroscopic scale using mathematical models to describe the behavior of the structure. The effect of the microscopic mechanism is modeled by some physical laws. The physical laws, which play a key role in modeling, are often obtained empirically, by fitting a small set of experimental data.

However, extending these simple empirical approaches to more complex systems have had limited success. This is why mathematical models for complex physical systems are sometimes restricted to macroscale quantities, whereas microscale parameters do not explicitly enter into the model. In order to handle this problem, the mathematical models have to be adapted. The mathematical models for a physical system that account for macro and micro scale are generally very complicated (larger number of evolution variables, coupled interacting fields) and sometimes even virtually impossible to solve. It requires a high degree of refinement in the finite element mesh making the simulations extensive and complicated. It may be necessary to increase computational resources and develop powerful numerical methods. This is where multiscale modeling comes in. The term multiscale

modeling is widely used to describe some approaches based on a hierarchy of simulation to simulate systems across different scales. It is widely recognized that multiscale techniques will become an essential part of computational science and engineering. The multiscale approach opens up unprecedented opportunities for modeling, by focusing on the different levels of physical laws and the relations between them. It influences the way we view the relation between mathematics and science, by considering simultaneously models at different scales.

Many branches of science and engineering today have adopted materials made from two or more constituent materials with significantly different physical or chemical properties. These are composite materials, combining two or more constituents in order to optimize some physical properties of the material. A special case of paramount importance among composite materials is formed by those having a periodic microstructure. Composite materials have mainly periodic or nearly periodic microstructures (woven composites, unidirectional composites). Let us consider a periodic composite material. Two scales are distinguished: the macroscopic one is the length scale on which the system interacts with its environment, and the microscopic one, where the distance of recurrence is much smaller than the dimensions defining the macroscale. The resulting microscale pattern is referred to as the physical system's microstructure. The microscale pattern can also be called representative volume element (RVE), which must be small enough to allow us to distinguish the microscopic heterogeneities and sufficiently large to be representative of the overall behavior [Stolz, 2010].

The multiscale techniques have been remarkably successful in studying relationships between microscopic and macroscopic mechanical quantities of composite materials. These approaches have also been used to get a deeper understanding of the internal physical phenomena. The effective (average) characteristics of a composite material can also be determined by doing experimental testing, but doing that is very time expensive. Some of the most widely used multiscale approaches will be briefly described below.

5.2 Heterogeneous materials with a periodic structure

Our interest focuses on composites materials which have been playing an increasingly significant role in engineering design. Many composite materials often have periodic or nearly periodic microstructures, resulting in inhomogeneous properties in microscale. The structure of periodic heterogeneous materials can be viewed as the disjoint union of a recurrent element (unit cell) of fixed size, which is repeated periodically in space. Periodicity not only simplifies the microstructure representation, but aims at describing the effective (macroscopic) properties of composite

materials by means of the characteristics of their microstructures. A typical unidirectionally reinforced fibrous composite material is shown below in the Figure 5.1a. It is constituted by a succession of fibers arranged in parallel and impregnated with a resin matrix. Another example would be the textile composite, which have complex microstructures in a periodic order. These two examples of periodic composite materials and the corresponding unit cells are illustrated in Figure 5.1.

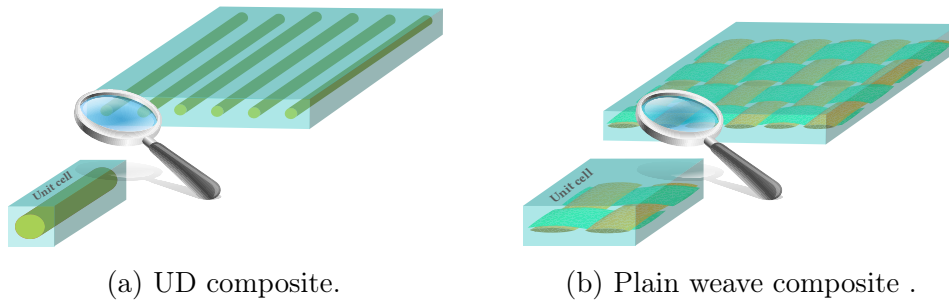


Figure 5.1 – Periodic composite materials and corresponding unit cells.

5.3 Multiscale methods in computational mechanics

This section is an introduction to multiscale methods in computational mechanics. We are going to have a brief survey of the general ideas behind the homogenization theory, domain decomposition methods and multigrid methods. Available homogenization processes are numerous. They can be classified according to the material structure either periodic or random. Our interest focuses on the method of homogenization for periodic structures.

5.3.1 Periodic homogenization theory

The certainly most common method to treat multiscale problems is to use the homogenization theory. In mathematical terms, the periodic homogenization theory describes the mathematical techniques for the asymptotic study of physical system with a periodic or nearly periodic microstructure. The homogenization procedure usually contains two scales (macroscale and microscale). The microscale refers to a representative volume element (RVE). We need to pay attention to the proper selection of RVE and boundary conditions. The overall aim of homogenization is to describe the relationship between the local structure of a heterogenous system and its macroscopic behavior. Homogenization is widely used to predict the effective elastic properties of composite material. This is achieved through averaging the microscopic information. The effective properties can then be used to treat the macrostructure. The composite structure is then replaced by an equivalent

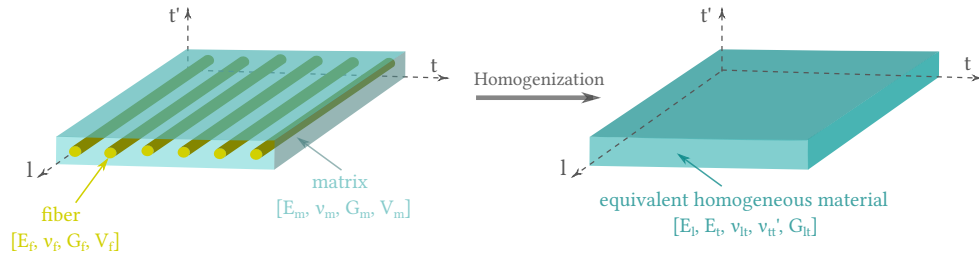


Figure 5.2 – Homogenization of UD composite material.

homogeneous material having the calculated effective properties. The material is said to be homogenized, see Figure 5.2. Generally, there are two principle steps in homogenization procedures [Yang, 1999]:

- Compute microscopic problems with RVE to get local stress and strain;
- Use homogenization method to link microscopic problem to macroscopic problem, and get the global stress and strain.

It is to be noticed that homogenization was one of the first multiscale methods. This theory was developed by various researchers [Bensoussan et al., 1978; Pavliotis and Stuart, 2008; Tartar, 2009], when Ivo Babuska introduced this term to the mathematical literature [Babuska, 1976]. The basic modeling principles have not changed since then. Identification of the effective material properties for composite materials dates back to the 19th century. Especially in the absence of computers, analytical and semi-analytical approximations based on homogenization were developed [Eshelby, 1957; Hashin, 1962; Hill, 1965; Mori and Tanaka, 1973]. Homogenization methods were first developed in the framework of linear elasticity. Nevertheless, the analytical homogenization theories have certain limitations and inconvenient assumptions, like assumptions in the link between micro and macro behavior, and restriction to small strain.

Nevertheless, a variety of interesting numerical homogenization methods have been proposed for problems with periodic microstructure [Christman et al., 1989; Sluis et al., 1999; Tvergaard, 1990]. They offer the possibility of computing the macroscopic response by solving a series of numerical tests on a representative volume element (RVE). These approaches offer also the possibility to get informations about the local solution. The homogenization techniques have been applied to treat the variability using non periodic macroscopic cells at dimensions far below the REV [Pineau and Dau, 2012]. It has been also extended for nonlinear materials in the context of the multiscale finite element method [Feyel, 1999; Feyel and Chaboche, 2000].

The concept of periodic homogenization theory Let us now consider a periodic material as depicted in Figure 5.3, a material occupying a domain Ω and which exhibits a periodic microstructure. Because of the periodicity, we can divide Ω into periodic cubic cells of side length ε , which we call Y . This kind of material is called εY -periodic. Suppose that the phenomenon we are interested in is modeled

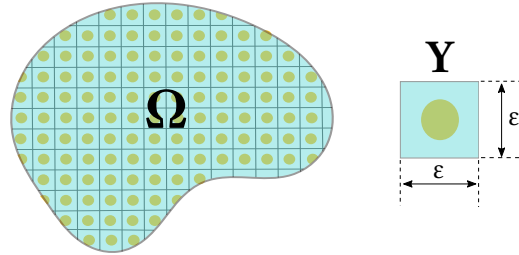


Figure 5.3 – Illustration of the periodicity cell concept.

by the equation:

$$\mathcal{A}u = f, \quad \text{in } \Omega \quad (5.1)$$

Where \mathcal{A} is a differential operator describing the physics of the phenomenon and the properties of the material, u is the unknown function, and f a given source function. There are also the required initial and boundary conditions. We note h a macroscopic characteristic dimension. Even though the material is strongly heterogeneous, in a macroscopic scale it appears to behave like a homogeneous material for large values of h . In other words, the microstructure becomes finer and finer as $\frac{\varepsilon}{h}$ tends to zero. Let us now describe the main idea behind the homogenization theory. If \mathcal{A} defines a medium with fine structured heterogeneities, Eq. 5.1 may be replaced by a sequence of equations:

$$\{\mathcal{A}_h u_h = f\}, \quad \text{in } \Omega \quad (5.2)$$

Each equation of this sequence corresponds to one cubic cell. Having still the same source function f in the domain Ω and the same kind of boundary conditions (periodic conditions), we desire to find a macroscopic equation representative of Eq. 5.2:

$$\mathcal{A}_{hom} u_{hom} = f, \quad \text{in } \Omega \quad (5.3)$$

With \mathcal{A}_{hom} the homogenized operator and u_{hom} the homogenized solution. The homogenized operator \mathcal{A}_{hom} describes the effective properties of the material. The equation 5.3 is a good approximation of the physical equation 5.1.

5.3.2 Domain decomposition methods

Though homogenization approaches are attractive, they present some drawbacks. A first restriction is that homogenization involves choosing some representative

microscopic boundary conditions. Another point to consider is that the homogenization theory postulates a well separated definition of scales. For example, the modeling of a crack can be achieved at microscopic scale, or at macroscopic scale, but is not possible if a crack begins at microscopic scale and propagates until it becomes macroscopic. The averaging required by homogenization may be too restrictive in some applications. To overcome these limitations of the homogenization theory, other approaches based on domain decomposition methods have been proposed. Domain decomposition methods are a family of methods developed to solve partial differential equations (PDEs). The basic idea is to decompose the computational domain into smaller, less complicated, subdomains and to add interface conditions on the boundary between subdomains that are iteratively modified to reach the global convergence.

Finding the global solution requires that:

- The equation is satisfied in each subdomain;
- The local solutions match on the interfaces between the subdomains.

The equations in the subdomains are solved by a direct method whereas the matching of the solutions is enforced iteratively. The convergence rate is very sensitive on the interface conditions. Contrary to direct methods, they are naturally parallel and adapted to multiprocessing technology. But such methods are also very useful when used on monoprocessor computers. These techniques are mainly used in the context of high performance computing. One other advantage of the domain decomposition methods is that it permits the use of different numerical techniques in each subdomain. This increases considerably the flexibility of these methods. It provides simpler and less complicated problems and geometries.

Domain decomposition methods can be categorized into two major classes, namely overlapping methods and non-overlapping methods. Just as the naming of the two categories implies, there are two ways of subdividing the original domain:

- With disjoint subdomains;
- With overlapping subdomains.

Figure 5.4 depicts an overlapping decomposition and a non-overlapping decomposition of the initial domain Ω .

Overlapping domain decomposition methods

Here we describe the family of Schwarz iterative algorithms. It consists of the classical alternating Schwarz method and several of its parallel extensions, such as the additive and multiplicative Schwarz methods.

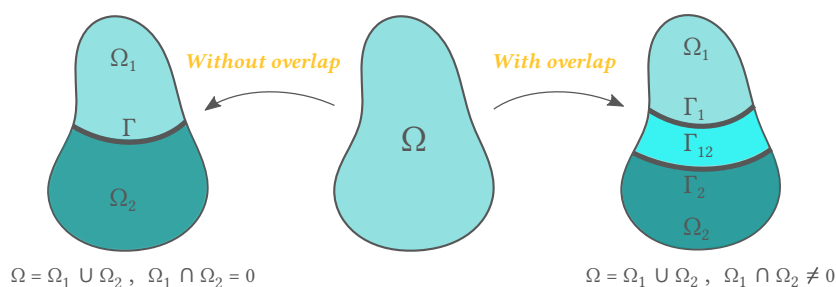


Figure 5.4 – Example of overlapping and non-overlapping decomposition of an initial domain Ω .

Schwarz methods The main idea behind the overlapping domain decomposition methods can be described by the first domain decomposition method: the classical alternating Schwarz method [Schwarz, 1870]. This method was introduced by the mathematician Hermann Andarouse Schwarz in 1870 as an iterative method to prove the existence of solutions to Poisson’s equation, which consists in finding $u: \Omega \rightarrow \mathbb{R}$ such that:

$$\begin{aligned} -\Delta u &= f & \text{in } \Omega \\ u &= 0 & \text{on } \partial\Omega \end{aligned} \quad (5.4)$$

His idea was to study the case of a domain Ω that is the union of two subdomains, a circle Ω_1 and a rectangle Ω_2 with interfaces $\Gamma_1 = \partial\Omega_1 \cap \Omega_2$ and $\Gamma_2 = \partial\Omega_2 \cap \Omega_1$, as depicted in Figure 5.5. Γ_1 is the artificial internal boundary of subdomain Ω_1 , and Γ_2 is the artificial internal boundary of subdomain Ω_2 .

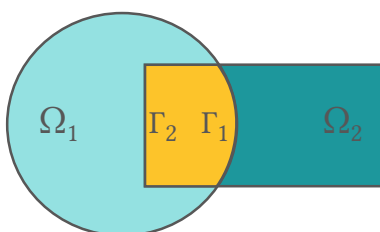


Figure 5.5 – Original geometry used to introduce the alternating Schwarz method.

u_1^n is the solution on Ω_1 and u_2^n is the solution on Ω_2 . This method starts by selecting an initial guess u_2^0 and then updates u_1^n and u_2^n iteratively for $n = 0, 1, 2, \dots$. The better approximate solutions u_1^{n+1} and u_2^{n+1} are determined by solving alternately the two following problems:

$$\begin{aligned} -\Delta u_1^{n+1} &= f & \text{in } \Omega_1 & & -\Delta u_2^{n+1} &= f & \text{in } \Omega_2 \\ u_1^{n+1} &= 0 & \text{on } \partial\Omega_1 \cap \partial\Omega & \text{and} & u_2^{n+1} &= 0 & \text{on } \partial\Omega_2 \cap \partial\Omega \\ u_1^{n+1} &= u_2^n & \text{on } \Gamma_1 & & u_2^{n+1} &= u_1^n & \text{on } \Gamma_2 \end{aligned}$$

Note also that this algorithm is sequential, the problem has to be solved first in Ω_1 then in Ω_2 . From u_2^n , one can obtain some boundary condition on the internal boundary Γ_1 of subdomain Ω_1 and use it to find for u_1^{n+1} , and vice versa. The boundary conditions can either be Dirichlet or Neumann type, or other boundary conditions. If the boundary conditions are chosen properly, the solution will eventually converge. Parallel computing has become the dominant paradigm in computer architecture. In order to benefit from the possibility of using parallel computing to speed up the computation, the original sequential algorithm has been modified by Lions [Lions, 1988]. This can be done by using an iterative method which solves concurrently problems in all subdomains. This method is called the additive Schwarz method. Given a first couple of iterates (u_1^0, u_2^0) , solve:

$$\begin{array}{llll} -\Delta u_1^{n+1} = f & \text{in } \Omega_1 & -\Delta u_2^{n+1} = f & \text{in } \Omega_2 \\ u_1^{n+1} = 0 & \text{on } \partial\Omega_1 \cap \partial\Omega & u_2^{n+1} = 0 & \text{on } \partial\Omega_2 \cap \partial\Omega \\ u_1^{n+1} = u_2^n & \text{on } \Gamma_1 & u_2^{n+1} = u_1^n & \text{on } \Gamma_2 \end{array}$$

The benefit of this algorithm is the saving in memory requirements. The Schwarz alternating method can readily be extended to the case when there are more than two subdomains, this is called multiplicative Schwarz method. Lions proved the convergence of the algorithm by variational approach [Lions, 1988] and also by the maximum principle [Lions, 1989].

Non-overlapping domain decomposition methods

The overlapping methods described previously have some drawbacks. Because of the duplication of unknowns on the overlap, increasing the number of subdomains means that the number of unknowns increases also and routines for manipulating meshes are needed. The second limitation is that, when studying the mechanical behavior of heterogeneous materials made of different constituents with different elastic properties, a natural way to partition the computational domain would be to split each part into a subdomain, but that is not possible with overlapping subdomains. This limitation also appears when solving a coupled multiphysics problem. In order to remedy the drawbacks of the overlapping methods, non-overlapping methods have been developed.

Schur complement methods The Schur complement method is the earliest version of non-overlapping domain decomposition methods in which coupling is performed through common interfaces [Gosselet and Rey, 2006]. It is also called iterative substructuring method, the subdomains intersect only on their interface. This method is obviously well suited for large-scale parallel computation. Its main feature is to compute the solution on the interface between the subdomains by eliminating the unknowns in the interiors of the subdomains. The remaining Schur complement system on the unknowns associated with subdomain interfaces is solved by the conjugate gradient method. The solution on the interface is then

used to compute the solution for each subdomain. The domain Ω in which the differential equation is defined is partitioned into two non-overlapping subdomains s and s' :

$$\Omega = s \cup s', \quad s \cap s' = \emptyset$$

We define the interface between subdomains (Figure 5.6):

$$\Gamma = \partial s \cap \partial s'$$

Schur complement methods can furthermore be distinguished in primal and dual methods:

- In primal methods, like the Balancing Domain Decomposition (BDD) and its variants [Mandel, 1993; Tallec, 1994], the continuity of the solution between each subdomain is insured by introducing a unique displacement field on the interface between subdomains, and looking for the equilibrium of the reaction forces;
- In dual methods, such as Finite Element Tearing and Interconnecting (FETI), the continuity is enforced by the use of Lagrange multipliers [Farhat and Roux, 1991].

Hybrid methods, such as Dual-Primal Finite Element Tearing and Interconnecting (FETI-DP), have also been introduced [Farhat et al., 2000]. Balancing Domain Decomposition by Constraints (BDDC) was introduced by Dohrmann [Dohrmann, 2003] as a simpler primal alternative to the FETI-DP method. Now FETI-DP and BDDC are considered as efficient as original FETI and BDD.

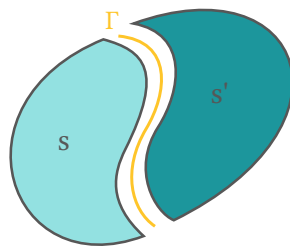


Figure 5.6 – Non-overlapping domain decomposition.

We suppose that the linear equation system to solve is:

$$\mathbf{K}u = f \tag{5.5}$$

where \mathbf{K} is the assembled matrix of a finite element model (example: a stiffness matrix), u is the corresponding set of degrees of freedom and f is the generalized force vector. The local equilibrium of each subdomain can be written as:

$$\forall s, \quad \mathbf{K}^{(s)}u^{(s)} = f^{(s)} + \lambda^{(s)} \tag{5.6}$$

$\lambda^{(s)}$ is the reaction imposed by neighboring subdomains on subdomain (s), while it is non-zero only on its interface $\partial\Omega_s$. The global equilibrium of the interface reactions is then given by:

$$\sum_s \mathbf{A}^{(s)} \mathbf{t}^{(s)} \lambda^{(s)} = 0 \quad (5.7)$$

The global continuity of the displacement field through the interface can be written as:

$$\sum_s \mathbf{B}^{(s)} \mathbf{t}^{(s)} u^{(s)} = 0 \quad (5.8)$$

We will use subscript b for interface data and subscript i for internal data.

$\mathbf{t}^{(s)}$ is the local trace boolean operator defined by $u_b^{(s)} = \mathbf{t}^{(s)} u^{(s)}$.

$\mathbf{A}^{(s)}$ is the primal assembly boolean operator (such as $u_b^{(s)} = \mathbf{A}^{(s)T} u_b$) and $\mathbf{B}^{(s)}$ is the dual assembly signed boolean operator, that verify:

$$\sum_s \mathbf{B}^{(s)} \mathbf{A}^{(s)T} = 0 \quad (5.9)$$

Schur complement methods consist in solving a condensed problem on the interface between the subdomains. The local condensed operators are operators that represent how neighboring subdomains see one subdomain [Gosselet and Rey, 2006].

Primal Schur complement The principle of method based on the primal Schur complement is to write the interface problem in terms of one unique unknown interface displacement field $u_b^{(s)} = \mathbf{A}^{(s)T} u_b$, automatically ensures the verification of Eq. 5.8. If we renumber the local degrees of freedom of subdomain (s) in order to separate internal and boundary degrees of freedom, system 5.6 then becomes:

$$\begin{pmatrix} \mathbf{K}_{ii}^{(s)} & \mathbf{K}_{ib}^{(s)} \\ \mathbf{K}_{bi}^{(s)} & \mathbf{K}_{bb}^{(s)} \end{pmatrix} \begin{pmatrix} u_i^{(s)} \\ u_b^{(s)} \end{pmatrix} = \begin{pmatrix} f_i^{(s)} \\ f_b^{(s)} + \lambda_b^{(s)} \end{pmatrix} \quad (5.10)$$

The condensed form of the local equilibrium of subdomains expressed in terms of interface field can be written as follow:

$$\mathbf{S}_p^{(s)} u_b^{(s)} = \lambda_b^{(s)} + f_c^{(s)} \quad (5.11)$$

$$\text{where: } \begin{cases} \mathbf{S}_p^{(s)} \text{ is the local primal Schur complement} \\ \mathbf{S}_p^{(s)} = \mathbf{K}_{bb}^{(s)} - \mathbf{K}_{bi}^{(s)} \mathbf{K}_{ii}^{(s)-1} \mathbf{K}_{ib}^{(s)} \\ f_c^{(s)} \text{ is the condensed effort imposed on the substructure} \\ f_c^{(s)} = f_b^{(s)} - \mathbf{K}_{bi}^{(s)} \mathbf{K}_{ii}^{(s)-1} f_i^{(s)} \end{cases}$$

The computation of $\mathbf{K}_{ii}^{(s)-1}$ for all (s) can be treated with separated processors. The global equilibrium of the decomposed structure is then given by:

$$\mathbf{S}_p u_b = f_c \quad (5.12)$$

$$\text{where: } \begin{cases} \mathbf{S}_p = \sum_s \mathbf{A}^{(s)} \mathbf{S}_p^{(s)} \mathbf{A}^{(s)T} \\ f_c = \sum_s \mathbf{A}^{(s)} f_c^{(s)} \end{cases}$$

This system can be solved using a direct solver or an iterative method, for example the conjugate gradient algorithm.

Dual Schur complement The principle of dual Schur complement methods (like FETI method) is to write the interface problem in terms of one unique unknown interface effort field $\lambda_b = \mathbf{B}^{(s)T} \lambda_b^{(s)}$, that automatically ensures the verification of Eq. 5.7. So, if $\mathbf{K}^{(s)+}$ is the generalized inverse of matrix $\mathbf{K}^{(s)}$ and $\mathbf{R}^{(s)}$ the kernel of matrix $\mathbf{K}^{(s)}$, from Eqs. 5.10 and 5.11 we have:

$$\begin{cases} u^{(s)} = \mathbf{K}^{(s)+} (\lambda^{(s)} + f^{(s)}) + \mathbf{R}^{(s)} \alpha^{(s)} \\ \mathbf{R}^{(s)T} (\lambda^{(s)} + f^{(s)}) = 0 \end{cases} \quad (5.13)$$

where vector $\alpha^{(s)}$ denotes the magnitude of rigid body motions. The local equilibrium 5.13 of the subdomain (s) is condensed on the interface $\partial\Omega_s$ by introducing the local dual Schur complement $\mathbf{S}_d^{(s)}$:

$$u_b^{(s)} = \mathbf{S}_d^{(s)} \lambda_b^{(s)} + u_c^{(s)} + \mathbf{R}_b^{(s)} \alpha^{(s)} \quad (5.14)$$

$$\text{with: } \begin{cases} \mathbf{S}_d^{(s)} = \mathbf{t}^{(s)} \mathbf{K}^{(s)+} \mathbf{t}^{(s)T} \\ u_c^{(s)} = \mathbf{t}^{(s)} \mathbf{K}^{(s)+} f^{(s)} \\ \mathbf{R}_b^{(s)} = \mathbf{t}^{(s)} \mathbf{R}^{(s)} \end{cases}$$

From Eqs. 5.14 and 5.8, and recalling the condition given by the second equation of 5.13, the global interface problem can be written as:

$$\begin{pmatrix} \mathbf{S}_d & \mathbf{G} \\ \mathbf{G}^T & 0 \end{pmatrix} \begin{pmatrix} \lambda_b \\ \alpha \end{pmatrix} = \begin{pmatrix} -f \\ -e \end{pmatrix} \quad (5.15)$$

$$\text{with: } \begin{cases} \mathbf{S}_d = \sum_s \mathbf{B}^{(s)} \mathbf{S}_d^{(s)} \mathbf{B}^{(s)T} \\ \mathbf{G} = (\dots \mathbf{B}^{(s)} \mathbf{R}_b^{(s)} \dots) \\ f = \sum_s \mathbf{B}^{(s)} u_c^{(s)} \\ e = (\dots f_b^{(s)T} \mathbf{B}^{(s)} \mathbf{R}_b^{(s)} \dots)^T \end{cases} \quad (5.16)$$

A complete overview of various domain decomposition methods may be found in a few books or in the proceedings of various conferences on domain decomposition methods [Chan and Mathew, 1994; Quarteroni and Valli, 1999; Smith et al., 1996; Chan et al., 1989]. Figure 5.7 show the two major groups of domain decomposition methods and its sub-groups. The domain decomposition methods have two major

disadvantages. First, the local problems may need high number of iterations to converge. Second, the convergence of iterative solvers depends on the number of processors. The ideal situation occurs when each processor deals with only one subdomain. The algorithm needs to interchange data across the boundaries, which leads to communication between the processors. Each communication involves additional cost for the data transmitted. Periodic domain decomposition uses a distributed-memory parallel technique for finite periodic geometries. It distributes unit cell mesh subdomains to a network of processors. Though very successful when applied to finite periodic geometries, the communication between the processors is often the limiting factor.

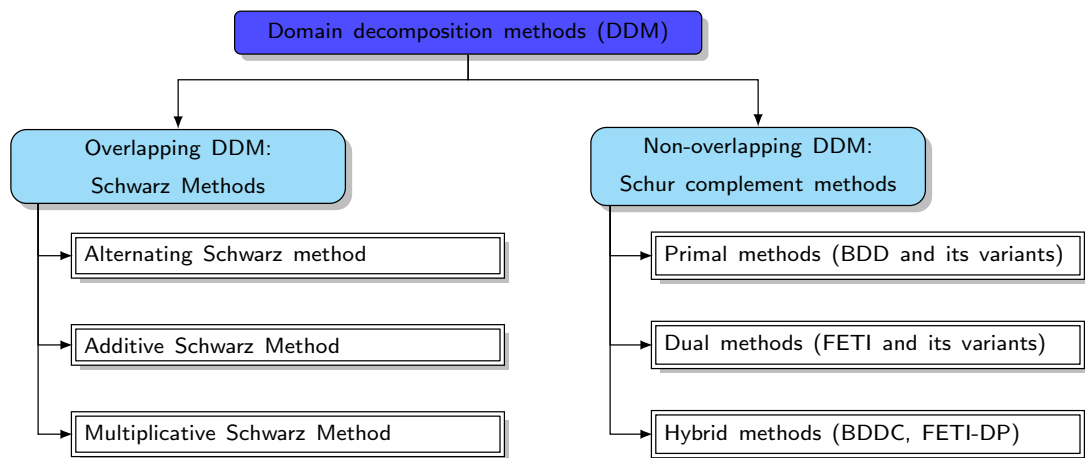


Figure 5.7 – Families of domain decomposition solvers.

5.3.3 Multigrid methods

Multigrid methods have proved to be the fastest numerical methods for solving elliptic and hyperbolic partial differential equations (PDEs) and can be applied in combination with any of the common discretization techniques. They have optimal complexity, are very flexible and can be used for a wide variety of problems. Multigrid algorithm iterates over a hierarchy of successively coarser grids until the convergence is reached. The main characteristic of the multigrid iteration is its fast convergence. The idea of systematically using sets of coarser grids to accelerate the convergence of iterative schemes that arise from the numerical solution of partial differential equations was made popular by the work of Brandt [Brandt, 1977]. The convergence speed does not deteriorate when the discretisation is refined, whereas classical iterative methods slow down for decreasing grid size.

The multigrid methods can yield a solution with computational cost proportional to the size of the problems. The CPU time and storage space are of order $O(N)$,

where N is the size of the problem [Golub and Ortega, 1993]. Basic iterative methods like Jacobi and Gauss-Seidel methods are characterized by global poor convergence rates. That is because these methods remove high frequency errors efficiently, but are inefficient for low frequency errors. High frequency errors are rough errors and low frequency errors are smooth errors. These smooth components are responsible for the slow global convergence. In order to speed up the convergence when the error becomes smooth after a few iterations, the error can be projected to a coarse grid as it becomes rough on a coarse scale grid. On the other hand, the high-frequency components of the error are reduced by applying basic iterative methods like Jacobi or Gauss-Seidel schemes. For this reason these methods are called smoothers.

There are two approaches for solving discretized nonlinear PDEs by multigrid methods:

- The first is based on the Newton method and uses the multigrid scheme as inner solver of the linearized equations;
- The second uses a variant of multigrid method directly to the nonlinear problem, this is known as the Full Approximation Scheme (FAS)[Brandt, 1982].

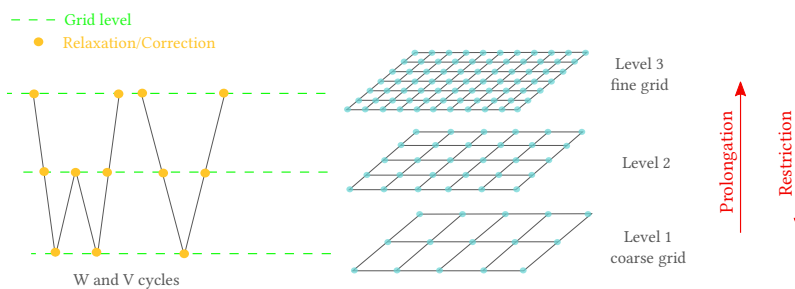


Figure 5.8 – Graphical illustration of the hierarchical grid levels.

To illustrate the FAS method, consider the nonlinear problem $\mathbf{A}(u) = f$. The f subscript is related to the fine grid and c subscript is related to the coarse grid. We summarise the basic steps of the two-level FAS algorithm as follows [Jimack, 2007].

Step 8 of the above algorithm is solved using two-level multigrid algorithm. This idea can be generalized to any number of multigrid levels (see Figure 5.8). γ is the number of times the multigrid procedure is applied to the coarse level problem. This procedure converges very fast, $\gamma = 1$ or $\gamma = 2$ are the typical values used. For $\gamma = 1$ the multigrid scheme is called V-cycle, whereas $\gamma = 2$ is named W-cycle.

Algorithm 1 Two-level FAS algorithm.

- 1: Choose initial fine grid solution u^f
 - 2: Update u^f applying α^1 iterations of the nonlinear smoother
 - 3: Find the residual: $r^f = \mathbf{A}^f(u^f) - f^f$
 - 4: Restrict the residual to the coarse grid: $r^f \rightarrow r^c$
 - 5: Restrict the solution to the coarse grid: $u^f \rightarrow u^c$
 - 6: Calculate the coarse grid right-hand side: $f^c = \mathbf{A}^c(u^c) - r^c$
 - 7: Save the initial coarse grid solution: $u_{init}^c = u^c$
 - 8: Call γ times the multigrid scheme to solve the system $\mathbf{A}^c(u^c) = f^c$
 - 9: Calculate the coarse grid correction: $e^c = u^c - u_{init}^c$
 - 10: Interpolate the correction: $e^c \rightarrow e^f$
 - 11: Correct the fine grid solution: $u^f = u^f + e^f$
 - 12: Update u^f by applying α^2 iterations of the nonlinear smoother.
-

5.4 A multiscale separated representation for periodic 1D domains

5.4.1 Separated description of the 1D problem

For the sake of simplicity, the method will be described firstly for a simple 1D problem. The 2D and 3D cases will be addressed in the next section. Then, an 1D problem with a periodic geometry and materials properties is considered in this section. The weak formulation of the static equilibrium equation for a beam in traction/compression with an elastic homogeneous material is:

$$\int_0^L AE \frac{dU^*}{dX} \frac{dU}{dX} dX = \left[AE U^* \frac{dU}{dX} \right]_0^L \quad (5.17)$$

E is the elastic modulus, A is the area of the beam, U is the longitudinal displacement, X is the coordinate along the beam axis and U^* is a trial function. L denotes the length of the beam. The right hand term is related to the boundary conditions on the left ($x = 0$) and on the right ($x = L$) of the domain. To enforce the boundary conditions, a penalty method will be used. This method will be described in the subsection 5.4.4. For now, the method will be presented without accounting for boundary conditions. The weak formulation is then becomes :

$$\int_0^L AE \frac{dU^*}{dX} \frac{dU}{dX} dX = 0 \quad (5.18)$$

In the finite element method, this weak form is approximated using some shape functions over each element. The proposed strategy takes advantage of the periodicity of the mesh. The domain is sliced into identical elementary parts assuming a periodic geometry and material properties for the truss. The loading and boundary

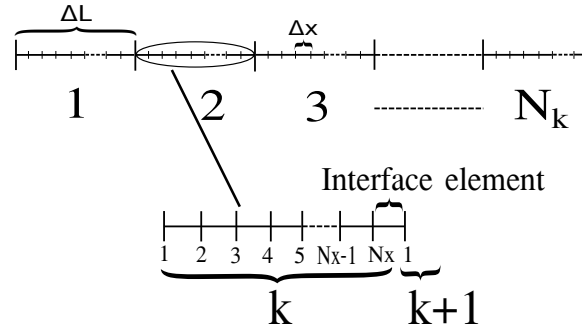


Figure 5.9 – 1D mesh and decomposition in elementary parts.

conditions may differ from one part to another. Each occurrence of the periodic pattern is associated to an integer denoted k as shown in Figure 5.9. k is an integer such as $k \in [1, N_k]$, and N_k denotes the number of patterns. The coordinate X defining the horizontal position in the beam is written using k :

$$X = (k - 1) \Delta L + x \quad (5.19)$$

$x \in [0, \Delta L]$ is the position in each part and ΔL is the total length of each part. The continuous form of the displacement field found using the separated approximation of the solution is given by :

$$U(X) = U((k - 1) \Delta L + x) = \sum_{i=1}^n F_i(x) G_i(k) \quad (5.20)$$

The discrete form of the Eq. 5.20 can be written as:

$$U(X) = \sum_{i=1}^n \underline{F}_i \otimes G_i \quad (5.21)$$

where \otimes is the tensor product. In the following, the notation $U(k, x) = U((k - 1) \Delta L + x)$ will be used. Using k and x instead of X leads to a double definition of the position at the edge of the elementary parts: $U(k, \Delta L) = U(k + 1, 0)$. This is problematic from a numerical point of view because it leads to a multiplication of degrees of freedom on these points. There are two possibilities to treat the edge of the elementary part:

1. Solving the problem using more degrees of freedom than necessary and as well as using boundary conditions to enforce the continuity: $U(k, \Delta L) = U(k + 1, 0)$.
2. Deleting some nodes when discretizing the domain in order to suppress the non-necessary degrees of freedom.

The first method is not well-adapted to the classical PGD solver. For instance, if the beam is clamped in $x = 0$, the boundary condition is:

$$U(1, 0) = 0 \quad (5.22)$$

In general, the separated representation is built term by term. Therefore, each term of the series must satisfy the boundary condition. In most cases, that leads to verify:

$$F_i(x = 0) = 0 \quad \forall i \in [1, n] \quad (5.23)$$

But this will also enforce some unwanted conditions:

$$U(k, 0) = U((k - 1) \Delta L) = 0 \quad \forall k \in [1, N_k] \quad (5.24)$$

Even if some solutions exist to enforce the boundary condition, such as using a penalty method and computing many terms of the separated approximation at the same time, the convergence of the PGD remains slow and unsatisfactory. The second strategy is clearly more efficient. In the following, only the second strategy is described. Let us consider a finite element discretization of the domain with equally distributed nodes as shown in Figure 5.9. This distribution of nodes is only for sake of clarity without loss of generality. The size of an element is denoted Δx . Then, the weak formulation Eq. 5.18 can be rewritten:

$$\sum_{k=1}^{N_k} \left(\int_{(k-1)\Delta L}^{k\Delta L - \Delta x} AE \frac{dU^*}{dX} \frac{dU}{dX} dX \right) + \sum_{k=1}^{N_k-1} \left(\int_{k\Delta L - \Delta x}^{k\Delta L} AE \frac{dU^*}{dX} \frac{dU}{dX} dX \right) = 0 \quad (5.25)$$

The first sum contains integrals defined on the elements that are inside the elementary parts. The second sum contains integrals defined over the interface elements. There is only $N_k - 1$ terms on the second sum because there is no interface element on the right. The right boundary condition needs a special treatment that will be detailed later. With a change of variable between X and x it comes:

$$\underbrace{\sum_{k=1}^{N_k} \left(\int_0^{\Delta L - \Delta x} AE \frac{dU_k^*}{dx} \frac{dU_k}{dx} dx \right)}_{I_1} + \underbrace{\sum_{k=1}^{N_k-1} \left(\int_{\Delta L - \Delta x}^{\Delta L} AE \frac{dU_k^*}{dx} \frac{dU_k}{dx} dx \right)}_{I_2} = 0 \quad (5.26)$$

5.4.2 First iteration

The approximation defined by Eq. 5.20 is built term by term. For now, we focus on the first iteration. The displacement is then approximated by:

$$U(X) = F_1(x)G_1(k) = R(x)S(k) \quad (5.27)$$

To avoid the redundant use of subscripts, we denote $R = F_1$ and $S = G_1$. The determination of R and S involves a non-linear problem that is solved using the

classical alternate direction strategy [Ammar et al., 2006]. At the beginning, R is computed assuming a random value for S . Then S is computed knowing R . And again R is computed knowing S and so on until the convergence of R and S are reached. Then, two different problems must be treated:

1. Computing R knowing S
2. Computing S knowing R

The trial function is $U^* = R^*S$ for the first problem and $U^* = RS^*$ for the second problem. The first problem is considered in the following. The first integral of Eq. 5.26 can be simply rewritten using the separated approximation:

$$\begin{aligned} I_1 &= \sum_{k=1}^{N_k} \int_0^{\Delta L - \Delta x} AE \frac{dR^*}{dx} \frac{dR}{dx} S^2(k) dx \\ &= \left(\int_0^{\Delta L - \Delta x} AE \frac{dR^*}{dx} \frac{dR}{dx} dx \right) \sum_{k=1}^{N_k} S^2(k) \end{aligned} \quad (5.28)$$

After a finite element discretization it remains:

$$I_1 \approx (\mathbf{R}^{*\mathbf{T}} \mathbf{K} \mathbf{R}) \times (\mathbf{S}^{\mathbf{T}} \mathbf{I}_{N_k} \mathbf{S}) \quad (5.29)$$

\mathbf{R} is the column matrix containing the nodal values of R :

$$\mathbf{R} = [R_1 \quad R_2 \quad \cdots \quad R_{N_x}]^T \quad (5.30)$$

\mathbf{S} is the column matrix containing the values of S :

$$\mathbf{S} = [S_1 \quad S_2 \quad \cdots \quad S_{N_k}]^T \quad (5.31)$$

\mathbf{K} is the stiffness matrix related to the periodic pattern and \mathbf{I}_{N_k} is the $N_k \times N_k$ identity matrix. The second integral in Eq. 5.26 requires a little more development since the degree of freedom corresponding to $U_k(\Delta L) = U_{k+1}(0)$ is defined only on the part $k + 1$. This integral is defined on the interface elements between two parts. For 1D linear elements the shape functions over the interface element are: $\mathbf{N} = [N_{N_x}(x) \quad N_1(x)]$ (see Figure 5.9). For quadratic elements, $\mathbf{N} = [N_{N_x-1}(x) \quad N_{N_x}(x) \quad N_1(x)]$. The matrix of DOF are for linear elements:

$$\mathbf{Q}_k = \begin{bmatrix} R_{N_x} S_k \\ R_1 S_{k+1} \end{bmatrix} \quad (5.32)$$

or for quadratic elements:

$$\mathbf{Q}_k = \begin{bmatrix} R_{N_x-1} S_k \\ R_{N_x} S_k \\ R_1 S_{k+1} \end{bmatrix} \quad (5.33)$$

Using this finite element approximation, I_2 can be written as:

$$I_2 = \sum_{k=1}^{N_k-1} \int_{\Delta L - \Delta_x}^{\Delta L} AE \frac{dU_k^*}{dx} \frac{dU_k}{dx} dx = \sum_{k=1}^{N_k-1} \mathbf{Q}^{*T} \int_{\Delta L - \Delta_x}^{\Delta L} AE \frac{d\mathbf{N}^T}{dx} \frac{d\mathbf{N}}{dx} dx \mathbf{Q} \quad (5.34)$$

Defining $\alpha_{ij} = \int_{\Delta L - \Delta_x}^{\Delta L} E \frac{dN_i}{dx} \frac{dN_j}{dx} dx$ and developing the previous equation in the case of linear elements, I_2 becomes:

$$\begin{aligned} I_2 = & R_{N_x}^* \alpha_{N_x N_x} R_{N_x} \sum_{k=1}^{N_k-1} S_k^2 + R_{N_x}^* \alpha_{1 N_x} R_1 \sum_{k=1}^{N_k-1} S_k S_{k+1} \\ & + R_1^* \alpha_{1 N_x} R_{N_x} \sum_{k=1}^{N_k-1} S_{k+1} S_k + R_1^* \alpha_{11} R_1 \sum_{k=1}^{N_k-1} S_{k+1}^2 \end{aligned} \quad (5.35)$$

In general, four operators may be defined as follows:

$$\begin{aligned} I_2 = & (\mathbf{R}^{*T} \mathbf{M}_{N_x, N_x} \mathbf{R}) \times (\mathbf{S}^T \mathbf{D}_{k,k} \mathbf{S}) + (\mathbf{R}^{*T} \mathbf{M}_{N_x, 1} \mathbf{R}) \times (\mathbf{S}^T \mathbf{D}_{k, k+1} \mathbf{S}) \\ & + (\mathbf{R}^{*T} \mathbf{M}_{1, N_x} \mathbf{R}) \times (\mathbf{S}^T \mathbf{D}_{k+1, k} \mathbf{S}) + (\mathbf{R}^{*T} \mathbf{M}_{1, 1} \mathbf{R}) \times (\mathbf{S}^T \mathbf{D}_{k+1, k+1} \mathbf{S}) \end{aligned} \quad (5.36)$$

where $\mathbf{D}_{k,k}$, $\mathbf{D}_{k+1, k+1}$, $\mathbf{D}_{k+1, k}$ and $\mathbf{D}_{k, k+1}$ are the following $N_k \times N_k$ square matrix:

$$\mathbf{D}_{k,k} = \begin{bmatrix} 1 & 0 & 0 & \cdots & 0 \\ 0 & 1 & 0 & \cdots & 0 \\ \vdots & \ddots & \ddots & \ddots & \vdots \\ 0 & \cdots & 0 & 1 & 0 \\ 0 & \cdots & 0 & 0 & 0 \end{bmatrix} \quad \mathbf{D}_{k+1, k+1} = \begin{bmatrix} 0 & 0 & 0 & \cdots & 0 \\ 0 & 1 & 0 & \cdots & 0 \\ \vdots & \ddots & \ddots & \ddots & \vdots \\ 0 & \cdots & 0 & 1 & 0 \\ 0 & \cdots & 0 & 0 & 1 \end{bmatrix} \quad (5.37)$$

$$\mathbf{D}_{k, k+1} = \begin{bmatrix} 0 & 1 & 0 & \cdots & 0 \\ 0 & 0 & 1 & \ddots & \vdots \\ \vdots & \ddots & \ddots & \ddots & 0 \\ 0 & \cdots & 0 & 0 & 1 \\ 0 & \cdots & 0 & 0 & 0 \end{bmatrix} \quad \mathbf{D}_{k+1, k} = \begin{bmatrix} 0 & 0 & 0 & \cdots & 0 \\ 1 & 0 & 0 & \cdots & 0 \\ 0 & 1 & 0 & \ddots & \vdots \\ \vdots & \ddots & \ddots & \ddots & 0 \\ 0 & \cdots & 0 & 1 & 0 \end{bmatrix} \quad (5.38)$$

and \mathbf{M}_{N_x, N_x} , $\mathbf{M}_{1, 1}$, $\mathbf{M}_{N_x, 1}$ and \mathbf{M}_{1, N_x} are some $N_x \times N_x$ square matrix coming from the development of Eq. 5.34. In the case of linear elements, these matrix are identified from Eq 5.35:

$$\mathbf{M}_{N_x, N_x} = \begin{bmatrix} 0 & 0 & \cdots & 0 \\ \vdots & \ddots & \ddots & \vdots \\ 0 & \cdots & 0 & 0 \\ 0 & \cdots & 0 & \alpha_{N_x N_x} \end{bmatrix} \quad \mathbf{M}_{1, 1} = \begin{bmatrix} \alpha_{11} & 0 & \cdots & 0 \\ 0 & 0 & \cdots & 0 \\ \vdots & \ddots & \ddots & \vdots \\ 0 & \cdots & 0 & 0 \end{bmatrix} \quad (5.39)$$

$$\mathbf{M}_{N_x,1} = \begin{bmatrix} 0 & 0 & \cdots & 0 \\ \vdots & \vdots & \ddots & \vdots \\ 0 & 0 & \cdots & 0 \\ \alpha_{1N_x} & 0 & \cdots & 0 \end{bmatrix} \quad \mathbf{M}_{1,N_x} = \begin{bmatrix} 0 & \cdots & 0 & \alpha_{1N_x} \\ 0 & \cdots & 0 & 0 \\ \vdots & \ddots & \vdots & \vdots \\ 0 & \cdots & 0 & 0 \end{bmatrix} \quad (5.40)$$

The stiffness matrix \mathbf{K} is symmetric. With the separated formulation some operators are non symmetric. However the global problem remains symmetric because: $\mathbf{D}_{k+1,k} = \mathbf{D}_{k,k+1}^T$ and $\mathbf{M}_{1,N_x} = \mathbf{M}_{N_x,1}^T$. The weak formulation Eq. 5.26 gives eventually the system to solve after eliminating \mathbf{R}^* :

$$\begin{aligned} (\mathbf{K}\mathbf{R}) \times (\mathbf{S}^T \mathbf{I}_{N_k} \mathbf{S}) + (\mathbf{M}_{N_x, N_x} \mathbf{R}) \times (\mathbf{S}^T \mathbf{D}_{k,k} \mathbf{S}) + (\mathbf{M}_{N_x, 1} \mathbf{R}) \times (\mathbf{S}^T \mathbf{D}_{k,k+1} \mathbf{S}) \\ + (\mathbf{M}_{1, N_x} \mathbf{R}) \times (\mathbf{S}^T \mathbf{D}_{k+1,k} \mathbf{S}) + (\mathbf{M}_{1, 1} \mathbf{R}) \times (\mathbf{S}^T \mathbf{D}_{k+1,k+1} \mathbf{S}) = 0 \end{aligned} \quad (5.41)$$

And the system for the second problem, that is to compute S knowing R writes:

$$\begin{aligned} (\mathbf{R}^T \mathbf{K} \mathbf{R}) \times (\mathbf{I}_{N_k} \mathbf{S}) + (\mathbf{R}^T \mathbf{M}_{N_x, N_x} \mathbf{R}) \times (\mathbf{D}_{k,k} \mathbf{S}) + (\mathbf{R}^T \mathbf{M}_{N_x, 1} \mathbf{R}) \times (\mathbf{D}_{k,k+1} \mathbf{S}) \\ + (\mathbf{R}^T \mathbf{M}_{1, N_x} \mathbf{R}) \times (\mathbf{D}_{k+1,k} \mathbf{S}) + (\mathbf{R}^T \mathbf{M}_{1, 1} \mathbf{R}) \times (\mathbf{D}_{k+1,k+1} \mathbf{S}) = 0 \end{aligned} \quad (5.42)$$

5.4.3 Other iterations

For other iterations, the assumption is assumed known until the iteration n .

Now, we are looking for $R = F_{n+1}$ and $S = G_{n+1}$ such as:

$$U(x, k) = \sum_{i=1}^n F_i(x) G_i(k) + R(x) S(k) \quad (5.43)$$

The trial function is the same as in the first iteration:

- $U^* = R^* S$ if the unknown is R .
- $U^* = R S^*$ if the unknown is S .

Introducing this expression in the weak form, and using a finite elements discretization as described for the first iteration, if the unknown is R then :

$$\begin{aligned} (\mathbf{K}\mathbf{R}) \times (\mathbf{S}^T \mathbf{I}_m \mathbf{S}) + (\mathbf{M}_{N_x, N_x} \mathbf{R}) \times (\mathbf{S}^T \mathbf{D}_{k,k} \mathbf{S}) + (\mathbf{M}_{N_x, 1} \mathbf{R}) \times (\mathbf{S}^T \mathbf{D}_{k,k+1} \mathbf{S}) \\ + (\mathbf{M}_{1, N_x} \mathbf{R}) \times (\mathbf{S}^T \mathbf{D}_{k+1,k} \mathbf{S}) + (\mathbf{M}_{1, 1} \mathbf{R}) \times (\mathbf{S}^T \mathbf{D}_{k+1,k+1} \mathbf{S}) = \\ - \sum_{i=1}^n [(\mathbf{K}\mathbf{F}_i) \times (\mathbf{S}^T \mathbf{I}_m \mathbf{G}_i) + (\mathbf{M}_{N_x, N_x} \mathbf{F}_i) \times (\mathbf{S}^T \mathbf{D}_{k,k} \mathbf{G}_i) + (\mathbf{M}_{N_x, 1} \mathbf{F}_i) \times (\mathbf{S}^T \mathbf{D}_{k,k+1} \mathbf{G}_i) \\ + (\mathbf{M}_{1, N_x} \mathbf{F}_i) \times (\mathbf{S}^T \mathbf{D}_{k+1,k} \mathbf{G}_i) + (\mathbf{M}_{1, 1} \mathbf{F}_i) \times (\mathbf{S}^T \mathbf{D}_{k+1,k+1} \mathbf{G}_i)] \end{aligned} \quad (5.44)$$

where \mathbf{F}_i and \mathbf{G}_i contain the nodal values of $F_i(x)$ and the values of $G_i(k)$. Since the right part of this equation is known, it defines a vector that is the second member of the system to solve. A very similar system can be easily written when the unknown is S .

The global PGD algorithm is summed up in algorithm 2.

Algorithm 2 General PGD algorithm used to make the link between the elementary cell and the global mesh

- 1: $n = 0$
 - 2: initialize F_{n+1} and G_{n+1} to random values
 - 3: $F_{n+1}^{old} = F_{n+1}$; $G_{n+1}^{old} = G_{n+1}$
 - 4: Compute F_{n+1} knowing G_{n+1} (update the function related to the elementary cell)
 - 5: Compute G_{n+1} knowing F_{n+1} (update the function related to the global mesh)
 - 6: if $\max(\|F_{n+1} - F_{n+1}^{old}\|, \|G_{n+1} - G_{n+1}^{old}\|) > \epsilon_1$ then go to 3
 - 7: $n = n+1$
 - 8: $U(x, k) = \sum_{i=1}^n F_i(x)G_i(k)$ (no need to compute explicitly U)
 - 9: If the residual norm of the system $> \epsilon_2$ then go to 2 (see [Pruliere et al., 2010a] for more details)
-

5.4.4 Boundary conditions

For now, the method has been described without accounting for boundary conditions. As the method is based on a finite element discretization, stress conditions can naturally be introduced by adding a second member to the system to be solved. This second member represents the loadings. The only difference with the classical finite element method is that it must be written on a separated form. To use Dirichlet boundary conditions, a penalty method is recommended. It consists in adding some new operators that describe the boundary conditions. For instance, to enforce a unitary displacement on the left the operators related to boundary conditions are:

$$\mathbf{M}_{\mathbf{bc}} = \beta \begin{bmatrix} 1 & 0 & \cdots & 0 \\ 0 & 0 & \cdots & 0 \\ \vdots & \ddots & \ddots & \vdots \\ 0 & \cdots & 0 & 0 \end{bmatrix} \quad \mathbf{D}_{\mathbf{bc}} = \begin{bmatrix} 1 & 0 & \cdots & 0 \\ 0 & 0 & \cdots & 0 \\ \vdots & \ddots & \ddots & \vdots \\ 0 & \cdots & 0 & 0 \end{bmatrix}$$

$$\mathbf{B}_{\mathbf{bc}}^{\mathbf{x}} = \beta \begin{bmatrix} 1 \\ 0 \\ \vdots \\ 0 \end{bmatrix} \quad \mathbf{B}_{\mathbf{bc}}^{\mathbf{k}} = \begin{bmatrix} 1 \\ 0 \\ \vdots \\ 0 \end{bmatrix}$$

where β is the purely numerical penalty parameter. $\mathbf{M}_{\mathbf{bc}}$ is a $N_x \times N_x$ matrix, $\mathbf{D}_{\mathbf{bc}}$ is a $N_k \times N_k$ matrix, $\mathbf{B}_{\mathbf{bc}}^{\mathbf{x}}$ is a $N_x \times 1$ matrix and $\mathbf{B}_{\mathbf{bc}}^{\mathbf{k}}$ is a $N_k \times 1$ matrix. The system given in Eq. 5.41 becomes with this boundary condition:

$$\begin{aligned} & (\mathbf{KR}) \times (\mathbf{S}^T \mathbf{I}_m \mathbf{S}) + (\mathbf{M}_{N_x, N_x} \mathbf{R}) \times (\mathbf{S}^T \mathbf{D}_{k,k} \mathbf{S}) + (\mathbf{M}_{N_x, 1} \mathbf{R}) \times (\mathbf{S}^T \mathbf{D}_{k, k+1} \mathbf{S}) \\ & + (\mathbf{M}_{1, N_x} \mathbf{R}) \times (\mathbf{S}^T \mathbf{D}_{k+1, k} \mathbf{S}) + (\mathbf{M}_{1, 1} \mathbf{R}) \times (\mathbf{S}^T \mathbf{D}_{k+1, k+1} \mathbf{S}) + (\mathbf{M}_{\mathbf{bc}} \mathbf{R}) \times (\mathbf{S}^T \mathbf{D}_{\mathbf{bc}} \mathbf{S}) \\ & = \mathbf{B}_{\mathbf{bc}}^{\mathbf{x}} \times (\mathbf{S}^T \mathbf{B}_{\mathbf{bc}}^{\mathbf{k}}) \quad (5.45) \end{aligned}$$

Another problem has to be discussed relating to boundary conditions. On the right side, there is obviously no interface element. In comparison to other elementary parts, the right part has one node less on the right. This may be a problem. A simple solution to overcome this difficulty is to add a “virtual” elementary part on the right that is only used for one node. The other nodes are only virtual and the element inside this virtual part have to be ignored.

In operators $\mathbf{D}_{k,k}$, $\mathbf{D}_{k,k+1}$, $\mathbf{D}_{k+1,k}$ and $\mathbf{D}_{k+1,k+1}$, the lines corresponding to the virtual part (the line N_k) must be filled with 0 in order to prevent the effect of virtual element. There is no undesirable numerical error related to the presence of virtual element because the PGD solver is iterative and then there is convergence even if there is no unique solution.

5.5 A multiscale separated representation for periodic 2D/3D domains

5.5.1 Mechanical model

In this section, a 2D or 3D static problem is considered. \underline{U} denotes the displacement vector expressed in the canonical basis:

$$\underline{U}(\underline{X}) = \begin{bmatrix} U_x(\underline{X}) \\ U_y(\underline{X}) \\ U_z(\underline{X}) \end{bmatrix} \quad (5.46)$$

where $\underline{X} = (X, Y, Z)^T$ is the coordinate vector. $\boldsymbol{\varepsilon}$ denotes the strain tensor under matrix form:

$$\boldsymbol{\varepsilon} = \begin{bmatrix} \varepsilon_{xx} \\ \varepsilon_{yy} \\ \varepsilon_{zz} \\ 2\varepsilon_{yz} \\ 2\varepsilon_{xz} \\ 2\varepsilon_{xy} \end{bmatrix} \quad (5.47)$$

and \mathbb{H} is the matrix describing the constitutive equation. The stress tensor under matrix form is written:

$$\begin{bmatrix} \sigma_{xx} \\ \sigma_{yy} \\ \sigma_{zz} \\ \sigma_{yz} \\ \sigma_{xz} \\ \sigma_{xy} \end{bmatrix} = \mathbb{H} \begin{bmatrix} \varepsilon_{xx} \\ \varepsilon_{yy} \\ \varepsilon_{zz} \\ 2\varepsilon_{yz} \\ 2\varepsilon_{xz} \\ 2\varepsilon_{xy} \end{bmatrix} = \mathbb{H}\boldsymbol{\varepsilon} \quad (5.48)$$

In small displacements, $\boldsymbol{\varepsilon}$ is the symmetric gradient of the displacement. With these notations, the weak formulation of the equilibrium equation without dynamic

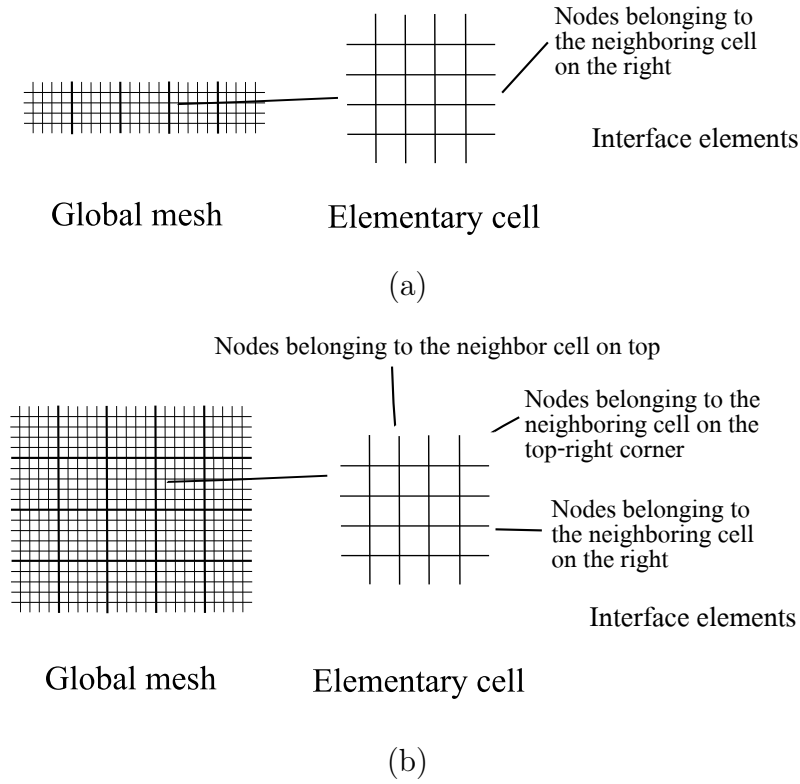


Figure 5.10 – Examples of 2D meshes and decomposition in elementary parts.

effect and volume forces is expressed as :

$$\int_{\Omega} \varepsilon(\underline{U}^*)^T (\mathbb{H}\varepsilon(\underline{U})) \, d\Omega = \int_{\partial\Omega} \underline{U}^* \cdot (\sigma \cdot \underline{n}) \, d\Gamma \quad (5.49)$$

Ω is the domain taken by the structure and $\partial\Omega$ is the boundary of the domain. The right part of this weak formulation is only used for boundary conditions. It is not included in the following for the sake of readability.

5.5.2 Separated description of 2D problems

As for the 1D case, the domain Ω is decomposed into N_k periodic elementary cells Ω_k . Ω_i denotes the set of elements inside the elementary cell and Ω_e is the set of interface elements. Ω_e depends on k because it varies according to the presence of neighboring cells. To avoid the double definition of degrees of freedom at the interface between cells, some nodes need to be deleted at the interface. We choose to delete the nodes on the right and up faces for the 2D case as shown in Figure 5.10.

The local coordinates in the elementary cells are noted \underline{x} . The separated approx-

imation associated to a 2D or a 3D problem is then:

$$\underline{U}(\underline{x}, k) = \sum_{i=1}^n \underline{F}_i(\underline{x}) G_i(k) \quad (5.50)$$

Here, G_i is a scalar function and \underline{F}_i is a vector function:

$$\underline{F}_i(\underline{x}) = \begin{pmatrix} F_i^x(\underline{x}) \\ F_i^y(\underline{x}) \\ F_i^z(\underline{x}) \end{pmatrix} \quad (5.51)$$

$$\underbrace{\sum_{k=1}^{N_k} \int_{\Omega_i} \boldsymbol{\varepsilon}(\underline{U}^*)^T (\mathbb{H} \boldsymbol{\varepsilon}(\underline{U})) \, d\Omega}_{I_1} + \underbrace{\sum_{k=1}^{N_k} \int_{\Omega_{e(k)}} \boldsymbol{\varepsilon}(\underline{U}^*)^T (\mathbb{H} \boldsymbol{\varepsilon}(\underline{U})) \, d\Omega}_{I_2} = 0$$

5.5.3 First iteration and operators assembly

The integral I_1 is treated as for the 1D case.

For the first iteration with $\underline{U}(\underline{x}) = \underline{R}(\underline{x})S(k)$, I_1 writes:

$$\begin{aligned} I_1 &= \left(\int_{\Omega_i} \boldsymbol{\varepsilon}(\underline{R}^*)^T (\mathbb{H} \boldsymbol{\varepsilon}(\underline{R})) \, d\Omega \right) \sum_{k=1}^{N_k} S(k)^2 \\ &\approx (\mathbf{R}^{*\mathbf{T}} \mathbf{K} \mathbf{R}) \times (\mathbf{S}^{\mathbf{T}} \mathbf{I}_{N_k} \mathbf{S}) \end{aligned}$$

\mathbf{K} is the stiffness matrix related to Ω_i and \mathbf{I}_{N_k} is the $N_k \times N_k$ identity matrix. \mathbf{R} is the column matrix containing the nodal values of R^x , R^y and R^z and \mathbf{S} is the column matrix containing the values of S .

The second integral I_2 needs an assembly of new matrices that are representative of interactions between neighboring cells. The element stiffness matrices of each interface elements must be assembled in many adequate global matrices.

For instance, in the first 2D problem depicted in Figure 5.10, I_2 can be written as:

$$I_2 = \sum_{m=1}^4 (\mathbf{R}^{*\mathbf{T}} \mathbf{M}_m^r \mathbf{R}) \times (\mathbf{S}^{\mathbf{T}} \mathbf{D}_m^r \mathbf{S})$$

\mathbf{D}_m^r are the matrices defined by:

$$(\mathbf{D}_1^r)_{i,j} = \begin{cases} 1 & \text{if } i = j \text{ and the cell } i \text{ has a right neighboring cell} \\ 0 & \text{otherwise} \end{cases}$$

$$(\mathbf{D}_2^r)_{i,j} = \begin{cases} 1 & \text{if } i = j \text{ and the cell } i \text{ has a left neighboring cell} \\ 0 & \text{otherwise} \end{cases}$$

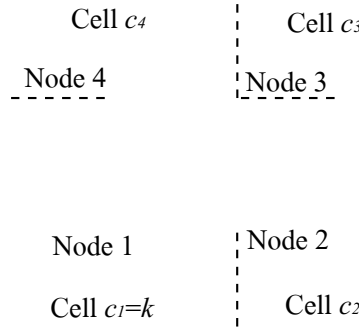


Figure 5.11 – Corner element: nodes and neighboring cells definition

$$(\mathbf{D}_3^r)_{i,j} = \begin{cases} 1 & \text{if the cell } j \text{ is at the right of the cell } i \\ 0 & \text{otherwise} \end{cases}$$

$$(\mathbf{D}_4^r)_{i,j} = \begin{cases} 1 & \text{if the cell } i \text{ is at the right of the cell } j \\ 0 & \text{otherwise} \end{cases}$$

and the matrices \mathbf{M}_m^r are matrices that result from the assembly. It is interesting to notice that $\mathbf{D}_2^r = (\mathbf{D}_1^r)^T$ and $\mathbf{M}_2^r = (\mathbf{M}_1^r)^T$.

The second problem depicted in Figure 5.10 is more complicated. There are now 3 types of interface elements:

- elements between the cell and its right neighbor (subscript r),
- elements between the cell and its top neighbor (subscript t),
- an element in the top-right corner that is at the interface of 4 different cells (subscript c).

The assembly results in the following sum:

$$I_2 = \underbrace{\sum_{m=1}^4 (\mathbf{R}^{*T} \mathbf{M}_m^r \mathbf{R}) \times (\mathbf{S}^T \mathbf{D}_m^r \mathbf{S})}_{\text{right interface elements}} + \underbrace{\sum_{m=1}^4 (\mathbf{R}^{*T} \mathbf{M}_m^t \mathbf{R}) \times (\mathbf{S}^T \mathbf{D}_m^t \mathbf{S})}_{\text{top interface elements}} + \underbrace{\sum_{m=1}^{16} (\mathbf{R}^{*T} \mathbf{M}_m^c \mathbf{R}) \times (\mathbf{S}^T \mathbf{D}_m^c \mathbf{S})}_{\text{corner interface element}}$$

The right interface elements brings the same operators as in the first case. The operators related to the top interface elements are also very similar.

The element on the corner is assembled with 16 operators because it is at the interface of 4 different cells. The assembly of the corner element is detailed as follows.

We assume for illustration that the corner element is the 4 nodes quadrilateral element as shown in Figure 5.11. The nodes belonging to the corner element are numbered from 1 to 4. Each one of these nodes belong to a different cell. The cells around the corner element are noted using some functions of k : c_1 , c_2 , c_3 and c_4 .

$c_1 = k$, c_2 is the cell on the right of k , c_3 is on the top-right of k and c_4 is on the top of k . Using these notations, the element degrees of freedom matrix are:

$$\mathbf{Q}_k^e = \begin{bmatrix} R_1^x S_{c_1} \\ R_2^x S_{c_2} \\ R_3^x S_{c_3} \\ R_4^x S_{c_4} \\ R_1^y S_{c_1} \\ R_2^y S_{c_2} \\ R_3^y S_{c_3} \\ R_4^y S_{c_4} \end{bmatrix} \quad (5.52)$$

The element stiffness matrix of the corner element is noted \mathbf{K}^c . The weak formulation restricted to the corner elements is: $\sum_{k \in \mathcal{C}} (\mathbf{Q}_k^{e\star T} \mathbf{K}^c \mathbf{Q}_k^e)$, where \mathcal{C} denotes the set of cells having an interface element on the top-right corner.

This sum is then decomposed as follow:

$$\sum_{k \in \mathcal{C}} (\mathbf{Q}_k^{e\star T} \mathbf{K}^c \mathbf{Q}_k^e) = \sum_{i=1}^4 \sum_{j=1}^4 \left(\begin{bmatrix} R_i^{x\star} & R_i^{y\star} \end{bmatrix} \begin{bmatrix} \mathbf{K}_{i,i}^c & \mathbf{K}_{i,j+4}^c \\ \mathbf{K}_{i+4,j}^c & \mathbf{K}_{i+4,j+4}^c \end{bmatrix} \begin{bmatrix} R_j^x \\ R_j^y \end{bmatrix} \times \sum_{k \in \mathcal{C}} (S_{c_i(k)} S_{c_j(k)}) \right) \quad (5.53)$$

There are then 16 separated operators. It remains only to assemble these element operators into global operators in order to get \mathbf{M}_m^c and \mathbf{D}_m^c (with $m = 1, 2, \dots, 16$).

Remark: This method requires a lot of separated operators. There are 25 operators for the 2D case treated here and 129 operators for the full 3D case. Though this is a high number, all the matrices are very sparse (some matrices have a few non-zero elements) and finally, the computational cost remains quite acceptable.

5.6 Numerical simulations

In this section, the method described in the previous sections will be considered for solving a variety of test cases in order to evaluate its performance in terms of results precision and computational cost.

5.6.1 Numerical results of 2D problem

Consider an elastic structure subjected to flexion. This structure is composed of a large number of periodic and heterogeneous microstructure which can be represented by a unit cell, as shown in Figure 5.12.

In the following example of simulation, two modeling scales are considered. The microscopic scale is assumed to be the scale at which the microstructure is defined, the unit cell is defined at the microscopic scale. A morphological analysis of the

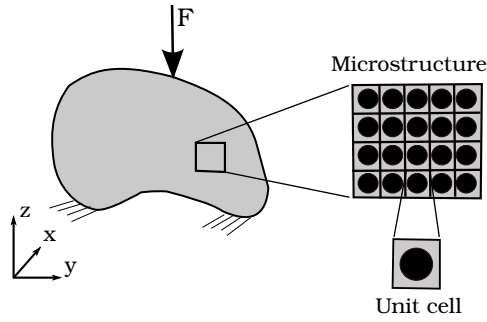


Figure 5.12 – Heterogeneous elastic structure with periodic microstructure.

microstructure was carried out on a section of a carbon fiber reinforced polymer. The micrograph was presumed representative of the microstructure of the analyzed material. This was in order to generate a representative virtual cell. This cell will be used in the following example. The virtual unit cell, as shown in Figure 5.13, is described by the following geometric parameters: the fibers diameters D_1 and D_2 , the distance d_c between the center of the central fiber and the centers of the surrounding fibers, the length L and width l of the cell. The material properties and the geometric parameters are summarized in Table 5.1.

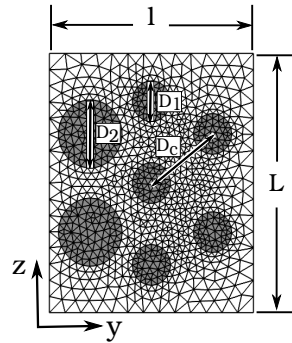


Figure 5.13 – The representative unit cell at the microscale.

Material properties				
E_f (GPa)	E_m (GPa)	ν_f	ν_m	V_f (%)
390	4,5	0,35	0,40	34
Geometric parameters				
D_1 (μm)	D_2 (μm)	d_c (μm)	l (μm)	L (μm)
3	5	6	16	19

Table 5.1 – Material properties and geometric parameters of the virtual cell.

In this subsection, the numerical simulations performed using the PGD are

compared with results of classical FEM implementation using the same set of parameters. The aim is to validate the PGD approach. Here, the finite element method serves as a reference solution. The PGD problem was divided into 20 substructures, each substructure corresponding to one cell. The loads and boundary conditions applied to the microstructure are shown in Figure 5.14.

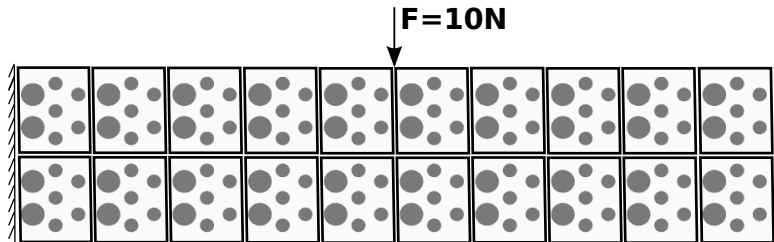


Figure 5.14 – Domain decomposed into subdomains and boundary conditions.

The unit cell mesh is composed of 986 nodes. The finite element mesh was constructed by assembling the meshes of 20 unit cells. A total of 19283 nodes involving 38566 degrees of freedom are used. A 2D triangular element with 3-nodes is used for both models. The displacements of the microstructure are depicted in Figure 5.15. The PGD approach gives quite similar results for the displacements.

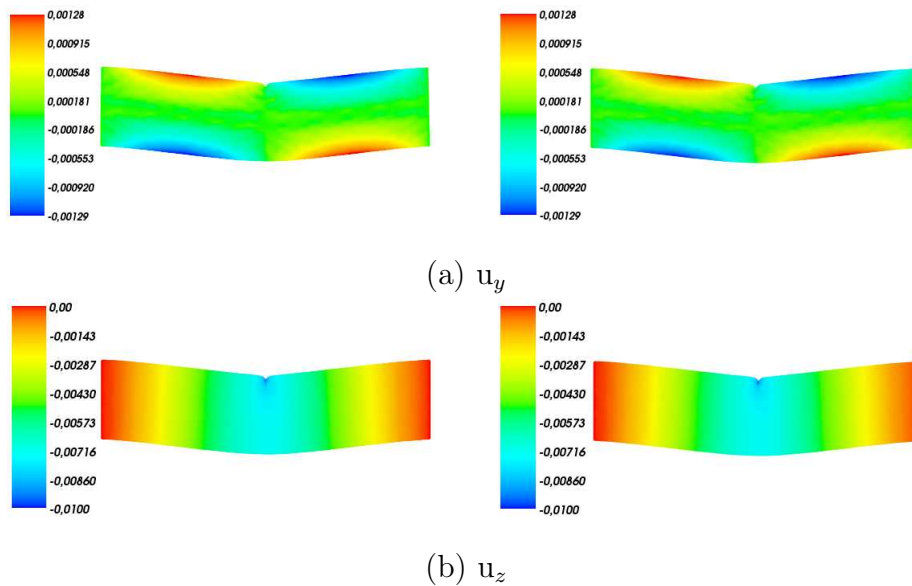


Figure 5.15 – Displacement fields (mm) : FEM solution (left) - PGD solution (right).

The stresses distributions are plotted in Figure 5.16. The results of the PGD are in excellent agreement with the 2D FEM solution. The PGD approach is able to fully capture the stress concentration in the microstructure.

Figures 5.17 and 5.18 give the distribution of the displacements and the stresses through the thickness (coordinate z) for different values of the y coordinate chosen

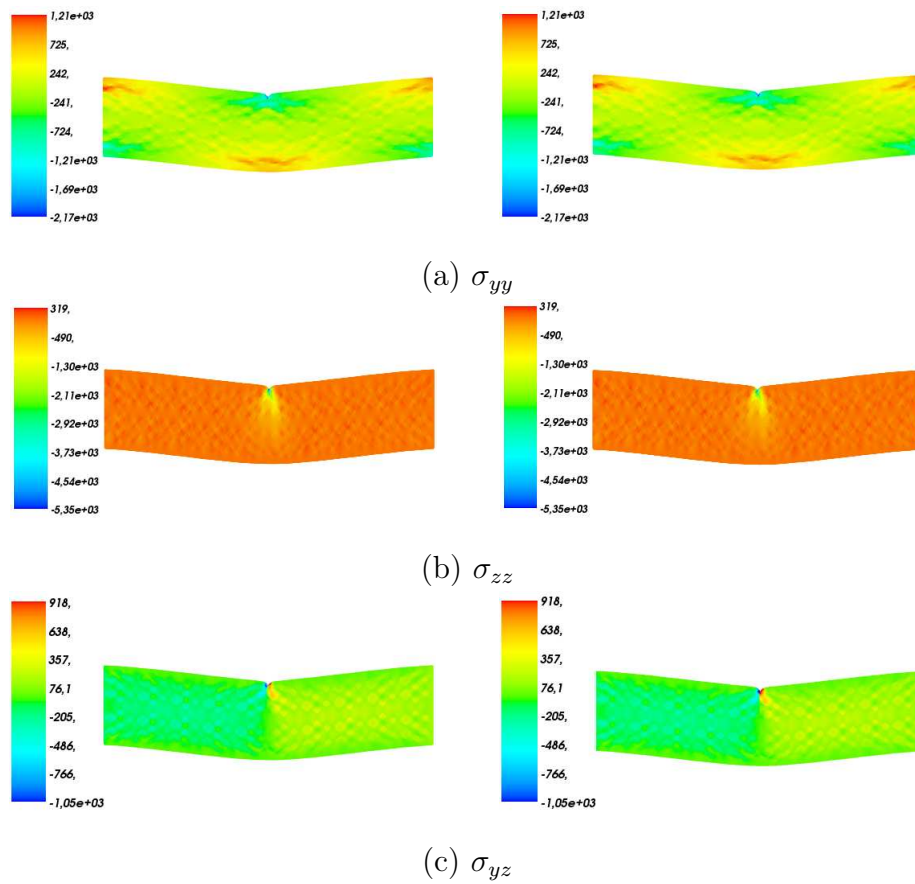


Figure 5.16 – Stresses distributions : FEM solution (left) - PGD solution (right).

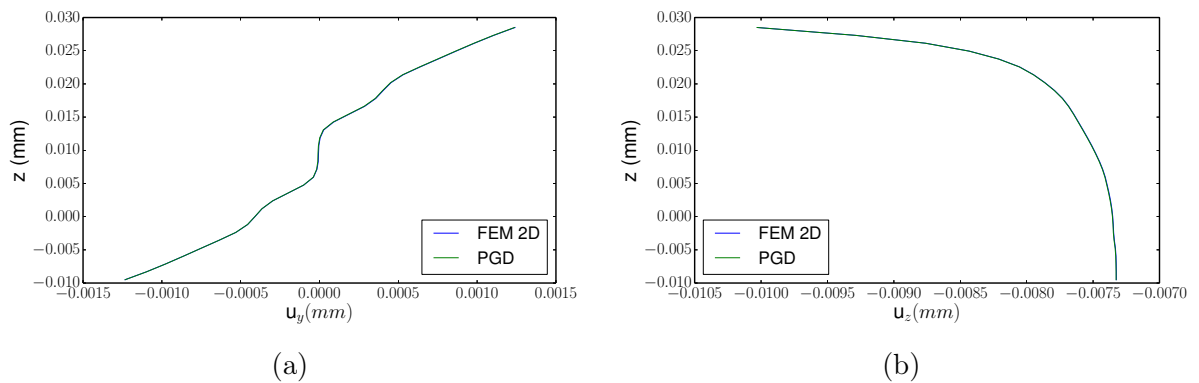


Figure 5.17 – Convergence study on the distribution of the displacements along the thickness: (a) u_y for $y=0.04$ mm, (b) u_z for $y=0.072$ mm.

to be the most critical for each displacement and stress component. Referring to these figures, the PGD solution performs very well with respect to the 2D reference solution. These figures show also that the errors on the displacement and the stress

between both approaches are negligible.

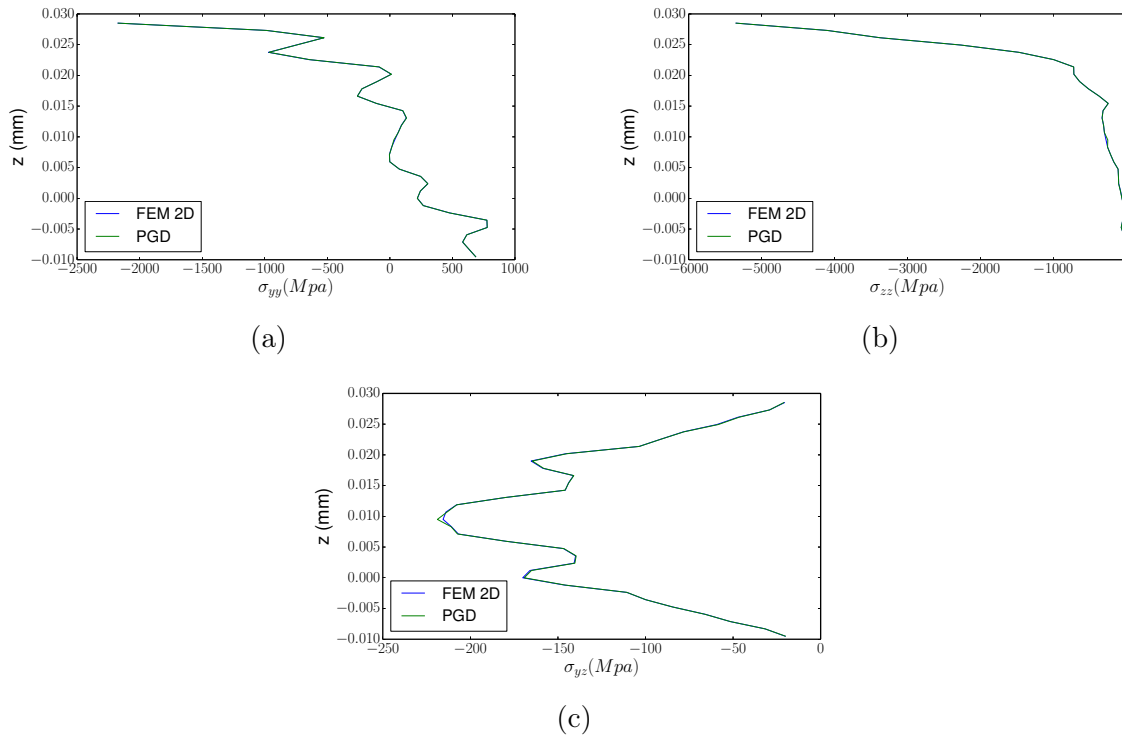


Figure 5.18 – Convergence study on the distribution of the stresses along the thickness: (a) σ_{yy} for $y=0.072$ mm, (b) σ_{zz} for $y=0.072$ mm, (c) σ_{yz} for $y=0.04$ mm.

In this example of simulation, the computational time using python did not exceed 3 minutes on a personal laptop. To check its dependence on the subdomains number, we depict in Figures 5.19 and 5.20 the evolution of the computational time associated to each model versus the subdomains number and the number of degrees of freedom (DOF). As the number of subdomains increases, the computational time required for convergence of PGD solution increases slightly, as shown in Figure 5.19. The slope proves that the computational time increases in a similar way with the subdomains number and with the number of degrees of freedom (DOF). It is obvious that the PGD drastically reduce the calculation cost for a large number of subdomains, while the resolution of a full 2D problem by FEM has involved millions degrees of freedom and a much higher computational and memory cost as shown in Figure 5.20. We can conclude on the efficiency of the proposed strategy that proceeds with impressive computing time savings without compromising the solution accuracy.

For estimating the convergence of PGD, we compute the normalized norm of residue. Figure 5.21 depicts the evolution of the error with the number of terms n in the separated representation of $\underline{U}(\underline{x}, k)$. As one can see, the error decreases as the number of terms in the decompositions increases. At this point, it is interesting

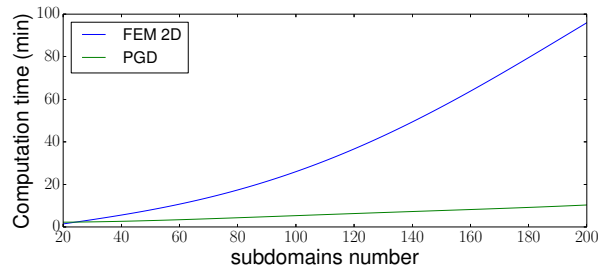


Figure 5.19 – Computing time against number of subdomains.

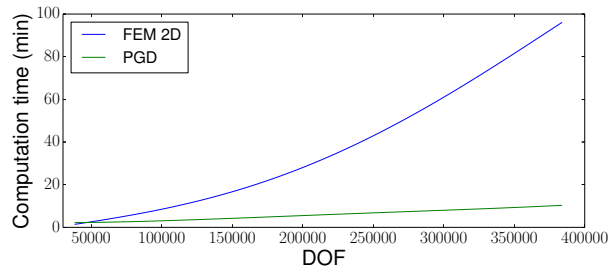


Figure 5.20 – Computing time against number of degrees of freedom (DOF).

to note that the number of couples does not depend on the number of unit cells. As can be noticed, 90 iterations seem to be sufficient to reach convergence in the alternating directions fixed point algorithm described in algorithm 2.

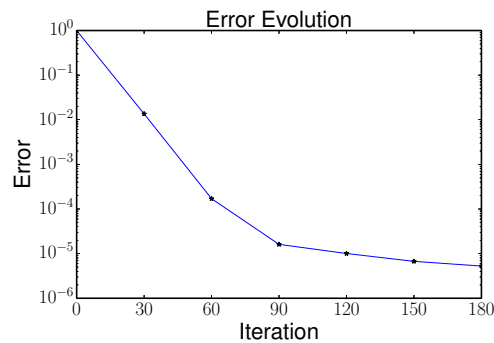


Figure 5.21 – Convergence of PGD solution.

5.6.2 Numerical results of 3D problem

To validate the efficiency of the proposed technique, a multiscale 3D model is used to simulate the mechanical behaviour of woven composite materials. This model is difficult to treat using a classical finite element solver with 3D solid elements. It consists in a two-ply composite made from woven carbon fibers (taffeta) and

epoxy resin.

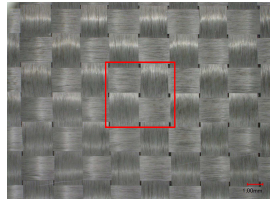
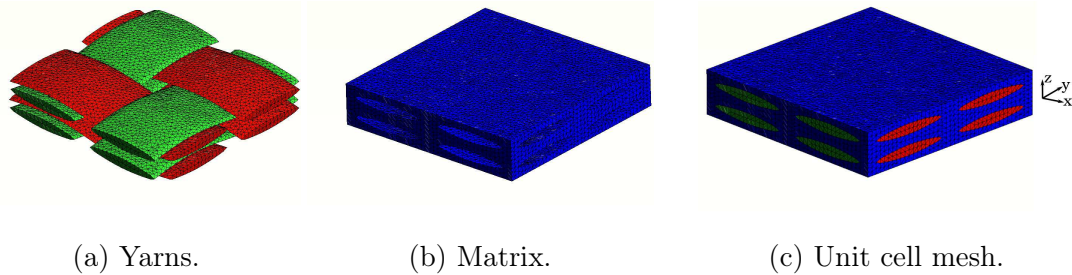


Figure 5.22 – Woven carbon fiber.



(a) Yarns.

(b) Matrix.

(c) Unit cell mesh.

Figure 5.23 – Periodic tetrahedral mesh of unit cell model.

Woven reinforcements are generally periodic media: in fact, they consist of a repeating pattern or a unit cell to reconstruct the complete composite fabric, as shown in Figure 5.22. Due to the geometrical complexity of woven composites architecture, the 3D geometric model was built using TexGen software as shown in Figure 5.23(a). TexGen is a very powerful tool to generate geometric models for composite textiles. The TexGen model is transferred to ABAQUS. As could be seen in figure Figure 5.23(b), the matrix volume is then created by subtracting the yarns volume. The next step is to construct the finite element mesh of the unit cell. In order to do the simulations, the mesh of the unit cell must be periodic. Figure 5.23(c) shown the 3D 4 nodes periodic tetrahedral mesh of unit cell model. The unit cell dimension is $2 \times 2 \times 0.42$ (mm). PGD simulations were carried out using linear elastic behaviours, the matrix and the yarns were assumed to be respectively isotropic and orthotropic. Material properties of the matrix and the effective properties of the yarns are given in Table 5.2. The unit cell mesh is composed of

Matrix		Effective properties of yarn					
E_m (GPa)	ν_m	E_x (GPa)	E_y (GPa)	ν_{xy}/ν_{xz}	ν_{yz}	G_{xy}/G_{xz} (GPa)	G_{yz} (GPa)
3500	0.3	234.345	45.743	0.327	0.375	20.056	16.628

Table 5.2 – Material property.

28934 nodes. The PGD problem was divided into 25 substructures which gives a total of 706390 nodes involving 2119170 degrees of freedom. The displacement along z of the composite plate is zero on both ends (for $x = 0$ and $x = x_{max}$). A

constant pressure is applied on the top face of the unit cell positioned at the center of the plate. A visualization of the deformed configuration is presented in Figure 5.24 and puts emphasis on the displacements. The maximum displacement value in the z direction logically appears at the middle of the plate where the load is applied. The stress values for the plate are analyzed and presented in the Figure 5.25. These stress fields are complex because of the heterogeneity of the model and of the orthotropic behavior of the yarn. With the proposed reduced strategy, these stress fields are accessible with a relatively low computational cost.

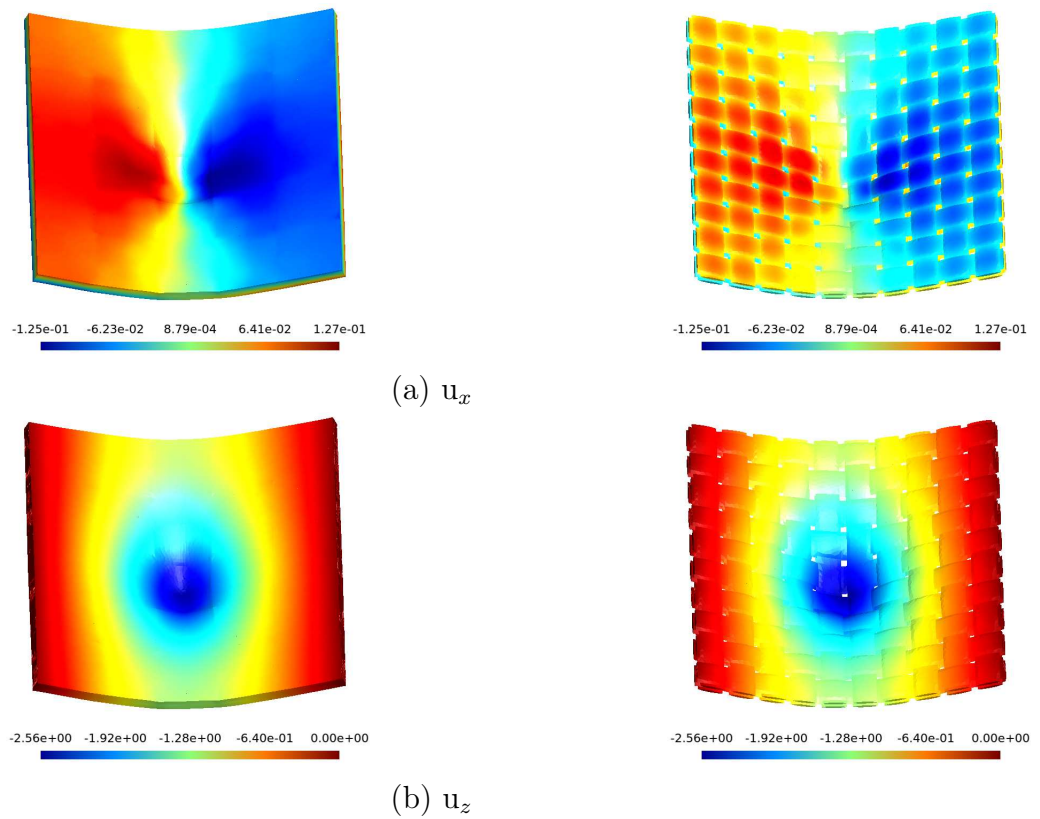


Figure 5.24 – Displacement fields and deformation of a plain weave based composite: full model is shown (left) - only yarn type materials are shown (right).

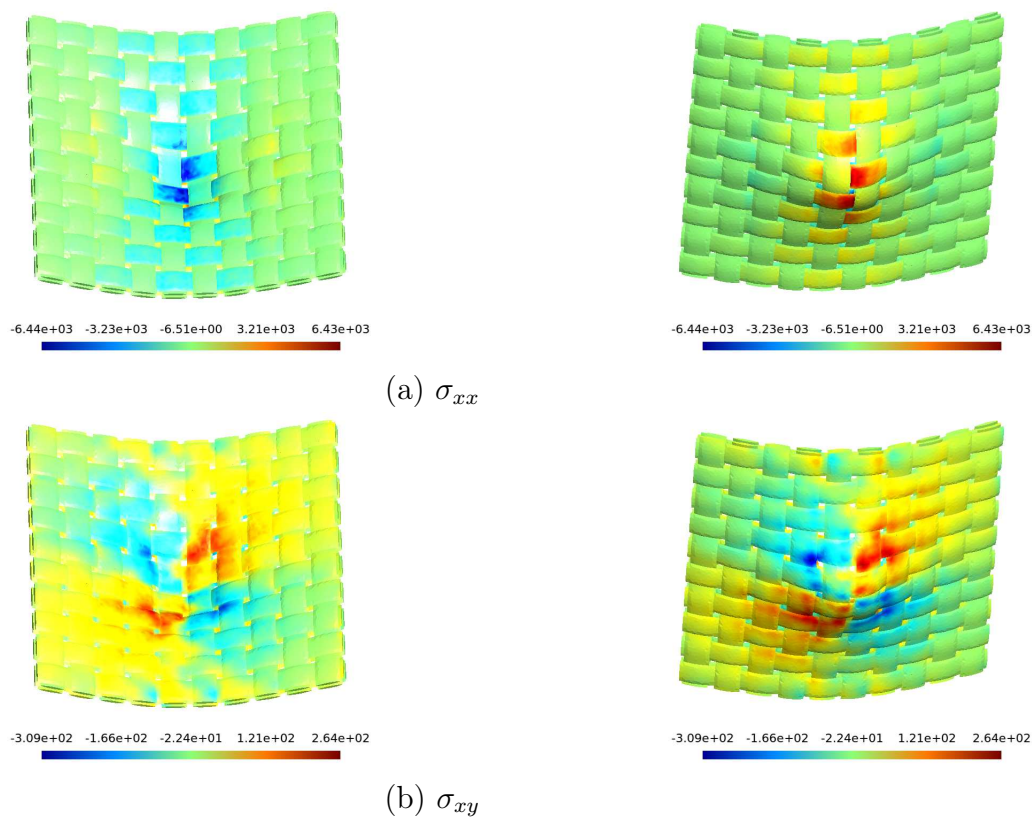


Figure 5.25 – Stress distributions of a plain weave based composite: only yarn type materials are shown. Upper surface (left) - lower surface (right).

Chapter 6

Conclusions and Perspectives

“ A winner is a dreamer who never gives up ”

Nelson Mandela

Contents

6.1	Conclusions	116
6.2	Perspectives	117

6.1 Conclusions

The first chapter of this work is dedicated to the presentation of the PGD. To demonstrate the capacity of this method for reducing the complexity of the model, the PGD have been applied to treat the variability of the composite microstructure. Some uncertain parameters have been added to the problem coordinates: the Young's modulus of each fiber and matrix. With one sole calculation we can get the solution for variable Young's modulus and different number of fibers.

In the second chapters, an approach based on the proper generalized decomposition (PGD) have been proposed to simulate the interfacial delamination under quasi-static loading. This technique coupled with a cohesive zone model (CZM) allows a significant reduction of the computational costs. Three classical failure tests (DCB, ELS, and MMF) have been modeled using PGD and FEM as references. These two methods have been implemented in conjunction with CZM to represent delamination in different fracture modes (two pure modes and a mixed mode). Both two and three dimensional models were developed and analysed. For all failure modes, a close agreement is found between PGD, FEM, and analytical solutions with a proper choice of the main model parameters (mesh density, interface stiffness and fracture toughness). The two methods have been compared with regard to the force versus displacement curves, the damage variable evolution, the interface separation evolution and the stress distributions. It shows that PGD can be used as an alternative to overcome the computational drawbacks of FEM such as the rapid increase in the number of degrees of freedom, the large computational time, and the storage limitation. PGD was found appropriate to capture physical phenomena, which occurs at the interface between layers. Finally, reduction of the number of interface elements was achieved owing to the new PGD-CZM discretization strategy, which minimizes modeling complexity.

This strategy is used in the third chapter for dynamical transient applications. Other types of damages, such as matrix cracking, have been considered. A computationally efficient approach is presented for predicting the impact response of $[90_3/0_3]_s$ cross-ply laminates under a low velocity impact. This was achieved using an implicit Newmark's integration scheme. A bilinear cohesive law was used to model the delamination and crack growth.

In the fourth chapter, we have presented a new multiscale separated representation method to compute the mechanical behavior of composites materials with periodic microstructure. This separated representation involves both the space coordinates of the microscopic scale as well as the space coordinates of the macroscopic scale. For coupling each subdomain, an efficient algorithm is proposed and validated in order to address the numerical challenges mentioned earlier. The performance of the proposed technique has been demonstrated by comparison with a

classical FEM approach. The agreement between the PGD and FEM is excellent. The computational time of the PGD is considerably reduced in comparison to the classical FEM especially when the number of periodic patterns is high.

6.2 Perspectives

There are many perspectives to this work:

- The model described in chapters 2 and 3 accounts only for delamination and localized matrix crack. This is not always sufficient to study complex damage in industrial structures. Therefore, the model should be improved to consider the different damage types and the interaction between them.
- The proposed approach developed in plate structures could be extended to study damage process in shell structures.
- The multiscale approach detailed in chapter 4 could be coupled with damaging models (as for example cohesive zone models) to simulate the failure of composite structures under dynamic loading.
- The convergence of the greedy algorithm used to built the separated representation is not always efficient. The method may be improved by adapting the building strategy to the considered problem. For instance, many terms of the separated representation can be computed at the same time.
- The PGD is well adapted to perform parametric studies as shown in chapter 1. The PGD is then a good candidate to treat variability in composite materials. An approach based on the multiscale model presented in chapter 4 coupled with the parametric model detailed in chapter 1 can be investigated for that purpose.

Résumé substantiel

Représentations séparées pour la simulation multi-échelle du comportement mécanique et de l'endommagement des matériaux composites.

Contexte: matériaux composites

Les matériaux composites sont de plus en plus utilisés dans de nombreuses applications d'ingénierie, notamment l'aérospatiale, l'aéronautique, l'automobile et les équipements de sport pour profiter de leurs bonnes propriétés mécaniques et leur capacité d'économie de poids. Ils ont joué un rôle important dans le développement de structures légères. Les matériaux composites remplacent progressivement les matériaux métalliques traditionnels en raison de leurs propriétés mécaniques spécifiques exceptionnelles ainsi que l'amélioration de la résistance à la corrosion, à la fatigue et de leur prédisposition à une conception sur mesure. Au cours du processus de fabrication, les matériaux composites peuvent être réalisés suivant des formes complexes.

Malgré leurs nombreux avantages, les composites présentent aussi certains inconvénients. Les facteurs environnementaux tels que la température et l'humidité peuvent tous entraîner la dégradation des matériaux. Le comportement des composites est souvent modifié par l'absorption d'humidité. Par ailleurs, la résistance à la température des matériaux composites est très dépendante du choix de la matrice.

Les matériaux composites sont réalisés en associant au moins deux matériaux chimiquement différents (matrice + renfort) dont les propriétés se complètent. Généralement, la tenue en traction d'un composite est assurée par les renforts. Ces derniers ayant une faible résistance en compression, la tenue en compression des composites provient aussi de la matrice. Les matrices les plus employées actuellement dans les matériaux composites sont les résines thermodurcissables,

thermoplastiques ou métalliques. La matrice maintient les fibres dans leur position et leur orientation et assure ainsi le transfert de charges vers les renforts. Elle protège également les fibres contre les agressions extérieures (thermiques, chimiques, chocs,...). Les matériaux de renfort apportent aux composites la tenue mécanique (rigidité et résistance) tout en offrant un gain de masse important vis à vis des matériaux métalliques. Par conséquent, les propriétés mécaniques du composite dépendent principalement du type et de la fraction volumique des fibres. Les différents types de renforts peuvent être classés suivant la nature du matériau qui les constitue (carbone, kevlar, verre, aramide,...) ou leur architecture (unidirectionnels (UD), bidirectionnels (tissés) et multidirectionnels (mat, tissages 3D),...).

Les composites stratifiés sont aujourd'hui largement utilisés dans les applications à hautes performances en raison de leur architecture spécifique. Ils sont constitués d'un empilement de plis unidirectionnels ou tissés en optimisant les directions des renforts en fonction des charges extérieures. Les propriétés mécaniques du stratifié varient en fonction de la séquence d'empilement et l'épaisseur de chaque pli. L'orientation privilégiée de chaque pli permet de maximiser certaines propriétés dans les directions voulues, et donc une conception spécifique pour chaque cas de chargement. Ceci donne au concepteur une certaine souplesse pour adapter la rigidité et la résistance du stratifié afin de satisfaire les exigences structurelles. Les matériaux composites, en particulier les stratifiés unidirectionnels, présentent d'excellentes propriétés mécaniques dans le plan des plis. Cependant, les stratifiés présentent également une faiblesse naturelle dans la direction de l'épaisseur, qui augmente fortement leur sensibilité aux chargements hors-plan, comme l'impact à basse vitesse.

Avec cette méthodologie de conception, l'anisotropie et l'hétérogénéité du matériau sont fortement augmentées. Par conséquent, divers modes d'endommagement peuvent se produire et ont tendance à interagir entre eux. Le processus de ruine dans les structures composites est d'une grande complexité en particulier sous sollicitations dynamiques. La structure particulière d'un stratifié est constituée de trois échelles caractéristiques. On peut en effet distinguer l'échelle microscopique (fibre/matrice), l'échelle mésoscopique (un pli) et l'échelle macroscopique (la structure).

Les endommagements peuvent se produire à ces trois échelles :

- Rupture de fibres, décohésion à l'interface fibre/matrice et microfissuration matricielle à l'échelle microscopique;
- Délaminage à l'échelle mésoscopique;
- Ruine du stratifié à l'échelle macroscopique.

Cette composante multi-échelle est un aspect particulièrement important pour le dimensionnement de structures composites, pour la prédiction et la compréhension

de la cinétique de dégradation. Parmi les différents mécanismes d'endommagement, le délaminage (le décollement ou la décohésion entre les plis du stratifié) est le mode d'endommagement le plus critique pour la structure en terme de tenue mécanique.

Les essais expérimentaux sont un moyen efficace pour évaluer le comportement des composites stratifiés. Cependant, la réponse complexe des stratifiés, le coût élevé des essais mécaniques, ainsi que la difficulté pour obtenir des résultats reproductibles, rendent l'approche expérimentale coûteuse et fastidieuse. Différentes méthodes numériques ont donc été développées afin de remplacer une partie des essais expérimentaux par des "essais virtuels".

Verrous scientifiques et solutions

Le développement de méthodes numériques performantes pour simuler les structures composites est un défi dont les verrous scientifiques sont :

- Les simulations multi-échelles sont très coûteuses en termes de ressources informatiques et de temps de calcul et nécessitent la gestion de grands volumes de données. De nouvelles stratégies numériques doivent être développées afin d'améliorer la performance des simulations multi-échelles;
- La modélisation des phénomènes d'endommagement peut aussi conduire à des difficultés numériques. Le modèle de zone cohésive (MZC) est particulièrement adapté pour étudier le délaminage et la décohésion interface fibre/matrice. Cependant, ce modèle nécessite des discrétisations spatiales et temporelles fines pour garantir la stabilité numérique du modèle;
- Les structures composites ont souvent des géométries de faible épaisseur (plaque ou coque). Dans le cas d'une simulation 3D, un nombre minimum d'éléments est nécessaire dans l'épaisseur pour obtenir une bonne précision, ce qui implique un grand nombre de nœuds;
- Lors de simulations dynamiques, les schémas explicites nécessitent l'utilisation de pas de temps relativement petits. L'intérêt des schémas implicites par rapport aux schémas explicites est qu'il n'y a pas de condition restrictive sur la valeur du pas de temps. Cependant, l'intégration implicite nécessite une opération coûteuse d'inversion de matrice. En utilisant les méthodes implicites, le coût d'un pas de temps est plus important que le coût d'un pas de temps explicite, surtout quand on prend en compte la non-linéarité.

De plus, les outils numériques doivent être robustes, efficaces et validés par l'expérience.

Les simulations des composites sont généralement effectuée dans le cadre de

la méthode des éléments finis (MEF). Il s'agit d'une méthode d'approximation numérique permettant de rechercher une solution approchée d'une équation aux dérivées partielles sur un domaine compact avec certaines conditions imposées. Le principe de base consiste à discrétiser le domaine de résolution en N sous-domaines élémentaires. L'écriture de l'équation différentielle en chaque sous-domaine conduit à un système linéaire qui peut être de très grande dimension suivant la complexité du problème. En pratique, le nombre d'équations algébriques est limité par les ressources informatiques.

Objectifs

Cette thèse a pour objectif de développer des solveurs numériques efficaces permettant de simuler le comportement complexe des composites stratifiés (en lien avec les verrous scientifiques cités ci-dessus), avec une bonne précision tout en conservant des temps de calcul raisonnables. Pour atteindre cet objectif, une nouvelle approche de simulation basée sur une méthode de réduction du modèle appelée PGD (Proper Generalized Decomposition) a été développée. La PGD permet de réduire considérablement le temps de calcul et l'espace mémoire associé à la résolution d'un problème, en particulier lorsque le maillage obtenu implique un grand nombre de degrés de liberté. Cette méthode est basée sur une représentation séparée de la solution. La méthode PGD consiste à construire par enrichissement successif une approximation de la solution sous la forme d'une somme finie de N produits de fonctions où chaque fonction dépend d'une seule variable ou d'un nombre réduit de variables. Ces fonctions ne sont pas connues a priori mais construites à l'aide d'une procédure itérative. La PGD a montré son efficacité dans la résolution de problèmes multidimensionnels et paramétriques.

Deux problèmes principaux sont traités dans cette thèse :

- La modélisation de l'endommagement des composites stratifiés, en particulier le phénomène de délaminage;
- Le développement d'une approche multi-échelle permettant de prendre en compte l'interaction entre les échelles.

Modélisation du délaminage

Le délaminage, qualifié souvent de rupture interlaminaire, est considéré comme un mode d'endommagement critique, puisqu'il réduit considérablement la capacité de la structure à supporter les charges. La rupture interlaminaire des composites stratifiés est due principalement à leur faible résistance interfaciale. Différents types de sollicitations peuvent conduire à l'apparition des délaminages (flexion, impact, ...). Le délaminage favorise l'apparition de flambement local, ce qui entraîne

une réduction de la résistance en compression. Il réduit également la résistance en flexion. C'est pourquoi la bonne prévision des délaminages est souvent nécessaire.

L'implémentation numérique du modèle de zone cohésive dans le cadre de la méthode des éléments finis présente de nombreux problèmes numériques, comme par exemple les problèmes de taille du maillage, pouvant engendrer des problèmes de convergence importants. La nécessité d'une finesse de maillage importante pour la description de l'amorçage et de la propagation de la fissure entraîne très souvent des temps de calcul prohibitifs. Afin de pallier ces différents problèmes numériques, un solveur basé sur la méthode PGD est développé dans le cadre de cette thèse pour modéliser le délaminage dans les composites stratifiés sous sollicitations statiques et dynamiques.

Modélisation Multi-échelle

Pour les approches purement macroscopiques, un modèle simplifié basé sur la théorie des stratifiés peut être utilisé. Dans ce cas, le stratifié est modélisé par un empilement de couches homogènes orthotropes. En réalité, chaque couche n'est pas homogène mais consiste en un renfort fibreux imprégné de résine. Le renfort peut être sous forme unidirectionnel, bidirectionnel (tissu) où avec une orientation aléatoire (mat). L'utilisation de modèles macroscopiques conduit à une perte d'informations microscopiques. De plus, un couplage entre les échelles est souvent observé (l'échelle de la fibre, du pli ou du stratifié). Pour prendre en compte ces couplages un modèle multi-échelle est nécessaire.

La difficulté principale des approches multi-échelles est le développement de méthodes numériques adaptées qui nécessitent souvent de grandes ressources de calcul. Pour prendre en compte les informations microscopiques et pour réduire significativement le coût des approches multi-échelles une nouvelle méthode est proposée. L'idée principale est d'utiliser la périodicité de la microstructure pour séparer deux échelles : l'échelle de la cellule périodique (échelle des fibres ou des torons) de l'échelle macroscopique (échelle de la structure). Cette séparation d'échelles est basée sur une représentation séparée de la solution rendant possible l'utilisation de la PGD.

Déroulement de la thèse

Cette thèse est organisée comme suit :

- Dans le **chapitre 2**, on présente tout d'abord les limites des techniques d'approximation classiquement utilisées pour approcher la solution des problèmes multidimensionnels et paramétriques. Après cela, le principe de la méthode Proper Generalized Decomposition (PGD) pour la construction de

la solution sous forme séparée est introduit brièvement. Enfin, la méthode PGD est détaillée pour des problèmes 2D.

- Dans le **chapitre 3**, nous présenterons de manière non exhaustive un état de l'art sur les approches numériques pour la prédiction des endommagements dans les matériaux composites. Dans un premier temps, l'état de l'art permettra de déterminer parmi les différentes approches numériques existantes, celle qui répond le plus efficacement à notre objectif : la description de l'amorçage et de la propagation du délaminage dans les structures stratifiées. Dans ce contexte, les modèles de zone cohésive (MZC) semblent être a priori l'approche la plus adaptée. Dans un second temps, les différents aspects numériques pour les modèles de zone cohésive et les points essentiels au bon usage de ce type de modèles seront présentés. Les essais de mécanique de la rupture permettant de caractériser la résistance au délaminage sous chargement statique sont rapidement présentés. Une nouvelle approche couplant la PGD et la MZC sera ensuite développée. Pour évaluer l'efficacité d'une telle approche en terme de gain en temps de calcul, une comparaison avec une approche couplée éléments finis (EF)/MZC sera effectuée.
- Dans le **chapitre 4**, Le couplage entre la méthode PGD et le modèle de zone cohésive (MZC) est étendu pour la résolution de l'équation de la dynamique. Ce chapitre s'intéresse particulièrement à la réponse des plaques composites à l'impact faible énergie. Un modèle numérique sera proposé pour prendre en compte la fissuration matricielle et le délaminage par l'utilisation de surfaces cohésives.
- Dans le **chapitre 5**, une revue des principales stratégies de calcul multi-échelle est proposée. Ce chapitre est dédié au développement d'une nouvelle formulation séparée basée sur la méthode PGD en vue de l'appliquer à la résolution des problèmes multi-échelles. L'origine de cette réflexion consiste à utiliser la périodicité de la microstructure pour séparer l'échelle microscopique et l'échelle macroscopique. Enfin, le gain et la robustesse de la méthode proposée par rapport à la méthode des éléments finis sont illustrés au travers d'exemples numériques.

Introduction à la méthode PGD

La simulation numérique des phénomènes non-linéaires, multi-échelles et multi-physiques est un défi qui n'a bien souvent pas encore de solution. Parmi les principales difficultés, ces modèles souffrent de la malédiction de la dimensionnalité (géométries complexes définis dans des espaces de grande dimension, paramétriques à grand nombre de paramètres, ...). En particulier, si on a besoin de multiplier les simulations (cas des problèmes paramétriques, stochastiques

ou d'optimisation), l'utilisation de techniques numériques classiques est limitée par la puissance et le temps de calcul ainsi que par la mémoire des ordinateurs. Pour repousser ces limites et réduire le coût de calcul (temps de calcul, espace de stockage, ...), de nouvelles approches de résolutions sont nécessaires.

Les méthodes de réduction de modèle ("**Reduced Order Modeling**" ou ROM) semblent être des solutions prometteuses pour réduire les coûts de calcul. Elles ont permis la simulation de phénomènes complexes de grande taille jusqu'à présent jamais résolus avec les moyens de calcul classiques.

Ces méthodes de réduction consistent à chercher la solution dans un espace engendré par une base adaptée au problème plutôt que dans l'espace des fonctions de forme éléments finis. Le principe de ces méthodes est donc de remplacer l'espace des fonctions de forme par un sous-espace de plus petite dimension (espace réduit).

Ces méthodes de réduction de modèle sont classées en deux catégories :

- Les méthodes de réduction "**a posteriori**" : où une connaissance préalable sur la solution du problème est nécessaire. La réponse d'un modèle peut être approchée avec une précision raisonnable par la réponse d'un modèle réduit. Ce dernier est obtenu par projection du modèle initial sur une base réduite de fonctions de dimension (n) inférieure à la dimension (N) des modèles numériques fins. Cela revient à résoudre un système d'équations différentielles couplées de taille n (avec $n \ll N$), dont la résolution est très rapide. Parmi les stratégies les plus utilisées actuellement pour la construction de ces bases réduites, nous trouvons la Proper Orthogonal Decomposition (POD) [Lumley, 1967];
- Les méthodes de réduction "**a priori**" : qui ne nécessitent aucune information préalable sur le problème que l'on souhaite simuler. Contrairement aux méthodes a posteriori, les fonctions de base ne sont pas connues a priori mais calculées à l'aide d'une procédure itérative. Ces méthodes permettent d'éviter des calculs préliminaires, assez coûteux en temps. Nous pouvons citer comme méthodes : la méthode PGD (Proper Generalized Decomposition) et la méthode APHR (A Priori Hyper Reduction) [Ryckelynck, 2005].

La méthode APHR [Ryckelynck, 2009] a montré une grande précision dans la simulation des problèmes complexes, accompagnée d'une réduction importante en terme de coût de calcul. Cette méthode n'est pas capable de procéder à une réduction dimensionnelle sur plus de deux sous-espaces ce qui reste une forte contrainte quand le nombre de dimensions est important.

Dans le cadre de ces travaux de thèse, nous nous intéressons à la méthode PGD. La PGD a été développée initialement par P. Ladeveze pour des problèmes espace/temps dans le contexte de la méthode LATIN [Ladeveze and Nouy, 2003];

[Ladeveze et al., 2010]. A. Ammar et al. ont généralisé cette méthode pour des problèmes multidimensionnels [Ammar et al., 2006; Ammar et al., 2007]. La PGD est basée sur une représentation séparée de la solution qui permet de réduire de façon potentiellement importante la taille des problèmes paramétriques et multidimensionnels.

La représentation séparée d'une fonction u quelconque (déplacement, température, vitesse, ...) qui dépend d'un nombre D de coordonnées et/ou paramètres (x_1, \dots, x_D) s'écrit :

$$u(x_1, \dots, x_D) \approx \sum_{i=1}^N F_i^1(x_1) \times \dots \times F_i^D(x_D) \quad (1)$$

Toutes les fonctions (F_i^j) sont inconnues a priori et donc à déterminer.

Cette représentation de la solution est injectée dans la forme faible de l'équation à résoudre. Cette solution est déterminée itérativement avec un algorithme glouton qui consiste à enrichir plusieurs fois l'approximation existante. L'étape d'enrichissement consiste à ajouter un nouveau produit de fonctions à la solution existante. Il s'agit d'un problème non linéaire. Une méthode des directions alternées est généralement utilisée pour linéariser les équations à résoudre.

La séparation des variables d'espace est particulièrement intéressante dans le cas de géométries de type plaque. La PGD est utilisée pour chercher la solution sur la plaque sous la forme d'une somme de produits de fonctions du plan et de fonctions de l'épaisseur. La solution recherchée peut alors s'écrire :

$$\mathbf{u}(x, y, z) \approx \sum_{i=1}^N \mathbf{F}_i(x, y) \circ \mathbf{G}_i(z) \quad (2)$$

où $\mathbf{F}_i(x, y)$ est une fonction vectorielle définie dans le plan et $\mathbf{G}_i(z)$ est une fonction vectorielle définie dans l'épaisseur (Figure 1). Le symbole \circ représente le produit d'Hadamard ou produit composante par composante.

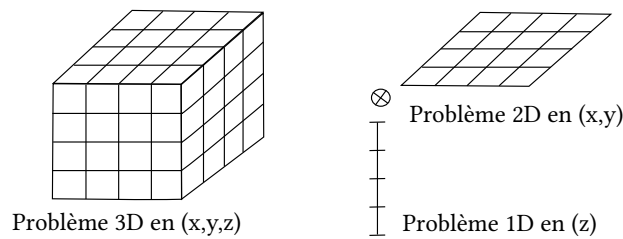


Figure 1 – Séparation d'un problème 3D en 2D/1D.

Avec cette séparation, la solution 3D est obtenue en résolvant uniquement des

problèmes 2D et 1D. Bien que la PGD ait été utilisée avec succès dans un grand nombre de domaines, de nouveaux développements de la méthode restent d'actualité afin de mieux cerner son potentiel mais aussi ses limites.

Simulation du délaminage en statique

Différents modèles ont été développés pour modéliser l'endommagement de composites stratifiés. Certains s'intéressent à l'étude du comportement à une échelle assez fine (fibre/matrice) afin de comprendre les interactions entre les modes de dégradation et leurs influences sur le comportement de la structure. D'autres se concentrent sur le comportement à une échelle intermédiaire et assez grossière (mésomodèle), afin de garder un bon compromis entre la prise en compte des interactions et un coût de calcul raisonnable. Mais le coût de calcul reste généralement élevé dans le cas de problèmes non-linéaires de très grande taille. Pour réduire considérablement le coût de ces techniques, une nouvelle approche basée sur la méthode PGD est développée dans cette thèse.

Un modèle de zone cohésive (MZC) a été choisi pour modéliser l'amorçage des fissures jusqu'à leur propagation. On s'intéresse plus particulièrement à la loi cohésive linéaire par morceaux de Crisfield [[Alfano and Crisfield, 2001](#)]. Ce modèle a été choisi pour décrire et simuler le phénomène de délaminage. Il permet de représenter le comportement d'interface à l'aide d'une loi liant l'effort d'interface à son ouverture, comme le montre la Figure 2.

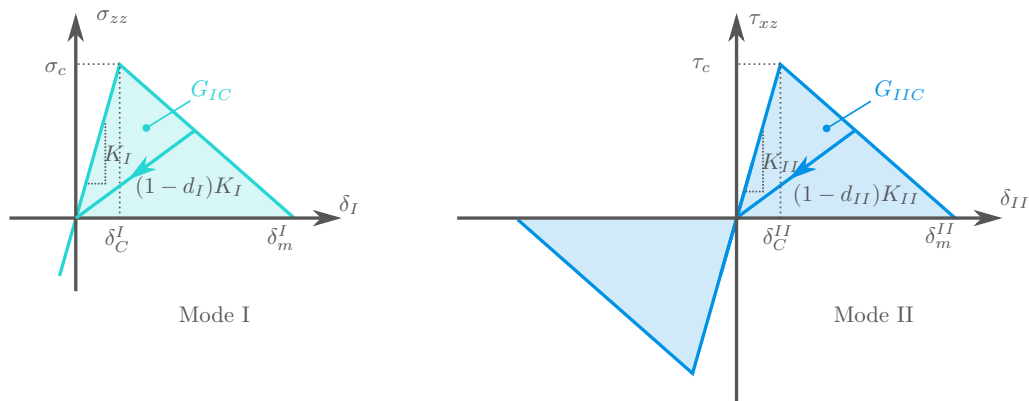


Figure 2 – Loi de comportement linéaire par morceaux pour le modèle cohésif. Traction/compression à gauche, cisaillement à droite.

Dans ces travaux de thèse, on utilise la méthode PGD pour calculer la solution d'un problème 3D complet, tout en gardant un coût de calcul proche de celui d'un calcul 2D. Pour cela, on utilise la capacité de la PGD à calculer des solutions de problèmes

définis sur des géométries de type plaques via une séparation des variables. On choisit donc de séparer les variables d'espace en deux sous espaces : un espace 2D représentant le plan moyen, et un espace 1D représentant l'épaisseur. Ceci conduit à utiliser un maillage 2D et un maillage 1D pour représenter la géométrie, tout en intégrant la possibilité de prendre en compte l'endommagement et en particulier le délaminage. Le couplage entre PGD et MZC se fait à travers l'insertion d'un élément cohésif 1D à l'interface entre deux plis (voir Figure 3). Le problème à

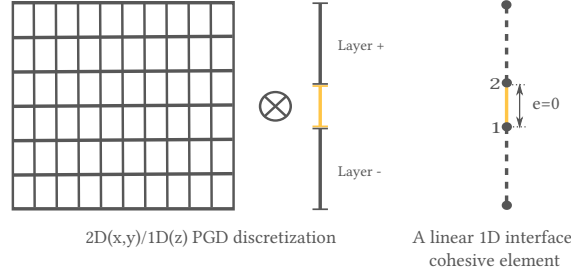


Figure 3 – Maillages 1D et 2D pour la simulation du délaminage.

résoudre est modélisé par l'équation d'équilibre suivante :

$$\nabla \cdot \boldsymbol{\sigma}(\mathbf{u}(x, y, z)) + \mathbf{f} = 0 \quad (3)$$

La loi de comportement élastique s'écrit comme suit :

$$\boldsymbol{\sigma}(\mathbf{u}(x, y, z)) = \mathbb{H}(x, y, z) \cdot \boldsymbol{\varepsilon}(\mathbf{u}(x, y, z)) \quad (4)$$

où $\mathbb{H}(x, y, z)$ est le tenseur d'élasticité, et $\boldsymbol{\varepsilon}(\mathbf{u}(x, y, z))$ est le tenseur de déformation défini par :

$$\boldsymbol{\varepsilon}(\mathbf{u}(x, y, z)) = \frac{1}{2}(\nabla \mathbf{u}(x, y, z) + (\nabla \mathbf{u}(x, y, z))^T) \quad (5)$$

La formulation faible associée à l'équation d'équilibre 3 s'écrit sous la forme suivante

$$\iiint_{\Omega} \boldsymbol{\varepsilon}(\mathbf{u}^*) \cdot (\mathbb{H} \cdot \boldsymbol{\varepsilon}(\mathbf{u})) d\Omega + \underbrace{\iint_{\Gamma_{coh}} \mathbf{T}_{coh} \cdot \boldsymbol{\delta}^* d\Gamma}_{zone\ cohésive} = \iint_{\partial\Omega} \mathbf{T}_{ext} \cdot \mathbf{u}^* d\Gamma \quad (6)$$

On cherchera alors la solution du problème 3D en l'exprimant ainsi :

$$\mathbf{u}(x, y, z) = \sum_{i=1}^N \mathbf{F}_i(x, y) \circ \mathbf{G}_i(z) \quad (7)$$

avec $\mathbf{F}_i(x, y) = \begin{pmatrix} F_u^i(x, y) \\ F_v^i(x, y) \\ F_w^i(x, y) \end{pmatrix}$ est une fonction vectorielle définie dans le plan,

et $\mathbf{G}_i(z) = \begin{pmatrix} G_u^i(z) \\ G_v^i(z) \\ G_w^i(z) \end{pmatrix}$ est une fonction vectorielle définie dans l'épaisseur.

Le problème 3D est représenté comme le produit tensoriel des problèmes 2D et 1D. L'ensemble des quantités du modèle doivent être exprimées sous formes séparées.

Le saut de déplacement à l'interface entre deux plis s'écrit en fonction des composantes du déplacement sous forme séparée :

$$\boldsymbol{\delta} = \begin{pmatrix} \delta_I \\ \delta_{II} \\ \delta_{III} \end{pmatrix} = \begin{pmatrix} \sum_{i=1}^N F_i^w(x, y)(G_i^w(z^+) - G_i^w(z^-)) \\ \sum_{i=1}^N F_i^u(x, y)(G_i^u(z^+) - G_i^u(z^-)) \\ \sum_{i=1}^N F_i^v(x, y)(G_i^v(z^+) - G_i^v(z^-)) \end{pmatrix} \quad (8)$$

L'expression de l'effort cohésif \mathbf{T}_{coh} pour le modèle de zone cohésive est :

$$\mathbf{T}_{coh} = \begin{pmatrix} \sigma_{zz} \\ \tau_{xz} \\ \tau_{yz} \end{pmatrix} = \begin{pmatrix} (1-d)K_I\delta_I \\ (1-d)K_{II}\delta_{II} \\ (1-d)K_{III}\delta_{III} \end{pmatrix} \quad (9)$$

où δ_I (respectivement δ_{II} et δ_{III}) est le saut de déplacement en mode I (respectivement mode II et mode III). K_I (respectivement K_{II} et K_{III}) est la raideur initiale de l'interface en mode I (respectivement mode II et mode III) et d est la variable d'endommagement locale de l'interface.

Pour évaluer l'apport du modèle proposé dans ce travail, la modélisation 3D d'un essai DCB (Double Cantilever Beam) a été mise en place. Les dimensions de la plaque et les conditions aux limites de l'essai sont représentées sur la Figure 4.

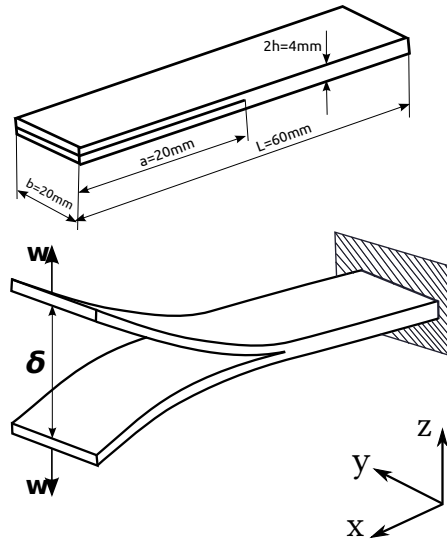


Figure 4 – Représentation schématique des dimensions de l'éprouvette DCB et des conditions aux limites imposées.

L'essai DCB correspond à un essai de traction sur deux bras d'une éprouvette

symétrique pré-fissurée. La pré-fissure permet d'amorcer le délaminage dans des conditions stables. Le matériau étudié est un carbone époxy unidirectionnel. Pour cette modélisation, le comportement du stratifié et le comportement de l'interface sont résumés dans le Tableau 1. La sollicitation en mode I est considérée comme

Propriétés mécaniques du pli		Propriétés de l'interface	
$E_z(MPa)$	11873	$G_{Ic}(N/mm)$ 0.3 ;	$G_{IIc}(N/mm)$ 1.6
$E_x(MPa)$	157380	$\sigma_c(MPa)$ 60 ;	$\tau_c(MPa)$ 139
$G_{xz}(MPa)$	5051	$K_I(N/mm^3)$ 1.10^4 ;	$K_{II}(N/mm^3)$ 5.10^4
ν_{xz}	0.31		

Table 1 – Propriétés mécaniques du pli et propriétés de l'interface.

la plus critique car elle nécessite moins d'énergie pour amorcer une fissure. La Figure 5 présente la distribution du champ de contraintes σ_{xx} . Dans l'objectif

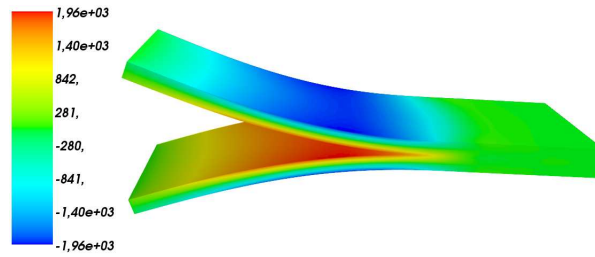


Figure 5 – Représentation du champ de contrainte σ_{xx} .

de connaître l'apport du modèle en termes de temps de calcul, l'essai DCB a été modélisé avec au total 1.8×10^6 degrés de liberté. Dans le cas présenté ici, le temps de calcul est moins de 20 minutes sur un ordinateur portable ce qui n'est pas concevable avec la méthode des éléments finis. Les gains en temps de calcul sont donc intéressants et le sont d'autant plus que le problème est grand.

L'endommagement surfacique à l'interface entre les deux plis est donnée sur la Figure 6.

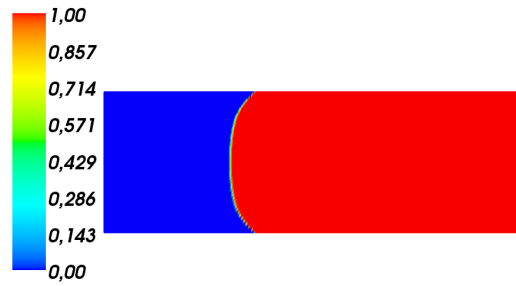


Figure 6 – La variable d’endommagement “d” à l’interface.

Simulation du délaminage en dynamique

Les stratifiés présentent également une faiblesse naturelle dans la direction de l’épaisseur, qui augmente fortement leur sensibilité aux chargements hors-plan, comme l’impact à basse vitesse. Ces impacts peuvent créer des dommages internes sans laisser de marque visible (fissuration de la matrice, délaminage, ...), et par conséquence diminuer leur résistance résiduelle.

L’approche présentée précédemment a été étendue pour modéliser le délaminage des composites stratifiés sous un chargement de type impact. Le problème à résoudre consiste à trouver $\mathbf{u}(x, y, z)$ vérifiant l’équation locale d’équilibre mécanique suivante :

$$\nabla \cdot \boldsymbol{\sigma}(\mathbf{u}(x, y, z)) + \mathbf{f} = \rho \ddot{\mathbf{u}}(x, y, z) \quad (10)$$

avec ρ est la masse volumique.

La forme globale, ou forme faible, s’écrit donc comme suit :

$$\begin{aligned} & \iiint_{\Omega} \boldsymbol{\varepsilon}(\mathbf{u}^*) \cdot (\mathbb{H} \cdot \boldsymbol{\varepsilon}(\mathbf{u}(t))) d\Omega + \underbrace{\iint_{\Gamma_{coh}} \mathbf{T}_{coh} \cdot \boldsymbol{\delta}^*(t) d\Gamma}_{\text{zone cohésive}} \\ & = \iiint_{\Omega} \rho \ddot{\mathbf{u}}(t) \cdot \mathbf{u}^* d\Omega + \iint_{\partial\Omega} \mathbf{T}_{ext} \cdot \mathbf{u}^* d\Gamma \end{aligned} \quad (11)$$

Pour la résolution numérique à chaque pas de temps, une approximation sous forme séparée des champs cinématiques (déplacement, vitesse et accélération) est utilisée :

- Champ de déplacement

$$\mathbf{u}(x, y, z) = \sum_{i=1}^N \mathbf{F}_i(x, y) \circ \mathbf{G}_i(z) \quad (12)$$

- Champ d'accélération

$$\ddot{\mathbf{u}}(x, y, z) = \sum_{i=1}^N \ddot{\mathbf{F}}_i(x, y) \circ \ddot{\mathbf{G}}_i(z) \quad (13)$$

- Champ de vitesse

$$\dot{\mathbf{u}}(x, y, z) = \sum_{i=1}^N \dot{\mathbf{F}}_i(x, y) \circ \dot{\mathbf{G}}_i(z) \quad (14)$$

L'intégration en temps est assurée par un schéma implicite de type Newmark qui est couplé à la PGD. Ce schéma permet d'utiliser un pas de temps indépendant de la taille du plus petit élément du maillage. Afin de valider ce modèle numérique, on considère une plaque constituée de 12 plis de composite carbone/époxy, de dimension $60 \text{ mm} \times 40 \text{ mm} \times 3 \text{ mm}$. Le drapage du stratifié considéré est $[90_3/0_3]_s$. L'impacteur est de type hémisphérique de 12.7 mm de diamètre. La vitesse de l'impacteur est de 5 m/s. Le matériau est considéré comme orthotrope avec les propriétés élastiques présentées au Tableau 1.

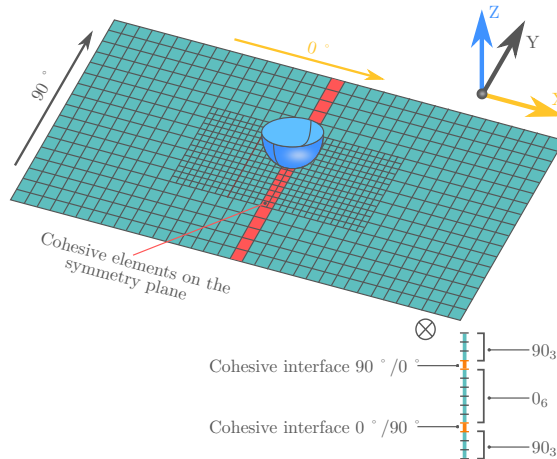
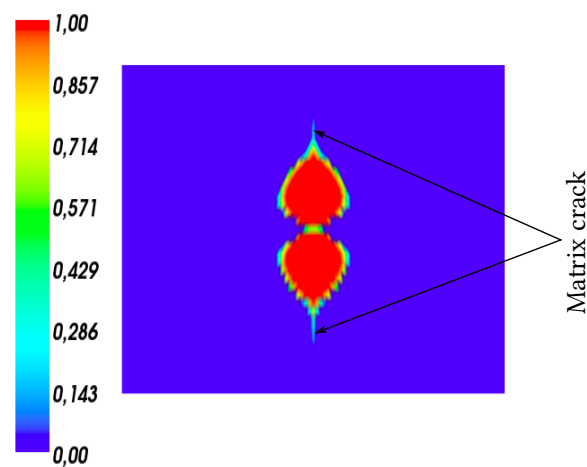


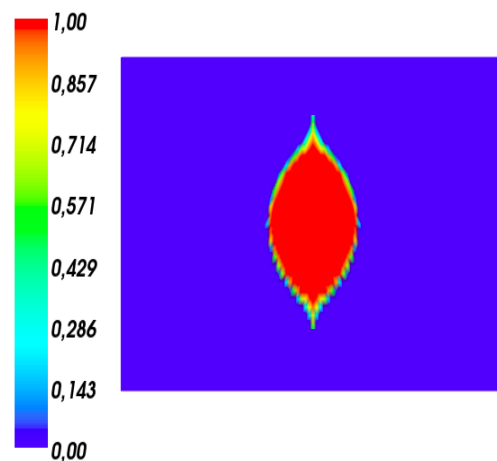
Figure 7 – Localisation des éléments cohésifs.

Chaque pli est représenté séparément avec un élément dans l'épaisseur. Des éléments cohésifs sont disposés aux interfaces entre les plis d'orientations différentes permettant de représenter le délaminage (voir Figure 7). La fissuration de la matrice est la première étape du processus d'endommagement dans les structures composites stratifiées. Sous chargement de type impact, la fissuration matricielle s'amorce assez tôt au cours du chargement dans les plis inférieurs. Avec l'augmentation de la charge, les fissures se multiplient et traversent le pli. Une fois que les fissures transverses atteignent l'interface, le délaminage apparaît et se propage dans l'interface entre deux plis. Les éléments cohésifs pour la fissuration

matricielle sont disposés le long de l'axe de symétrie de la poutre dans la direction des fibres. Ces fissures entraînent l'apparition du délaminage localisé à l'interface inférieure $0^\circ/90^\circ$. Le comportement associé à ces éléments cohésifs est donné par la loi cohésive linéaire par morceaux de Crisfield décrite précédemment. Dans le modèle présenté, la force d'impact est calculée avec la loi non-linéaire de Hertz [Tan and Sun, 1985]. La Figure 8 montre des résultats de calculs utilisant ce modèle. Les résultats numériques du modèle PGD sont comparés à des résultats expérimentaux disponibles dans la littérature [Aymerich et al., 2009]. La PGD donne des résultats en accord avec les résultats expérimentaux, au moins d'un point de vu qualitatif. La PGD a aussi l'avantage d'être un outil de simulation relativement simple peu coûteux à utiliser.



(a) Interface en bas $0^\circ/90^\circ$.



(b) Interface en haut $90^\circ/0^\circ$.

Figure 8 – La variable d'endommagement "d" à l'interface.

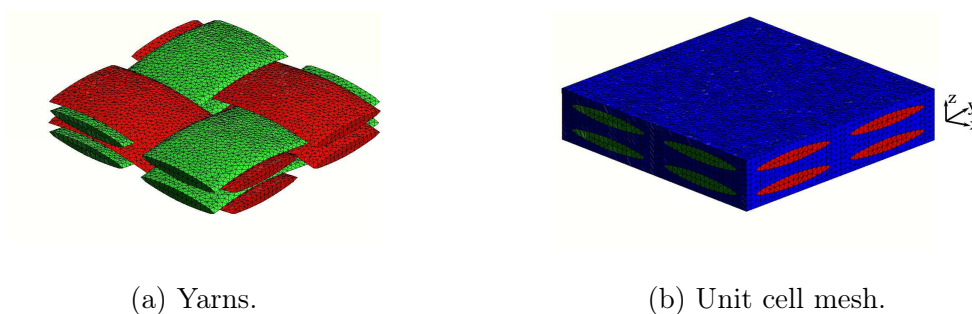
Simulation multi-échelle du comportement mécanique des composites à microstructure périodique

La méthode la plus classique pour traiter les problèmes multi-échelles est de passer par des techniques d'homogénéisation numériques. Ces techniques nécessitent de définir un volume élémentaire représentatif (VER). Le comportement «moyen» du VER est alors estimé et peut être utilisé dans des calculs macroscopiques. Les techniques d'homogénéisation ont été étendues pour des comportements non linéaires dans le cadre de la méthode des éléments finis au carré [Feyel, 1999]. Bien que les méthodes d'homogénéisation soient intéressantes, elles présentent un certain nombre de limites. La première limite est qu'il faut définir des conditions aux limites sur la microstructure. Suivant le choix de ces conditions aux limites, les résultats ne seront pas exactement les mêmes. Une autre limite est que la théorie de l'homogénéisation suppose que les deux échelles (micro et macro) sont bien séparées. Par exemple, une fissure qui apparaît à l'échelle microscopique pour se propager et devenir une fissure macroscopique peut difficilement être représentée par les méthodes d'homogénéisation.

D'autres approches sont basées sur les techniques de décomposition de domaine. L'idée générale est de séparer le domaine d'étude en plusieurs sous-domaines puis d'ajouter des conditions d'interface qui sont modifiées itérativement jusqu'à atteindre la convergence globale. Ces techniques peuvent être utilisées pour des problèmes multi-échelles ou simplement pour réduire le coût des calculs éléments finis classiques. Mais les coûts de calcul restent relativement importants. Pour avoir des calculs plus efficaces, il est nécessaire d'introduire des hypothèses supplémentaires.

Nous nous limitons dans ces travaux de thèse aux matériaux dont la microstructure peut être considérée comme périodique. C'est généralement le cas des matériaux composites. Une représentation séparée de la solution est alors calculée en utilisant une décomposition propre généralisée (PGD : Proper Generalized Decomposition). La démarche proposée nécessite de connaître au préalable une cellule périodique de la structure considérée. Un exemple de cellule périodique pour un composite tissé (taffetas) à deux plis est représenté dans Figure 9. Le maillage de la cellule doit être périodique ce qui peut nécessiter des traitements particuliers pour les bords du maillage.

La position dans la cellule périodique est définie par des coordonnées locales $x = (x, y, z)$. La structure globale étudiée est un assemblage de plusieurs cellules. Un identifiant est associée à chacune de ces cellules. On définit alors une variable k qui décrit l'ensemble des identifiants des cellules. Une représentation



(a) Yarns.

(b) Unit cell mesh.

Figure 9 – Cellule périodique pour un composite tissé à deux plis dans la même direction : représentation des fibres (gauche) et représentation de la matrice (droite).

séparée du déplacement $\underline{u} = (u_x, u_y, u_z)$ peut alors s'écrire :

$$\underline{u}(\underline{x}, k) = \sum_{i=1}^n \underline{F}_i(\underline{x}) \otimes G_i(k) \quad (15)$$

Ici les fonctions \underline{F}_i sont des fonctions vectorielles c'est-à-dire qu'elles comportent trois composantes relatives à u_x , u_y et u_z . Elles sont définies uniquement sur la cellule périodique. Les fonctions G_i sont des fonctions scalaires définies sur l'ensemble des cellules périodiques. Les fonctions \underline{F}_i contiennent les informations liées au comportement mécanique de la microstructure et les fonctions G_i permettent de faire le couplage multi-échelle.

Pour utiliser la méthode PGD, il faut pouvoir construire les opérateurs sous forme séparée. Pour le faire, on effectue un assemblage des opérateurs tel qu'il est fait dans la méthode des éléments finis. On distingue deux types d'éléments :

- Les éléments internes à la cellule. Ce sont les éléments pour lesquels l'ensemble des nœuds appartient à la même cellule microscopique. Pour ces éléments, on construit un opérateur éléments finis classiques pour le maillage local. L'opérateur correspondant au maillage global (décrit par k) est alors une simple matrice identité. Cet opérateur traduit le fait que toutes les cellules contiennent les mêmes éléments internes.
- Les éléments d'interfaces. Ce sont ces éléments qui permettent le couplage entre les différents sous domaines périodiques. Il faut alors construire les opérateurs qui vont faire le couplage entre les cellules et leurs cellules voisines.

Il reste finalement à appliquer des conditions aux limites. Cela peut se faire simplement en utilisant une méthode de pénalisation qui s'avère efficace en pratique.

On considère un problème 2D en déformations planes. Il s'agit d'une plaque encastrée à ses deux extrémités et chargée au centre. Elle est constituée d'un

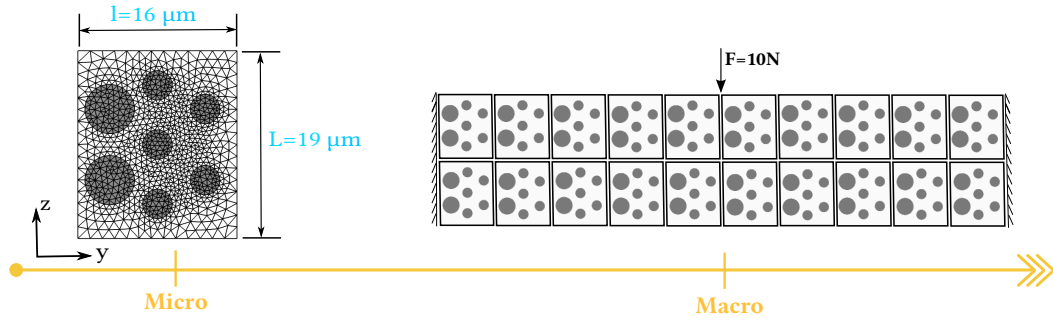


Figure 10 – Géométrie et conditions aux limites du problème considéré.

assemblage de cellules périodiques (voir Figure 10). Le calcul est effectué avec la démarche proposée ci-dessus ainsi qu'avec la méthode des éléments finis en 2D. Lorsque la PGD a convergé, les deux méthodes donnent des résultats rigoureusement identiques. Par exemple, la Figure 11 montre les profils des contraintes σ_{yy} et σ_{yz} au centre de la plaque en fonction de la position dans l'épaisseur (suivant z) et pour les deux méthodes.

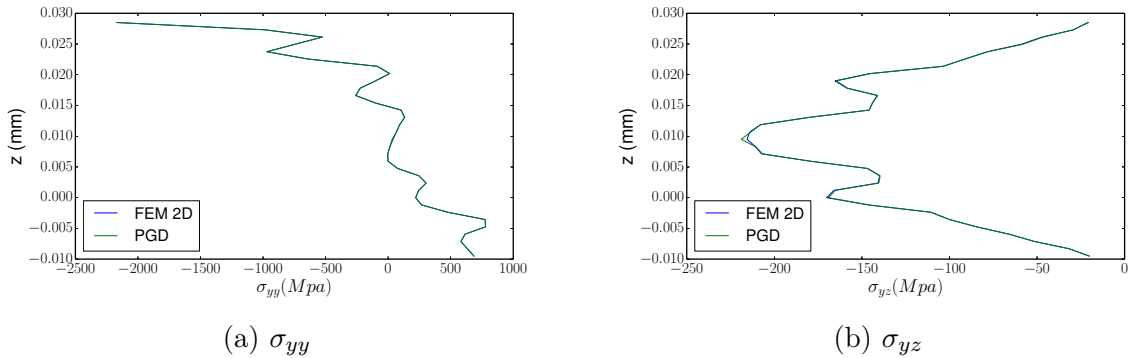


Figure 11 – Profils des contraintes dans l'épaisseur au centre de la plaque.

Un exemple de résultat pour la cellule de la Figure 9 est présenté dans la Figure 12. Il s'agit des contraintes normales σ_{xx} dans une plaque composites simplement appuyée sur ses deux cotés ($x = 0$ et $x = x_{max}$) et chargée en son centre. Seuls les torons sont représentés pour voir les contraintes reprises par les fibres.

Pour un faible nombre de cellules périodiques (inférieur à 20 en 2D), les deux méthodes donnent des temps de calcul assez proches. Par contre, lorsque le nombre de cellules augmente, la démarche proposée devient beaucoup plus performante. Par exemple, pour le cas présenté dans la Figure 10 avec 200 cellules, le temps de calcul est divisé par 10 par rapport aux éléments finis. Et cet écart augmente exponentiellement lorsque le nombre de cellules augmente. Il est ainsi possible de réaliser des calculs multi-échelles en considérant plusieurs dizaines de milliers de

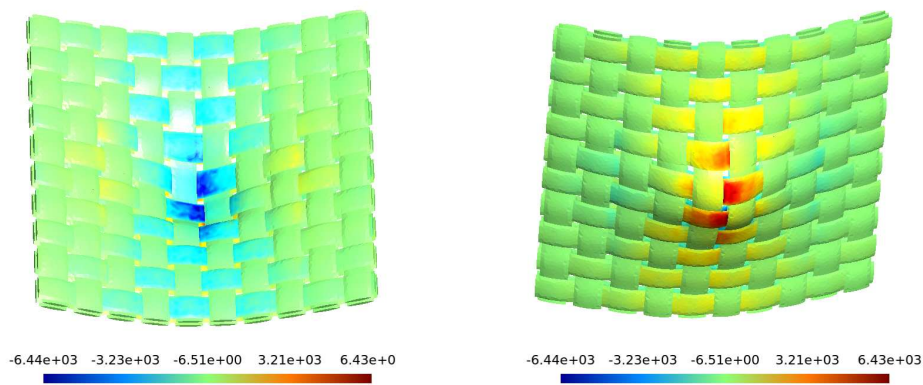


Figure 12 – Contraintes σ_{xx} dans une plaque composite en flexion (vue de dessus et de dessous).

cellules périodiques sur un simple ordinateur portable ce qui n'est absolument pas concevable avec la méthode des éléments finis classiques.

Bibliography

- [Abrate, 1991] Abrate, S. (1991). Impact on laminated composite materials. *Applied Mechanics Reviews*, 44(4):155–190. [65](#)
- [Abrate, 1994] Abrate, S. (1994). Impact on laminated composites : Recent advances. *Applied Mechanics Reviews*, 47:517–544. [68](#)
- [Abrate, 2001] Abrate, S. (2001). Modeling of impacts on composite structures. *Composite Structures*, 51:129–138. [68](#)
- [Airoldi and Dávila, 2012] Airoldi, A. and Dávila, C. G. (2012). Identification of material parameters for modelling delamination in the presence of fibre bridging. *Composite Structures*, 94(11):240–3249. [27](#)
- [Alfano, 2006] Alfano, G. (2006). On the influence of the shape of the interface law on the application of cohesive-zone models. *Composites Science and Technology*, 66(6):723–730. [38](#), [40](#)
- [Alfano and Crisfield, 2001] Alfano, G. and Crisfield, M. A. (2001). Finite element interface models for the delamination analysis of laminated composites: mechanical and computational issues. *International Journal for Numerical Methods in Engineering*, 50(7):1701–1736. [38](#), [43](#), [127](#)
- [Alfredsson and Stigh, 2012] Alfredsson, K. and Stigh, U. (2012). Stability of beam-like fracture mechanics specimens. *Engineering Fracture Mechanics*, 89:98–113. [32](#)
- [Ammar et al., 2012] Ammar, A., Chinesta, F., Cueto, E., and Doblaré, M. (2012). Proper generalized decomposition of time-multiscale models. *International Journal for Numerical Methods in Engineering*, 90(5):569–596. [10](#), [52](#)
- [Ammar et al., 2006] Ammar, A., Mokdad, B., Chinesta, F., and Keunings, R. (2006). A new family of solvers for some classes of multidimensional partial differential equations encountered in kinetic theory modeling of complex fluids. *Journal of Non-Newtonian Fluid Mechanics*, 139(3):153–176. [10](#), [97](#), [126](#)

- [Ammar et al., 2007] Ammar, A., Mokdad, B., Chinesta, F., and Keunings, R. (2007). A new family of solvers for some classes of multidimensional partial differential equations encountered in kinetic theory modelling of complex fluids: Part ii: Transient simulation using space-time separated representations. *Journal of Non-Newtonian Fluid Mechanics*, 144(2-3):98–121. [10](#), [126](#)
- [Anderson, 2005] Anderson, T. L. (2005). *Fracture Mechanics: Fundamentals and Applications*. Third edition: Taylor and Francis. [32](#)
- [ASTM-D5528-01, 2003] ASTM-D5528-01 (2003). Standard test method for mode i interlaminar fracture toughness of unidirectional fiber-reinforced polymer matrix composites. In *Annual Book of ASTM Standards*, volume 15.03. [28](#)
- [ASTM-D5528-94, 1997] ASTM-D5528-94 (1997). Standard test method for mode i interlaminar fracture toughness of unidirectional fibre-reinforced polymer matrix composites. In *Annual Book of ASTM Standards*, volume 15.03. [28](#)
- [Aymerich et al., 2009] Aymerich, F., Dore, F., and Priolo, P. (2009). Simulation of multiple delaminations in impacted cross-ply laminates using a finite element model based on cohesive interface elements. *Composites Science and Technology*, 69(11-12):1699–1709. [74](#), [75](#), [133](#)
- [Babuska, 1976] Babuska, I. (1976). Homogenization approach in engineering, lecture notes in economics and mathematical systems. *Computer Methods in Applied Mechanics and Engineering*, 134:137–153. [84](#)
- [Balzani and Wagner, 2008] Balzani, C. and Wagner, W. (2008). An interface element for the simulation of delamination in unidirectional fiber-reinforced composite laminates. *Engineering Fracture Mechanics*, 75(9):2597–2615. [35](#)
- [Barenblatt, 1962] Barenblatt, G. I. (1962). The mathematical theory of equilibrium cracks in brittle fracture. *Advances in Applied Mechanics*, 7:55–129. [35](#), [36](#), [42](#)
- [Bascom et al., 1980] Bascom, W. D., Bitner, R. J., Moulton, R. J., and Siebert, A. R. (1980). The interlaminar fracture of organic-matrix woven reinforced composites. *Composites*, 11(1):9–18. [28](#)
- [Bensoussan et al., 1978] Bensoussan, A., Lions, J. L., and Papanicolaou, G. C. (1978). In *Asymptotic analysis for periodic structures*, volume 5 of *Studies in Mathematics and Its Applications*. Elsevier. [84](#)
- [Blackman et al., 2006] Blackman, B. R. K., Brunner, A. J., and Williams, J. G. (2006). Mode ii fracture testing of composites: a new look at an old problem. *Engineering Fracture Mechanics*, 73(16):2443–2455. [29](#)

- [Bognet et al., 2012] Bognet, B., Bordeu, F., Chinesta, F., Leygue, A., and Poitou, A. (2012). Advanced simulation of models defined in plate geometries: 3d solutions with 2d computational complexity. *Computer Methods in Applied Mechanics and Engineering*, 201-204:1–12. [10](#)
- [Bolotin, 1996] Bolotin, V. V. (1996). Delaminations in composite structures: Its origin, buckling, growth and stability. *Composites Part B: Engineering*, 27(2):29–145. [25](#)
- [Bolotin, 2001] Bolotin, V. V. (2001). Mechanics of delaminations in laminate composite structures. *Mechanics of Composite Materials*, 37(5-6):367–380. [25](#)
- [Borst et al., 2004] Borst, R. D., Gutierrez, M. A., G. N. Wells, J. J. C. R., , and Askes, H. (2004). Cohesive-zone models, higher-order continuum theories and reliability methods for computational failure analysis. *International Journal for Numerical Methods in Engineering*, 60(1):89–315. [35](#)
- [Brandt, 1977] Brandt, A. (1977). Multi-level adaptive solutions to boundary-value problems. *Mathematics of Computation*, 31:333–390. [92](#)
- [Brandt, 1982] Brandt, A. (1982). Guide to multigrid development. In Hackbush, A. and Trottenberg, U., editors, *Conference on Multigrid Methods*, pages 220–312. [93](#)
- [Camacho and Ortiz, 1996] Camacho, G. T. and Ortiz, M. (1996). Computational modelling of impact damage in brittle materials. *International Journal of Solids and Structures*, 33(20):2899–2938. [36](#)
- [Cantwell and Morton, 1991] Cantwell, W. J. and Morton, J. (1991). The impact resistance of composite materials-a review. *Composites*, 22(5):347–362. [65](#)
- [Chai, 1984] Chai, H. (1984). The characterization of mode i delamination failure in non-woven, multidirectional laminates. *Composites*, 15(4):277–290. [28](#)
- [Chan et al., 1989] Chan, T., Glowinski, R., Periaux, J., and Widlund, O., editors (1989). *Domain Decomposition Methods*, Philadelphia. SIAM. [91](#)
- [Chan and Mathew, 1994] Chan, T. F. and Mathew, T. P. (1994). Domain decomposition algorithms. In *Acta Numerica*, pages 61–143. Cambridge University Press. [91](#)
- [Chandra et al., 2002] Chandra, N., Li, H., Shet, C., and Ghonem, H. (2002). Some issues in the application of cohesive zone models for metal–ceramic interfaces. *International Journal of Solids and Structures*, 39(10):2827–2855. [40](#)
- [Chandra and Shet, 2004] Chandra, N. and Shet, C. (2004). Micromechanistic perspective of cohesive zone approach in modelling fracture. *Computer Modeling in Engineering and Sciences*, 5(1):21–34. [38](#)

- [Chen et al., 1999] Chen, J., Crisfield, M., Kinloch, A. J., Busso, E. P., Matthews, F. L., and Qiu, Y. (1999). Predicting progressive delamination of composite material specimens via interface elements. *Mechanics of Composite Materials and Structures*, 6(4):301–317. [38](#)
- [Chen et al., 2014] Chen, J. F., Morozov, E. V., and Shankar, K. (2014). Simulating progressive failure of composite laminates including in-ply and delamination damage effects. *Composites Part A: Applied Science and Manufacturing*, 61:185–200. [24](#)
- [Cherepanov, 1967] Cherepanov, C. P. (1967). Crack propagation in continuous media. *Journal of Applied Mathematics and Mechanics*, 31:476–488. [33](#)
- [Chinesta et al., 2010a] Chinesta, F., Ammar, A., and Cueto, E. (2010a). On the use of proper generalized decompositions for solving the multidimensional chemical master equation. *European Journal of Computational Mechanics*, 19(1):53–64. [10](#)
- [Chinesta et al., 2010b] Chinesta, F., Ammar, A., and Cueto, E. (2010b). Recent advances and new challenges in the use of the proper generalized decomposition for solving multidimensional models. *Archives of Computational Methods in Engineering*, 17(4):327–350. [10](#)
- [Chinesta et al., 2007] Chinesta, F., Ammar, A., Falco, A., and Laso, M. (2007). On the reduction of stochastic kinetic theory models of complex fluids. *Modelling and Simulation in Materials Science and Engineering*, 15(6):639. [10](#)
- [Choi et al., 1991a] Choi, H., Downs, R., and Chang, F. (1991a). A new approach toward understanding damage mechanisms and mechanics of laminate composites due to low-velocity impact: Part i - experiments. *Journal of Composite Materials*, 25:992–1011. [65](#)
- [Choi et al., 1991b] Choi, H., Downs, R., and Chang, F. (1991b). A new approach toward understanding damage mechanisms and mechanics of laminate composites due to low-velocity impact: Part ii - analysis. *Journal of Composite Materials*, 25:1011–1038. [65](#)
- [Choi and Lim, 2004] Choi, I. H. and Lim, C. H. (2004). Low-velocity impact analysis of composite laminates using linearized contact law. *Composite Structures*, 66(1-4):125–132. [69](#)
- [Christman et al., 1989] Christman, T., Needleman, A., and Suresh, S. (1989). An experimental and numerical study of deformation in metal-ceramic composites. *Acta Metallurgica*, 37(11):3029–3050. [84](#)
- [Cox and Yang, 2006] Cox, B. and Yang, Q. (2006). In quest of virtual tests for structural composites. *Science*, 314(5802):1102–1107. [35](#)

- [Davies, 1992] Davies, P. (1992). Protocols for interlaminar fracture testing of composites. European Structural Integrity Society (ESIS). [28](#), [29](#)
- [Davies, 1998] Davies, P. (1998). Standard test methods for delamination resistance of composite materials: Current status. *Applied Composite Materials*, 5(6):345–364. [28](#)
- [de Moura and de Morais, 2008] de Moura, M. F. S. F. and de Morais, A. B. (2008). Equivalent crack based analyses of enf and els tests. *Engineering Fracture Mechanics*, 75(9):2584–2596. [29](#)
- [Devitt et al., 1980] Devitt, D. F., Schapery, R. A., and Bradley, W. L. (1980). A method for determining the mode i delamination fracture toughness of elastic and viscoelastic composite materials. *Journal of Composite Materials*, 14:270–285. [28](#)
- [Ding, 1999] Ding, W. (1999). *Delamination analysis of composite laminates*. PhD thesis, University of Toronto. [27](#)
- [Dohrmann, 2003] Dohrmann, C. R. (2003). A preconditioner for substructuring based on constrained energy minimization. *SIAM Journal for Scientific Computing*, 25:246–258. [89](#)
- [Dugdale, 1960] Dugdale, D. S. (1960). Yielding of steel sheets containing slits. *Journal of the Mechanics and Physics of Solids*, 8(2):100–104. [35](#), [36](#), [42](#)
- [Eshelby, 1957] Eshelby, J. D. (1957). The determination of the field of an ellipsoidal inclusion and related problems. In *Proceedings of the Royal Society of London*, volume 241 of *series A*, pages 376–396. [84](#)
- [Falk et al., 2001] Falk, M. L., Needleman, A., and Rice, J. R. (2001). A critical evaluation of cohesive zone models of dynamic fracture. *Journal de Physique IV (in press)*, pages 543–550. [42](#), [43](#)
- [Farhat et al., 2000] Farhat, C., Pierson, K., and Lesoine, M. (2000). The second generation feti methods and their application to the parallel solution of large-scale linear and geometracally non-linear structural analysis problems. *Computer Methods in Applied Mechanics and Engineering*, 184:333–374. [89](#)
- [Farhat and Roux, 1991] Farhat, C. and Roux, F. X. (1991). A method of finite element tearing and interconnecting and its parallel solution algorithm. *International Journal for Numerical Methods in Engineering*, 32:1205–1227. [89](#)
- [Feyel, 1999] Feyel, F. (1999). Multiscale fe2 elastoviscoplastic analysis of composite structures. *Computational Materials Science*, 16(1-4):344–354. [84](#), [134](#)

- [Feyel and Chaboche, 2000] Feyel, F. and Chaboche, J. L. (2000). Fe2 multiscale approach for modelling the elastoviscoplastic behaviour of long fibre sic/ti composite materials. *Computer Methods in Applied Mechanics and Engineering*, 183(3-4):309–330. [84](#)
- [Fuoss, 1996] Fuoss, E. (1996). *Effects of stacking sequence on the impact resistance of composite laminates*. PhD thesis, Carleton University - Ottawa Canada. [66](#)
- [Glaessgen et al., 2002] Glaessgen, E. H., Raju, I. S., and Poe, C. C. (2002). Analytical and experimental studies of the debonding of stitched and unstitched composite joints. *Journal of Composite Materials*, 36(23):2599–2622. [27](#)
- [Glaessgen and Hodgkinson, 2000] Glaessgen, P. and Hodgkinson, J. M. (2000). Interlaminar fracture toughness. In Hodgkinson, J., editor, *Mechanical Testing of Advanced Fibre Composites*, pages 170–210. Woodhead Publishing, Cambridge (UK). [27](#)
- [Golub and Ortega, 1993] Golub, G. H. and Ortega, J. M. (1993). *Scientific computing: An introduction with parallel computing*. Academic Press, San Diego. [93](#)
- [Gosselet and Rey, 2006] Gosselet, P. and Rey, C. (2006). Non-overlapping domain decomposition methods in structural mechanics. *Archives of Computational Methods in Engineering*, 13:515–572. [88](#), [90](#)
- [Griffith, 1921] Griffith, A. A. (1921). The phenomena of rupture and flow in solids. *Philosophical Transactions of the Royal Society of London*, 221:163–198. [31](#)
- [Gustafson and Waas, 2009] Gustafson, P. A. and Waas, A. M. (2009). The influence of adhesive constitutive parameters in cohesive zone finite element models of adhesively bonded joints. *International Journal of Solids and Structures*, 46(10):2201–2215. [40](#)
- [Harper and Hallett, 2008] Harper, P. W. and Hallett, S. R. (2008). Cohesive zone length in numerical simulations of composite delamination. *Engineering Fracture Mechanics*, 75(16):4774–4792. [30](#), [43](#)
- [Hashin, 1962] Hashin, Z. (1962). The elastic moduli of heterogeneous materials. *ASME Journal for Applied Mechanics*, 29:143–150. [84](#)
- [Hill, 1965] Hill, R. (1965). A self-consistent mechanics of composite materials. *Journal of the Mechanics and Physics of Solids*, 13:213–222. [84](#)

- [Hillerborg et al., 1976] Hillerborg, A., Mod er, M., and Petersson, P. E. (1976). Analysis of crack formation and crack growth in concrete by means of fracture mechanics and finite elements. *Cement and Concrete Research*, 6(6):773–781. [42](#)
- [Huang and Hull, 1989] Huang, X. N. and Hull, D. (1989). Effects of fibre bridging on {GIC} of a unidirectional glass/epoxy composite. *Composites Science and Technology*, 35(3):283–299. [27](#)
- [Hui et al., 2003] Hui, C. Y., Jagota, A., Bennison, S. J., and Londono, J. D. (2003). Crack blunting and the strength of soft elastic solids. In *Proceedings of the Royal Society of London*, volume 459 of *series A*, pages 1489–1516. [42](#)
- [Irwin, 1958] Irwin, G. R. (1958). Fracture. In Fl gge, S., editor, *Elasticity and Plasticity / Elastizit t und Plastizit t*, volume 3-6 of *Handbuch der Physik / Encyclopedia of Physics*, pages 551–590. Springer Berlin Heidelberg. [33](#)
- [Irwin, 1960] Irwin, G. R. (1960). Plastic zone near a crack and fracture toughness. In *The Seventh Sagamore Ordnance Materials Conference*. [42](#)
- [Jensen and Sheinman, 2001] Jensen, H. M. and Sheinman, I. (2001). Straight-sided, buckling-driven delamination of thin films at high stress levels. *International Journal of Fracture*, 110(4):371–385. [27](#)
- [Jimack, 2007] Jimack, P. K. (2007). Applications of multigrid techniques in cfd. *International Journal for Numerical Methods in Fluids*, pages 1–12. [93](#)
- [Joffe, 1999] Joffe, R. (1999). *Damage accumulation and stiffness degradation in composite laminates*. PhD thesis, Lulea University of Technology. [24](#)
- [Joshi and Sun, 1987a] Joshi, S. P. and Sun, C. T. (1987a). Impact-induced fracture in a quasi-isotropic laminate. *Journal of Composite Technology and Research*, 9(2):40–46. [65](#)
- [Joshi and Sun, 1987b] Joshi, S. P. and Sun, C. T. (1987b). Impact-induced fracture initiation and detailed dynamic stress field in the vicinity of impact. In *American Society of Composites 2nd Tech. Conf.*, pages 177–185. [65](#)
- [Krueger, 2004] Krueger, R. (2004). Virtual crack closure technique: History, approach, and applications. *Applied Mechanics Reviews*, 57:109–143. [33](#)
- [Kurnatowski and Matzenmiller, 2012] Kurnatowski, B. and Matzenmiller, A. (2012). Coupled twoscale analysis of fiber reinforced composite structures with microscopic damage evolution. *International Journal of Solids and Structures*, 49:2404–2417. [24](#)

- [Ladeveze and Nouy, 2003] Ladeveze, P. and Nouy, A. (2003). On a multiscale computational strategy with time and space homogenization for structural mechanics. *Computer Methods in Applied Mechanics and Engineering*, 192(28-30):3061–3087. [10](#), [126](#)
- [Ladeveze et al., 2010] Ladeveze, P., Passieux, J., and Neron, D. (2010). The latin multiscale computational method and the proper generalized decomposition. *Computer Methods in Applied Mechanics and Engineering*, 199(21-22):1287–1296. [10](#), [126](#)
- [Lagunegrand et al., 2006] Lagunegrand, L., Lorriot, T., Harry, R., and an J. M. Quenisset, H. W. (2006). Initiation of free-edge delamination in composite laminates. *Composites Science and Technology*, 66:1315–1327. [25](#)
- [Lee, 1982] Lee, J. D. (1982). Three dimensional finite element analysis of damage accumulation of composite laminate. *Computers and Structures*, 15(3):335–350. [24](#)
- [Lee et al., 2010] Lee, M. J., Cho, T. M., Kim, W. S., Lee, B. C., and Lee, J. J. (2010). Determination of cohesive parameters for a mixed-mode cohesive zone model. *International Journal of Adhesion and Adhesives*, 30(5):322–328. [40](#)
- [Li et al., 2014] Li, D. H., Liu, Y., and Zhang, X. (2014). Low-velocity impact responses of the stiffened composite laminated plates based on the progressive failure model and the layerwise/solid-elements method. *Composite Structures*, 110:249–275. [69](#)
- [Lin and Lee, 1990] Lin, H. and Lee, Y. (1990). Impact-induced fracture in laminated plates and shells. *Journal of Composite Materials*, 24:1179–1199. [66](#)
- [Lions, 1988] Lions, P. (1988). On the schwarz alternating method. i. In *First International Symposium on Domain Decomposition Methods for Partial Differential Equations*, pages 1–42. [88](#)
- [Lions, 1989] Lions, P. L. (1989). On the schwarz alternating method. ii. In *Domain decomposition methods*, pages 47–70. [88](#)
- [Liu and Malvem, 1987] Liu, D. and Malvem, L. E. (1987). Matrix cracking in impacted glass/epoxy plates. *Journal of Composite Materials*, 21:594–609. [65](#)
- [Lorriot et al., 2003] Lorriot, T., Marion, G., Harry, R., and Wargnier, H. (2003). Onset of free-edge delamination in composite laminates under tensile loading. *Composites Part B: Engineering*, 34:459–471. [25](#)
- [Lumley, 1967] Lumley, J. (1967). The structure of inhomogeneous turbulence. pages 166–178. [9](#), [125](#)

- [Majeed, 1995] Majeed, O. (1995). *Numerical modelling of transverse impact on composite coupons*. PhD thesis, Carleton University - Ottawa Canada. 66
- [Mandel, 1993] Mandel, J. (1993). Balancing domain decomposition. *Communications in Numerical Methods in Engineering*, 9:233–241. 89
- [McCartney, 1998] McCartney, L. N. (1998). Predicting transverse crack formation in cross-ply laminates. *Composites Science and Technology*, 58:1069–1081. 25
- [Mi et al., 1998] Mi, U., Crisfield, M., and Davies, G. (1998). Progressive delamination using interface elements. *Journal of Composite Materials*, 32:1246–1272. 43
- [Moës and Belytschko, 2002] Moës, N. and Belytschko, T. (2002). Extended finite element method for cohesive crack growth. *Engineering Fracture Mechanics*, 69:813–833. 43
- [Mori and Tanaka, 1973] Mori, T. and Tanaka, K. (1973). Average stress in the matrix and average elastic energy of materials with misfitting inclusions. *Acta Metallurgica*, 21:571–574. 84
- [Needleman, 1987] Needleman, A. (1987). A continuum model for void nucleation by inclusion debonding. *Journal of Applied Mechanics*, 54(3):525–531. 36
- [Needleman, 2014] Needleman, A. (2014). Some issues in cohesive surface modelling. In *23rd International Congress of Theoretical and Applied Mechanics*. 40
- [Newmark, 1959] Newmark, N. M. (1959). A method of computation for structural dynamics. *Journal of the Engineering Mechanics Division*, 85(EM3). 70
- [Nouy, 2008] Nouy, A. (2008). Generalized spectral decomposition method for solving stochastic finite element equations: Invariant subspace problem and dedicated algorithms. *Computer Methods in Applied Mechanics and Engineering*, 197(51-52):4718–4736. 10
- [Nouy and Maitre, 2009] Nouy, A. and Maitre, O. P. L. (2009). Generalized spectral decomposition for stochastic nonlinear problems. *Journal of Computational Physics*, 228(1):202–235. 10
- [Ochoa and Engblom, 1987] Ochoa, O. O. and Engblom, J. J. (1987). Analysis of progressive failure in composites. *Composites Science and Technology*, 28:87–102. 24
- [Olsson, 1999] Olsson, R. (1999). Impact and damage tolerance of composites – status and future work at ffa. The Aeronautical Research Institute of Sweden, Bromma. 68

- [Olsson, 2001] Olsson, R. (2001). Analytical prediction of large mass impact damage in composite laminates. *Composites Part A: Applied Science and Manufacturing*, 32(9):1207–1215. [68](#)
- [Olsson, 2003] Olsson, R. (2003). Closed form prediction of peak load and delamination onset under small mass impact. *Composite Structures*, 59(3):341–349. [68](#)
- [Olsson et al., 2006] Olsson, R., Donadon, M. V., and Falzon, B. G. (2006). Delamination threshold load for dynamic impact on plates. *International Journal of Solids and Structures*, 43:3124–3141. [68](#)
- [P. W. Harper and Hallet, 2012] P. W. Harper, L. S. and Hallet, S. R. (2012). A study on the influence of cohesive zone interface element strength parameters on mixed mode behaviour. *Composites Part A: Applied Science and Manufacturing*, 43(4):722–734. [40](#)
- [Pagano and Schoeppner, 2000] Pagano, N. J. and Schoeppner, G. A. (2000). *Delamination of Polymer Matrix Composites: Problems and Assessment*. Pergamon. [25](#)
- [Pavliotis and Stuart, 2008] Pavliotis, G. A. and Stuart, A. M. (2008). In *Multiscale methods: averaging and homogenization*, volume 53 of *Texts in Applied Mathematics*. Springer. [84](#)
- [Pineau and Dau, 2012] Pineau, P. and Dau, F. (2012). Subsampling and homogenization to investigate variability of composite material mechanical properties. *Computer Methods in Applied Mechanics and Engineering*, 241-244:238–245. [84](#)
- [Poon and N. Bellinger, 1993] Poon, C. and N. Bellinger, Y. Xiong, R. G. (1993). Edge delamination of composite laminates. In *The 9th International Conference on Composite Materials*, pages 12.1–12.13. [66](#)
- [Pruliere, 2014] Pruliere, E. (2014). 3d simulation of laminated shell structures using the proper generalized decomposition. *Composite Structures*, 117:373–381. [10](#)
- [Pruliere et al., 2010a] Pruliere, E., Chinesta, F., and Ammar, A. (2010a). On the deterministic solution of multidimensional parametric models using the proper generalized decomposition. *Mathematics and Computers in Simulation*, 81(4):791–810. [10](#), [100](#)
- [Pruliere et al., 2010b] Pruliere, E., Ferec, J., Chinesta, F., and Ammar, A. (2010b). An efficient reduced simulation of residual stresses in composite forming processes. *International Journal of Material Forming*, 3(2):1339–1350. [10](#)

- [Quarteroni and Valli, 1999] Quarteroni, A. and Valli, A. (1999). Domain decomposition methods for partial differential equations. Oxford University Press. [91](#)
- [Rice, 1980] Rice, J. (1980). The mechanics of earthquake rupture. In Dziewonski, A. M. and Boschi, E., editors, *Physics of the Earth's Interior*, volume 3-6 of *Proc. International School of Physics "Enrico Fermi", Course 78, 1979*, pages 555–649. Italian Physical Society and North-Holland Publ. Co. [42](#)
- [Rice, 1968] Rice, J. R. (1968). A path independent integral and the approximate analysis of strain concentration by notches and cracks. *Journal of applied mechanics*, 35:379–386. [32](#), [33](#)
- [Richardson and Wisheart, 1996] Richardson, M. . W. and Wisheart, M. J. (1996). Review of low-velocity impact properties of composite materials. *Composites Part A*, 27:1123–1131. [64](#)
- [Roy and Chakraborty, 2008] Roy, T. and Chakraborty, D. (2008). Delamination in {FRP} laminates with holes under transverse impact. *Materials and Design*, 29(1):124–132. [69](#)
- [Rybicki and Kanninen, 1977] Rybicki, E. F. and Kanninen, M. F. (1977). A finite element calculation of stress intensity factors by a modified crack closure integral. *Engineering Fracture Mechanics*, 9(4):931–938. [33](#)
- [Ryckelynck, 2005] Ryckelynck, D. (2005). A priori hyperreduction method : an adaptive approach. *Journal of Computational Physics*, 202:346–366. [9](#), [125](#)
- [Ryckelynck, 2009] Ryckelynck, D. (2009). Hyper reduction of mechanical models involving internal variables. *International Journal for Numerical Methods in Engineering*, 77(1):75–89. [9](#), [125](#)
- [Schwarz, 1870] Schwarz, H. A. (1870). Über einen grenzübergang durch alternierendes verfahren. In *Vierteljahrsschrift der Naturforschenden Gesellschaft in Zürich 15*, pages 272–286. [87](#)
- [Shivakumar et al., 1985] Shivakumar, K. N., Elber, W., and Illg, W. (1985). Prediction of low-velocity impact damage in thin circular laminate. *AIAA Journal*, 23(3):442–449. [65](#)
- [Shivakumar et al., 1988] Shivakumar, K. N., Tan, P. W., and Newman, J. C. (1988). A virtual crack-closure technique for calculating stress intensity factors for cracked three dimensional bodies. *International Journal of Fracture*, 36:R43–R50. [33](#)

- [Sills and Thouless, 2013] Sills, R. B. and Thouless, M. D. (2013). The effect of cohesive-law parameters on mixed-mode fracture. *Engineering Fracture Mechanics*, 109:353–368. [40](#)
- [Sjöblom et al., 1988] Sjöblom, P. O., Hartness, J. T., and Cordell, T. M. (1988). On low-velocity impact testing of composite materials. *Journal of Composite Materials*, 22:30–52. [65](#)
- [Sluis et al., 1999] Sluis, O. V. D., Schreurs, P. J. G., and Meijer, H. E. H. (1999). Effective properties of a viscoplastic constitutive model obtained by homogenisation. *Mechanics of Materials*, 31(11):743–759. [84](#)
- [Smith et al., 1996] Smith, B. F., Bjorstad, P. E., and Gropp, W. (1996). Domain decomposition: parallel multilevel methods for elliptic partial differential equations. Cambridge University Press. [91](#)
- [Song et al., 2008] Song, K., Davila, C. G., and Rose, C. A. (2008). Guidelines and parameter selection for the simulation of progressive delamination. In *ABAQUS User’s Conference*. [41](#), [43](#), [44](#)
- [Stolz, 2010] Stolz, C. (2010). On micro-macro transition in non-linear mechanics. *Materials*, 3(1):296–317. [82](#)
- [Tallec, 1994] Tallec, P. L. (1994). Domain decomposition methods in computational mechanics. In *Computational Mechanics Advances*, 1. [89](#)
- [Tamuzs et al., 2001] Tamuzs, V., Tarasovs, S., and Vilks, U. (2001). Progressive delamination and fiber bridging modeling in double cantilever beam composite specimens. *Engineering Fracture Mechanics*, 68(5):513–525. [27](#)
- [Tan and Sun, 1985] Tan, T. M. and Sun, C. T. (1985). Use of statical indentation law in the impact analysis of laminated composite plates. *Journal of Composite Materials*, 52:6–12. [69](#), [71](#), [133](#)
- [Tartar, 2009] Tartar, L. (2009). In *The general theory of homogenization: a personalized introduction*, volume 7 of *Lecture Notes of the Unione Matematica Italiana*. Springer. [84](#)
- [Tàvara et al., 2013] Tàvara, L., Mantič, V., Salvadori, A., Gray, L. J., and París, F. (2013). Cohesive-zone-model formulation and implementation using the symmetric galerkin boundary element method for homogeneous solids. *Computational Mechanics*, 51(4):535–551. [54](#)
- [Tay and Shen, 2002] Tay, T. E. and Shen, F. (2002). Analysis of delamination growth in laminated composites with consideration for residual thermal stress effects. *Journal of Composite Materials*, 36(11):1299–1320. [25](#)

- [Tenchev and Falzon, 2006] Tenchev, R. T. and Falzon, B. G. (2006). A pseudo-transient solution strategy for the analysis of delamination by means of interface elements. *Finite Elements in Analysis and Design*, 42(8-9):698–708. [35](#)
- [Troussset, 2013] Troussset, E. (2013). *Prévision des dommages d'impact basse vitesse et basse énergie dans les composites à matrice organique stratifiés*. PhD thesis, École Nationale Supérieure d'Arts et Métiers - Centre d'Angers. [68](#)
- [Turon, 2007] Turon, A. (2007). *Simulation of delamination in composites under quasi-static and fatigue loading using cohesive zone models*. PhD thesis, University of Girona. [42](#), [43](#)
- [Turon et al., 2010] Turon, A., Camanho, P. P., Costa, J., and Renart, J. (2010). Accurate simulation of delamination growth under mixed-mode loading using cohesive elements: Definition of interlaminar strengths and elastic stiffness. *Composite Structures*, 92(8):1857–1864. [51](#)
- [Turon et al., 2005] Turon, A., Davila, C. G., Camanho, P. P., and Costa, J. (2005). An engineering solution for using coarse meshes in the simulation of delamination with cohesive zone models. *NASA Technical Memorandum*. [41](#), [42](#), [43](#), [51](#), [53](#)
- [Tvergaard, 1990] Tvergaard, V. (1990). Analysis of tensile properties for a whisker-reinforced metal-matrix composite. *Acta Metallurgica*, 38(2):185–194. [84](#)
- [Tvergaard and Hutchinson, 1992] Tvergaard, V. and Hutchinson, J. W. (1992). The relation between crack growth resistance and fracture process parameters in elastic-plastic solids. *Journal of the Mechanics and Physics of Solids*, 40(6):1377–1397. [36](#)
- [Valoroso et al., 2013] Valoroso, N., Sessa, S., Lepore, M., and Cricri, G. (2013). Identification of mode-I cohesive parameters for bonded interfaces based on dcB test. *Engineering Fracture Mechanics*, 104:56–79. [28](#)
- [Vandellos et al., 2009] Vandellos, T., Carrere, N., and Huchette, C. (2009). Development of computational strategy to model delamination in composite structures. In *Comptes Rendus des JNC 16*, Toulouse. [51](#)
- [Vidal et al., 2012] Vidal, P., Gallimard, L., and Polit, O. (2012). Composite beam finite element based on the proper generalized decomposition. *Computers and Structures*, 102-103:76–86. [10](#)
- [Vidal et al., 2013] Vidal, P., Gallimard, L., and Polit, O. (2013). Proper generalized decomposition and layer-wise approach for the modeling of composite plate structures. *International Journal of Solids and Structures*, 50(14-15):2239–2250. [10](#)

- [Volokh, 2004] Volokh, K. Y. (2004). Comparison between cohesive zone models. *Journal of Communications in Numerical Methods and Engineering*, 20:845–856. 38
- [Weinan, 2011] Weinan, E. (2011). *Principles of Multiscale Modeling*. Cambridge University Press. 81
- [Whitney et al., 1982] Whitney, J. M., Browning, C. E., and Hoogsteden, W. (1982). A double cantilever beam test for characterizing mode I delamination of composite materials. *Journal of Reinforced Plastics and Composites*, 1:297–330. 28
- [Wisnom, 2010] Wisnom, M. R. (2010). Modelling discrete failure in composites with interface elements. *Composites Part A: Applied Science and Manufacturing*, 11(7):795–805. 40
- [Xu and Needleman, 1994] Xu, X. P. and Needleman, A. (1994). Numerical simulation of fast crack growth in brittle solids. *Journal of the Mechanics and Physics of Solids*, 42(9):1397–1434. 36
- [Yang, 1999] Yang, J. (1999). *Development about composite homogenization in static and in dynamic - application to UD composite materials*. PhD thesis, l’Institut de Recherche en Génie Civil et Mécanique - Ecole Centrale de Nantes. 84
- [Yigit and Christoforou, 1995] Yigit, A. S. and Christoforou, A. P. (1995). Impact dynamics of composite beams. *Composite Structures*, 32:187–195. 69
- [Yigit and Christoforou, 1998] Yigit, A. S. and Christoforou, A. P. (1998). Characterization of impact in composite plates. *Composite Structures*, 43:15–24. 69
- [Zou et al., 2001] Zou, Z., Reid, S. R., Li, S., and Soden, P. D. (2004/2001). Mode separation of energy release rate for delamination in composite laminates using sublaminates. *International Journal of Solids and Structures*, 38:2597–2613. 34
- [Zubillaga et al., 2015] Zubillaga, L., Turon, A., Renart, J., Costa, J., and Linde, P. (2015). An experimental study on matrix crack induced delamination in composite laminates. *Composite Structures*, 127:10–17. 25

List of Figures

2.1	Problem definition.	11
2.2	2D problem separated into two decoupled 1D problems.	13
2.3	Algorithm of solution by PGD strategy.	17
2.4	Problem geometry and boundary conditions.	18
2.5	PGD parametric solution for $E_m = 3.8$, $E_{f1} = 228.92$, $E_{f2} = 221.48$, $E_{f3} = 246.9$, $E_{f4} = 237.6$, $E_{f5} = 223.65$, $E_{f6} = 242.25$, $E_{f7} = 225.51$, $E_{f8} = 234.5$, $E_{f9} = 250$ (GPa).	20
2.6	PGD parametric solution for $E_m = 3$, $E_{f1} = 220.554$, $E_{f2} = 225.89$, $E_{f3} = 240.7$, $E_{f4} = 228.61$, $E_{f5} = 249.07$, $E_{f6} = 236.05$, $E_{f7} = 246.59$, $E_{f8} = 232.95$, $E_{f9} = 3$ (GPa).	21
3.1	Illustration of the major failure modes in composite laminates.	24
3.2	Damage modes in unidirectional carbon/epoxy composite.	25
3.3	Fracture crack separation modes.	26
3.4	Schematic of fiber bridging.	28
3.5	Double cantilever beam specimen.	29
3.6	End load split specimen.	30
3.7	Mixed mode end load split specimen.	30
3.8	J-integral contour path enclosing the crack tip.	33
3.9	VCCT for 2D 4-node element.	34
3.10	Schematic illustration of fracture process zone.	35
3.11	Principle of cohesive crack models.	36
3.12	Linear softening: (a) with initial slope, (b) without initial slope.	38
3.13	Cohesive law for the mode I and mode II.	39
3.14	Cohesive law for the mixed mode.	41
3.15	Definition of cohesive surfaces.	45
3.16	Specimen dimensions.	51
3.17	Implementation of mixed boundary conditions in PGD. E_x is the longitudinal elastic modulus, the new elements (in colors) are incorporated at the surface where mixed boundary conditions are imposed.	52

3.18	Functions \mathbf{F}_i and \mathbf{G}_i in the separated representation of the displacement field.	53
3.19	Force vs. displacement curves.	54
3.20	Damage variable evolution along the crack path for an imposed displacement: (a) DCB test, (b) ELS test and (c) MMELS test.	55
3.21	Crack tip in the case of DCB test.	55
3.22	Interface separations evolution along the crack path: (a) DCB test, (b) ELS test and (c) MMELS test.	56
3.23	The normal stress distributions in the longitudinal and thickness direction for the DCB specimen: (a) Stress σ_{xx} , (b) Stress σ_{zz}	57
3.24	The distribution of normal and shear stresses for the ELS specimen: (a) Stress σ_{xx} , (b) Stress σ_{xz}	57
3.25	The distribution of normal and shear stresses for the MMELS specimen: (a) Stress σ_{xx} , (b) Stress σ_{zz} and (c) Stress σ_{xz}	58
3.26	Normal cohesive stresses vs. position for different load stages of DCB test.	58
3.27	Tangential cohesive stresses vs. position for different load stages of ELS test.	58
3.28	2D/1D PGD discretization.	59
3.29	Functions F_w^i and G_w^i in the separated representation of the displacement field: (a) $i=1$, (b) $i=2$	59
3.30	The σ_{xx} stress distribution for the 3D DCB specimen.	60
3.31	Crack surfaces of 3D DCB test: (a) iteration 3, (b) iteration 5, (c) iteration 40 and (d) final iteration.	61
4.1	Typical matrix cracking and delamination damage in a [0/90/0] UD laminated composite (longitudinal and transverse views).	67
4.2	Shape of the delamination.	67
4.3	Conical shape of impact damage.	67
4.4	Response types during impact on plates.	68
4.5	Schematic Illustration of the impact procedure.	72
4.6	Numerical models used for impact analysis.	74
4.7	Location of cohesive elements.	75
4.8	Comparison of contact force-time history.	76
4.9	Velocity of the impactor.	76
4.10	Comparison of plate central displacement-time history.	77
4.11	Displacement of the impactor.	77
4.12	Delamination areas predicted by the PGD impact model for the laminate [90 ₃ /0 ₃] _s subjected to impact velocity 3 $m.s^{-1}$	77
5.1	Periodic composite materials and corresponding unit cells.	83
5.2	Homogenization of UD composite material.	84
5.3	Illustration of the periodicity cell concept.	85

5.4	Example of overlapping and non-overlapping decomposition of an initial domain Ω .	87
5.5	Original geometry used to introduce the alternating Schwarz method.	87
5.6	Non-overlapping domain decomposition.	89
5.7	Families of domain decomposition solvers.	92
5.8	Graphical illustration of the hierarchical grid levels.	93
5.9	1D mesh and decomposition in elementary parts.	95
5.10	Examples of 2D meshes and decomposition in elementary parts.	102
5.11	Corner element: nodes and neighboring cells definition	104
5.12	Heterogeneous elastic structure with periodic microstructure.	106
5.13	The representative unit cell at the microscale.	106
5.14	Domain decomposed into subdomains and boundary conditions.	107
5.15	Displacement fields (mm) : FEM solution (left) - PGD solution (right).	107
5.16	Stresses distributions : FEM solution (left) - PGD solution (right).	108
5.17	Convergence study on the distribution of the displacements along the thickness: (a) u_y for $y=0.04$ mm, (b) u_z for $y=0.072$ mm.	108
5.18	Convergence study on the distribution of the stresses along the thickness: (a) σ_{yy} for $y=0.072$ mm, (b) σ_{zz} for $y=0.072$ mm, (c) σ_{yz} for $y=0.04$ mm.	109
5.19	Computing time against number of subdomains.	110
5.20	Computing time against number of degrees of freedom (DOF).	110
5.21	Convergence of PGD solution.	110
5.22	Woven carbon fiber.	111
5.23	Periodic tetrahedral mesh of unit cell model.	111
5.24	Displacement fields and deformation of a plain weave based composite: full model is shown (left) - only yarn type materials are shown (right).	112
5.25	Stress distributions of a plain weave based composite: only yarn type materials are shown. Upper surface (left) - lower surface (right).	113
1	Séparation d'un problème 3D en 2D/1D.	126
2	Loi de comportement linéaire par morceaux pour le modèle cohésif. Traction/compression à gauche, cisaillement à droite.	127
3	Maillages 1D et 2D pour la simulation du délaminage.	128
4	Représentation schématique des dimensions de l'éprouvette DCB et des conditions aux limites imposées.	129
5	Représentation du champ de contrainte σ_{xx} .	130
6	La variable d'endommagement "d" à l'interface.	131
7	Localisation des éléments cohésifs.	132
8	La variable d'endommagement "d" à l'interface.	133

9	Cellule périodique pour un composite tissé à deux plis dans la même direction : représentation des fibres (gauche) et représentation de la matrice (droite).	135
10	Géométrie et conditions aux limites du problème considéré.	136
11	Profils des contraintes dans l'épaisseur au centre de la plaques. . . .	136
12	Contraintes σ_{xx} dans une plaque composite en flexion (vue de dessus et de dessous).	137

List of Tables

- 3.1 Various traction-separation relationships. 37
- 3.2 Length of the process zone and equivalent value of the parameter M . 42
- 3.3 The minimum number of required cohesive elements within the process zone. 43
- 3.4 Material properties for carbon/epoxy. 52
- 3.5 Quantification of the simulated process zone length using PGD method. 54
- 3.6 Mean relative error. 56

- 4.1 Cohesive properties. 73
- 4.2 Material properties of the laminate and impactor properties. 76

- 5.1 Material properties and geometric parameters of the virtual cell. . . 106
- 5.2 Material property. 111

- 1 Propriétés mécaniques du pli et propriétés de l'interface. 130

Représentations séparées pour la simulation multi-échelle du comportement mécanique et de l'endommagement des matériaux composites.

Résumé: Le développement de méthodes numériques performantes pour simuler les structures composites est un défi en raison de la nature multi-échelle et de la complexité des mécanismes d'endommagement de ce type de matériaux. Les techniques classiques de discrétisation volumique conduisent à des coûts de calcul importants et sont restreintes en pratique à des petites structures.

Dans cette thèse, une nouvelle stratégie basée sur une représentation séparée de la solution est explorée. L'objectif est de proposer un cadre numérique efficace et fiable pour analyser les endommagements dans les composites stratifiés sous chargements statiques et dynamiques. La décomposition propre généralisée (PGD) est utilisée pour construire la solution.

Pour traiter l'endommagement, et plus particulièrement le délaminage, un modèle de zone cohésive a été implémenté dans la PGD. Une approche multi-échelle innovante est également proposée pour simuler le comportement mécanique des composites à microstructure périodique. L'idée principale est de séparer deux échelles : l'échelle du motif périodique (microstructure) et l'échelle macroscopique. Les résultats de la PGD sont très proches des résultats obtenus par la méthode éléments finis classique. Finalement, la PGD permet de réduire significativement la complexité des modèles tout en gardant une précision satisfaisante.

Mots clés: Matériaux composites, Réduction de modèle, Décomposition généralisée propre, Modélisation multi-échelle, Impact, Endommagement

Separated representations for the multiscale simulation of the mechanical behavior and damages of composite materials.

Abstract: The development of efficient simulations for composite structures is very challenging due to the multiscale nature and the complex damage process of these materials. When using standard 3D discretization techniques with advanced models for large structures, the computational costs are generally prohibitive.

In this thesis, a new strategy based on a separated representation of the solution is explored to develop a computationally efficient and reliable numerical framework for the analysis of damages in laminated composites subjected to quasi-static and dynamic loading. The PGD (Proper Generalized Decomposition) is used to build the solution.

To treat damage, and especially delamination, a cohesive zone model has been implemented in the PGD solver. A novel multiscale approach is also proposed to compute the mechanical behavior of composites with periodic microstructure. The idea is to separate two scales: the scale of periodic pattern and the macroscopic scale. The PGD results have been compared with the results obtained with the classical finite element method. A close agreement is found between the two approaches and the PGD has significantly reduced the model complexity.

Keywords: Composite materials, Model reduction, Proper Generalized Decomposition, Multi-scale modeling, Impact, Damage

